DEVELOPMENT OF BIOACTIVE GLASS BASED COMPOSITES FOR CORROSION RESISTANT COATING APPLICATIONS

Thesis Submitted to

DELHI TECHNOLOGICAL UNIVERSITY

For the Award of the Degree of

DOCTOR OF PHILOSOPHY

Submitted By

NARJES IBRAHEM KHALED

2K21/PhD/CH/02

Under the Guidance of

Dr. Deenan Santhiya

Department of Applied Chemistry

Delhi Technological University

Shahbad Daulatpur, Main Bawana Road,

Delhi- 110042, INDIA

April, 2024

DELHI TECHNOLOGICAL UNIVERSITY

(Formerly Delhi College of Engineering)

Department of Applied Chemistry

Shahbad Daulatpur, Bawana Road, Delhi- 110042, India

DECLARATION

This is to declare that the research work embodied in this thesis entitled **"Development of Bioactive Glass Based Composites for Corrosion Resistant Coating Applications"** submitted to the Delhi Technological University **is an original work and carried out by me for the degree of Doctor of Philosophy in Chemical Engineering** under the supervision of **Dr. Deenan Santhiya**, **Assistant Professor**, Department of Applied Chemistry. This thesis is a contribution to my original research work. The extent of information derived from the existing literature has been indicated in the body of the thesis at appropriate places giving the source of information. Every effort has been made to make sure that the scientific contributions of others are appropriately cited. To the best of my knowledge, this research work has not been submitted in part or full for award of any degree or diploma in Delhi Technological University or in any other university/institution.

Date:

Narjes Ibrahem Khaled
Research Scholar
Reg. No. 2K21/PhD/CH/02

DELHI TECHNOLOGICAL UNIVERSITY

(Formerly Delhi College of Engineering)

Shahbad Daulatpur, Bawana Road Delhi- 110042, India

CERTIFICATE

This is to certify that the thesis entitled **"Development of Bioactive Glass Based Composites for Corrosion Resistant Coating Applications"** submitted to the Delhi Technological University, Delhi-110042, in fulfillment of the requirement for the award of the degree of **Doctor of Philosophy in Chemical Engineering** has been carried out by the candidate, **Mrs. Narjes Ibrahem Khaled**, (Reg. No. 2K21/PhD/CH/02) under the supervision of **Dr. Deenan Santhiya**, **Assistant Professor**, Department of Applied Chemistry. It is further certified that the work embodied in this thesis has neither partially nor fully been submitted to any other university or institutionfor the award of any degree or diploma.

Dr. Deenan Santhiya
Supervisor
Department of Applied Chemistry Delhi Technological University, Delhi

Prof. Anil Kumar
Head of the Department
Department of Applied Chemistry
Delhi Technological University, Delhi.

DEDICATED TO

MY HUSBAND …

Acknowledgment

"I am blessed with everything I need. I am working hard towards everything I want, and most of all, I appreciate & Thank God for what I have."

I would like to thank God for the successful completion of my research work.

Coming to the end of my Ph.D., I pour out my thoughts and hope that reflect the deep gratitude I hold for people that have made it possible for me to surmount this hurdle and achieve my dream.

The life of a Ph.D student is anchored by their supervisor and I am extremely fortunate to have ***Dr. Deenan Santhiya*** *as my mentor, an individual with years of experience and possibly the most encouraging person. I have come across in my educational years. She is not only the person behind innumerable success stories of her doctoral students but also the one who established a pioneering research ethics amongst young researchers. A life filled with such scholarly achievements is only possible when the person is immensely talented and truly committed to their cause. I have witnessed her humility in response to gratitude, strength in face of adversity, decisiveness in matters of dilemma and undistinguished love for science at every step. Her scientific aptitude and clarity of even complex concepts helped me in testing times of research while her ability to motivate students to discover their hidden talents has introduced me to my own strengths. Her extensive generosity taught me the value of being generous, and her promptness taught me the value of time management. Her concept of "work hard, play hard" has been inspiring throughout the duration of my association with her. I am incredibly fortunate to have been trained and introduced to the world of research under her guidance.*

I am extremely grateful to ***Professor Anil Kumar*** *(Head, Department of Applied Chemistry) for providing the necessary research facilities and an excellent working environment in the department. His work exhibits the ideal fusion of punctuality, enthusiasm, commitment, organization, and excellent administrative abilities. We are fortunate to have a visionary like him in our department.*

I would also like to thank ***Professor D. Kumar, Professor R. C. Sharma, Professor R. K. Gupta, Professor S. G. Warkar, Professor Ram Singh, Professor Roli Purwar, Dr. Richa Srivastava, Dr. Manish Jain, Dr. Raminder Kaur, and Dr. Poonam, faculty members****,***Department of Applied Chemistry, DTU for their time-to-time valuable support.*

No word and no language is ever adequate to express my heartfelt admiration for to my loving ***husband (Muslim Abdul Wahed Qaitan)*** *for his support, encouragement and patience when it was most needed and standing by my side throughout this entire journey. I would like to thank my* ***daughter*** *sweet heart* ***(Rahaf)*** *for her loving, patience and cooperation during all my studies. A lot of thanks to baby sitter (****Sumitra****).*

- *I am grateful to all my labmates and deepest thanks to* ***Dr. Manjot Kaur, Dr. Neha*** *for them help and supportwhenever needed and for being such a good friend.*
- *I am grateful to* ***Anurag, Dr. Owais , and Divya Hood*** *for help me to do testing.*
- *I thank all the non-teaching and official staff of the Department of Applied Chemistry for their obligatory help whenever needed.*
- *I am grateful to* ***Prof. Prateek Sharma*** *(Vice Chancellor) of Delhi Technological University for giving me this opportunity to conduct my research work.*
- *Finally, I must thank all those, whom I have failed to mention specifically and personally, but they have helped me in various ways during this work.*

Thank you so much!!!!!

Narjes Ibrahem Khaled

ABSTRACT

Magnesium and its alloys show great promise as potential biodegradable metals for use in orthopedic applications. However, one significant challenge that has hindered their widespread adoption in medicine is their rapid degradation rate in the physiological environment. This thesis is aimed to explore surface modification strategies that could effectively regulate the degradation rate of magnesium alloys when exposed to physiological environments. Additionally, the study seeks to conduct thorough in vitro assessments and evaluations of the biocompatibility of these modified alloys. The overall thesis is composed of two individual projects.

Chapter 1, discusses a brief introduction of magnesium alloy as biodegradable materials and discusses the degradation rate when implanted in human body. Also, presents the approach strategies for surface modification to enhance corrosion resistance, biocompatibility and mechanical integrity of magnesium alloy.

Chapter 2, investigates the effect of zein-bioactive glass (BG) nanocomposite on AZ31B magnesium alloy. BG nanoparticles required for zein and BG (zein_BG) composite were synthesized by a bio-inspired method using cetyltrimethylammonium bromide (CTAB) as a template. The formation of BG particles were confirmed by Fourier transform infrared spectroscopy (FTIR) showing characteristic Si-O-Si and $Si\text{-}O^-$ peaks. Nano-size of BG particles with an average diameter of (6.67 ± 0.06) nm was reported by transmission electron microscopy (TEM). Scanning electron microscopy (SEM) revealed successful deposition of zein and zein_BG coatings on the magnesium alloy surfaces. High resolution X-ray Photoelectron Spectroscopy (XPS) analysis on zein_BG coated Mg alloy immersed in HBSS revealed the corrosion deposition of $Mg(OH)_2$,$MgHPO_4.H_2O$, $CaHPO_4.H_2O$, SiO_2 , $MgCO_3$ and $CaCO_3$ on the substrate surface. More than two-fold wettability, 95 % adhesion strength, and 14-fold increase in surface roughness were reported for zein_BG coated magnesium alloy compared to the bare surface. Measurements of weight loss and electrochemical measurements in zein and zein_BG coated alloy substrates in Hanks Balanced Salt Solution (HBSS) for 10 d at 37 ℃ showed a drastic decrease in weight loss of substrates after coating. As a result, zein_BG coated substrate was observed to possess the maximum protective efficacy (95.99 %) against corrosion. These findings demonstrated that simple zein_BG composite dip coating was a successful corrosion-resistant implant coating on magnesium alloy surface for orthopedic applications.

Chapter 3, the present study reports on a novel multilayer coating for biodegradable magnesium (Mg) alloy substrates. This coating contains soy protein hydrolysate (SPH), poly(allylamine hydrochloride) (PAH), and folic acid (FA) templated bioactive glass (BG) nano particles. The multilayer, designated as SPH/$(PAH/BG)_n$, was coated onto an alkaline-treated Mg alloy surface (AMgS) through a dip-coating process with various numbers of cycles (n = 5 and 7) using a layer-by-layer (LbL) assembly. The BG particles had an average diameter of 12.53 ± 2.22 nm and were embedded with therapeutic FA molecules. Scratch testing, wettability, and roughness tests showed excellent adherence of the SPH/$(PAH/BG)_7$ coating on AMgS, making it suitable for cell attachment. Electrochemical measurements in Hanks balanced salt solution (HBSS) demonstrated that the SPH/$(PAH/BG)_7$ coating improved the corrosion resistance of the Mg alloy. SPH/$(PAH/BG)_7$ coated substrate showed a maximum protective efficacy of 98.4041% , thanks to the bioactive nature of BG. High-resolution XPS and XRD analyses on SPH/$(PAH/BG)_7$/AMgS confirmed the corrosion deposition of $Mg(OH)_2$, $MgHPO_4.H_2O$, $CaHPO_4.H_2O$, SiO_2, $MgCO_3$ and $CaCO_3$ on the substrate surface after immersion in HBSS for 10 d at 37 ℃. The LbL coated Mg substrate also showed excellent cytocompatibility by hemolysis assay These results suggest that the SPH/$(PAH/BG)_7$ /AMgS material has multifunctional properties and can be a possible alternative for biomedical applications of Mg alloys.

Chapter 4, summarizes the main conclusions and recommendations for future work by use of surface modification (layer by layer) coating of magnesium alloy.

LIST OF PUBLICATIONS

- **Narjes Ibrahem Khaled**, Deenan Santhiya. " Zein_Bioactive Glass Nano Composite Coating on Magnesium Alloy Substrate for Orthopedic Applications". **"Advanced Composite Materials"** (2023) **(SCIE indexed) (ImpactFactor: 2.9)**
- **Narjes Ibrahem Khaled**, Deenan Santhiya. " Multifunctional Poly(Allylamine Hydrochloride) / Bioactive Glass Layer by Layer surface coating on Magnesium Alloy for biomedical applications ". **"Progress in Organic Coatings"** 186 (2024):108059. **(SCIE indexed) (Impact Factor: 6.6)**

CONFERENCE PROCEEDINGS

- **Narjes Ibrahem Khaled** , Deenan Santhiya, " Effect of Nano Fillers on Mechanical and Tribological Properties of Polymer Nano Composites: A Review ", International Conference Advances in Chemical Science and Nanocomposites, ACSN 2022 Organized by Zakir Husain Delhi College and ISAS", India during 1 – 2 April, 2022 (poster)

- **Narjes Ibrahem Khaled** , Deenan Santhiya, "Zein/Bioactive glass Nano Composite Coatings for Orthopedic Application to Improve the Surface Properties of Magnesium Alloy", International conference on Nanotechnology: opportunities & challenges, ICNOC 2022 organized by Jamia Millia Islamia", India during 28 – 30 November, 2022. (poster)

- **Narjes Ibrahem Khaled** , Deenan Santhiya, "In Vitro Corrosion Resistance of a Layer by Layer Assembled Poly(Allylamine Hydrochloride) / Bioactive Glass Coating on Magnesium Alloy ", International hybrid conference on nano structured materials and polymers, ICNP 2023 organized by Mahatma Gandhi University, India during 12 – 14 May, 2023 (oral presentation)

CONTENT

List of Figures

List of Tables

Nomenclature

English Symbols		
Symbol	**Definition**	**Unit**
A	Area of specimen	cm^2
C_1	Capacitance of protection layer	$(\Omega^{-1}.S^n\ cm^{-2})$
C_2	Capacitance of corroded layer	$(\Omega^{-1}.S^n\ cm^{-2})$
CPE	Constant phase element	$(\Omega^{-1}.S^n\ cm^{-2})$
CR	Corrosion Rate	$(mg/cm^2.d)$ Or (mm/years)
E_{corr}	Corrosion potential	(V/SCE)
I_{corr}	Corrosion current density	(A/cm^2)
R_1	Resistance due to surface deposited such as hydroxide	$(\Omega.cm^2)$
R_2	Resistance due to coating	$(\Omega.cm^2)$
R_3	Resistance due to defects through the film	$(\Omega.cm^2)$
R_a	Surface roughness	µm
R_p	Resistance polarization	$(\Omega.cm^2)$
R_s	Solution resistance	$(\Omega.cm^2)$
t	Time of immersion	hour
W_1	Weight loss for sample before immersion	mg
W_2	Weight loss for sample after immersion	mg
ω	Angular velocity	red/sec
Z_{CPE}	Impedance of the constant phase element	Ω
Z_{imag}	Imaginary impedance	$(k\Omega.cm^2)$
Z_{real}	Real impedance	$(k\Omega.cm^2)$
β_a	Anodic Tafel slope	$V.dec^{-1}$
β_c	Cathodic Tafel slope	$V.dec^{-1}$
ΔW	Weight loss difference	mg
$\lvert Z \rvert_{10HZ}$	Amplitude	$(\Omega.cm^2)$

Abbreviations	
Symbol	**Definition**
AMgS	Alkaline treated Mg alloy substrate
ASTM	American society for testing and materials
AZ31	3%Al, 1%Zn magnesium alloy
BG	Bioactive glass
$Ca(PO_4)_2$	Calcium phosphate
Ca^{2+}	Calcium ion
CaAc	Calcium acetate
$CaCO_3$	Calcium Carbonate
$CaHPO_4.H_2O$	Calcium phosphate dihydride

CaO	Calcium oxide
CHI	Chitosan
Cl^-	Chloride
CO_2	Carbone dioxide
CTAB	Cetyltrimethylammonium bromide
d	day
$D_{negative}$	Absorbance of negative control
$D_{positive}$	Absorbance of Positive control
D_{test}	Absorbance of testing sample
EDS	Energy dispersive spectroscopy
EIS	Electrochemical impedance spectroscopy
FA	Folic acid
FESEM	Field emission scanning electron microscopy
FTIR	Fourier Transformed Infrared Spectroscopy
h	hour
H_2	Hydrogen gas
H_2O	Water
H_3O	Hydronium
HA	Hydroxyapatite
HBSS	Hanks' balanced salts solution
HPO_4^{2-}	Hydrogen phosphate
HR%	Hemolysis ratio
ISO	International organization for standardization
LBL	Layer by layer
LDH	Layered double hydroxide
Mg	Magnesium
$Mg(OH)_2$	Magnesium hydroxide
Mg^{2+}	Magnesium ion
$MgCl_2$	Magnesium Chloride
$MgCO_3$	Magnesium Carbonate
$MgHPO_4.H_2O$	Magnesium phosphate dihydride
MgO	Magnesium oxide
$MgPO_4$	Magnesium phosphate
MgS	Mg alloy substrate
n	Exponent of constant phase element
Na_2O	Sodium oxide
NaAc	Sodium acetate
NaOH	Sodium hydroxide
nHA	Nano Hydroxyapatite
OH^-	Hydroxide ion
P_2O_5	Phosphate dioxide
PAA	Poly(acrylic acid)
PAH	Poly(allylamine hydrochloride)
PBS	Phosphate buffer saline
PE%	Protection efficiency

PEI	Poly(ethyleneimine)
PGA	Polyglycolic acid
PO_4^{3-}	Phosphate
PVDF	Polyvinylidene fluroide
PVP	polyvinylpyrrolidone
SBF	Simulated body fluid
SEC	Saturated calomel electrode
SEM	Scanning electron microscopy
$Si(OH)_2$	Silicon dyhydoxide
SiO_2	Silicon dioxide
SiO_4	Silicon oxygen tetrahedron
SPH	Soy protein hydrolysate
SPH$(PAH/BG)_n$/ AMgS	Represent number of cycle coating, n=5&7 that do it on alkaline treated Mg alloy substrate
TEM	Transmission electron microscopy
TEOS	Tetraethyl orthosilicate
TEP	Triethyl Phosphate
TGA	Thermogravimetric analysis
XPS	X – ray photoelectron spectroscopy
XRD	X- ray diffraction
Zein_BG	Zein _bioactive glass composite coating
ZIF-8	Zeolitic imidazolate framework -8
Ɵ	Surface coverage

CHAPTER 1
Introduction

Chapter One
Introduction

1.1. Biodegradable Orthopedic Biomaterials

Advanced orthopedic surgical treatments rely heavily on the progress of biomaterials utilized for repairing fractures and replacing joints [1]. Biomaterials are synthetic materials that are utilized in medical applications to treat or replace damaged or diseased tissue in various areas of the body. Examples of these applications include dental, cardiovascular, and orthopedic implants [2].

The use of biomaterials significantly enhances the health and well-being of humans [3]. The human body is susceptible to a range of painful injuries, including strains, sprains, dislocations, and fractures. A fracture is the result of excessive external force acting on a bone, which is larger than the strength of the osseous tissue. The risk of fractures varies depending on factors such as age, gender, bone strength, and overall health [4,5].

Every year, millions of people suffer from bone fractures and degenerative joint diseases, which may require varying types of treatment depending on the extent of the damage. In the case of degenerative joint disease, bone replacement is often necessary, and permanent implants such as artificial hips and knees are used to replace damaged tissue [6]. To ensure the longevity and stability of permanent implants within the body, they are typically made from inert materials like titanium, titanium alloys, and cobalt-chrome alloys. In cases where fracture fixation is required, metallic pins, screws, and plates may be surgically implanted to provide external support for the damaged bone tissue during the healing process [7]. The predominant materials utilized for bone fracture fixation are metals, including stainless steel and titanium alloys. Following tissue healing, the temporary implants, necessitate a second surgical procedure for their removal. As a consequence, this process can lead to the potential re-damage of the healed bone, causing discomfort for the patient, and imposing a considerable financial burden on the healthcare system [1].

Synthetic biomaterials should ideally mimic the tissue at the site of restoration, but this is often challenging to achieve. Therefore, Biomaterials employed for tissue restoration generally necessitate the following characteristics [2,8]:

1) Biocompatibility; this property ensures that the material is non-toxic, does not cause inflammatory reactions, hemolysis, or coagulation responses. As a result, the biomaterial can be safely utilized in the human body without eliciting any adverse reactions.
2) Osteoconductivity; It refers to the material's ability to stimulate osteogenesis, the process of new bone formation. An osteoconductive material should facilitate cell attachment, proliferation, and migration, allowing the formation of an extracellular matrix on its surface and within its pores. This property promotes the growth of new bone tissue and facilitates the effective restoration of damaged bone.
3) Biodegradability; It involves the material's ability to undergo degradation or breakdown over time, ideally at a rate that aligns with the pace of bone regeneration and growth.
4) Mechanical Properties; biomaterials used for tissue restoration should have suitable mechanical properties that match those of natural bone at the site of implantation. These properties include bending, compression, and tensile strength, as well as fatigue resistance to sustain loads applied during bone growth. This ensures that the implant can withstand the stresses and strains experienced during normal physical activity.
5) Surface Properties; a suitable surface chemistry and topological features are essential to facilitate effective cell attachment, differentiation, and proliferation. The surface chemistry should be tailored to promote cellular interactions, while the topological features play a role in supporting cellular adhesion and migration.
6) Commercialization; The materials chosen for medical applications should be cost-effective and affordable for large-scale production and distribution. Ensuring an acceptable cost for commercialization allows these biomaterials to be widely accessible to healthcare providers and patients, making the treatment options more practical and sustainable within the healthcare industry.

Many biodegradable biomaterials have been identified, with a significant portion of them being polymers. However, biodegradable polymers often lack the ability to effectively stimulate bone regeneration and their mechanical properties differ from those of natural bone. Therefore; metallic materials are better suited for load-bearing applications when compared to polymeric materials, primarily due to their high mechanical strength and fracture toughness. In recent years, biomaterials scientists have suggested the use of biodegradable metallic implants made from chemically reactive metals, such as iron and magnesium [9].

1.2. Magnesium Alloy as A biodegradable Implant

Magnesium (Mg) is a biodegradable and lightweight metal with superior mechanical properties. Its strength and ductility are comparable to those of natural bone, making it a promising material for bone fracture fixation [10]. Magnesium is an essential mineral element for the human body, elaborate in various metabolic processes. It acts as an enzymatic cofactor, stabilizes the structure of DNA and RNA, and helps maintain the function of muscles and nerves. An adult human body typically contains a significant amount of approximately (0.4 g Mg / kg) body weight, varying based on individual weight. A major portion of this element (50 - 60%) is found within bone tissue [11].

Magnesium exhibits physical and mechanical properties that closely resemble natural bone when compared to traditional metallic implant materials, with a density of (1.738 g/cm^3) close to that of human bone tissue (1.8 g/cm^3). The elastic modulus of Mg (45 GPa) and compressive strength (100 MPa) similar to that natural bone which is has (20 GPa) and (130 MPa), for elastic modulus and compressive strength, respectively[5]. The similarities between magnesium and natural bone can potentially reduce or avoid the stress shielding effect, which can enhance stimulation and remodeling of the bone tissue. Due to these properties, magnesium proves to be an excellent biomaterial for fracture fixation devices, offering robust mechanical stability during the early stages of healing.

1.3. Degradation Process of Mg Alloy

Overall, the healing process of bone fracture occurs in three stages: inflammation (1 – 7) days, repair (3 – 4) months, and remodeling (several months to year). Unfortunately, the majority of Mg-based orthopedic implants degrade before complete healing, leading to implant failure [12].

Research has demonstrated that magnesium (Mg) exhibits high degradability in both acidic and neutral pH conditions, which are commonly encountered in the physiological environment. Consequently, the rapid degradation of Mg within the human body can hinder tissue regeneration and potentially compromise the mechanical integrity of the implanted material. This situation may increase the risk of a second fracture occurrence [13].

When Mg is immersed in an aqueous solution, it undergoes an anodic reaction, as depicted in eq.(1.1), leading to the generation of Mg^{2+} cations on its surface. Simultaneously, a cathodic reaction takes place, with protons being reduced at the cathode to produce H_2 gas and OH^- ions, as shown in eq.(1.2) Consequently, the surface of Mg becomes covered with a film of $Mg(OH)_2$, as demonstrated in eq.(1.3)[3]:

$$Mg \leftrightarrow Mg^{2+} + 2e^- \quad \text{(anodic partial reaction)} \quad (1.1)$$

$$2H_2O + 2e^- \leftrightarrow H_2 + 2OH^- \quad \text{(cathodic partial reaction)} \quad (1.2)$$

$$Mg + 2H_2O \leftrightarrow Mg(OH)_2 + H_2 \quad \text{(overall reaction)} \quad (1.3)$$

Fig. 1.1 illustrates the corrosion degradation process of biomedical Mg alloys in body fluids. Galvanic coupling arises due to the potential difference between the magnesium substrate and intermetallic phases or grain boundaries, leading to electrochemical reactions taking place on the surface. Moreover, some organic molecules may be adsorbed on the surface of Mg alloys, affecting the corrosion process of the material. As a result of the reaction process, the local environment becomes alkaline due to the generation of OH^- ions, which leads to the formation of a $Mg(OH)_2$ film on the surface of the Mg substrate. This film acts as a barrier that separates the Mg from the surrounding environment. However, the $Mg(OH)_2$ film is not tightly bound and contains pores, which allows external corrosion media to penetrate through the holes and attack the fresh Mg substrate. This leads to the formation of corrosion pits and the production of a significant amount of $Mg(OH)_2$. It is important to mention that the human body contains a high concentration of chloride ions (Cl^-) which is around 150 mmol/L. When the concentration of chloride ions in the environment surrounding the Mg, substrate reaches 30 mmol/L, it causes the conversion of $Mg(OH)_2$ into soluble $MgCl_2$. This process can result in corrosion defects caused by chloride ions. The reactions as shown below in eqs. (1.4) and (1.5)[14].

$$Mg(OH)_2 + 2Cl^- \leftrightarrow MgCl_2 + 2OH^- \quad (1.4)$$

$$Mg^{2+} + 2Cl^- \leftrightarrow MgCl_2 \quad (1.5)$$

When the $Mg(OH)_2$ layer is destroyed, the local alkalinity rises, and the Ca^{2+} and PO_4^{3-} ions in the bodily fluid use the remaining $Mg(OH)_2$ as the nucleation sites to produce calcium phosphate-based apatite. The surface of magnesium substrate forms a corrosion

products layer as a result of carbonates reacting with acid or CO_2, leading to the deposition of these products. Additionally, cells are observed to adhere to the surface of magnesium. As the implantation duration extends, the attached cells undergo increased proliferation, leading to the development of new tissue in proximity to the corrosion product layer. Furthermore, the corroded magnesium may detach from the substrate, manifesting as particles that separate and fall off. The particles have the potential to become enveloped and ingested by the fibrous tissue or macrophages, undergoing this process until complete degradation occurs [15].

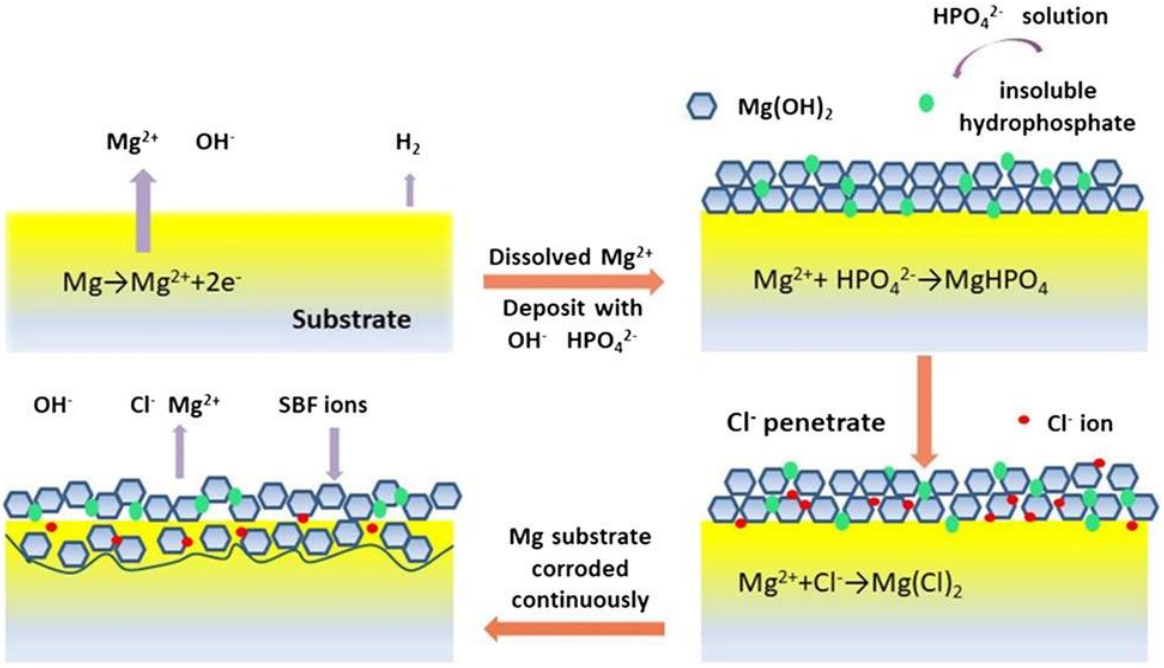

Fig. 1.1: A schematic showing the corrosion processes in Mg-based alloys in the presence of simulated bodily fluid (SBF) [14].

1.4. Improving the Performance of Mg for Orthopedic Applications

The service environment of biomedical magnesium alloys is complex, with their mechanical performance and corrosion behavior heavily influenced by factors such as alloy composition, microstructure, environmental conditions, and stress levels. In recent years, researchers have made substantial efforts to achieve optimal corrosion resistance for magnesium biomaterials. This includes the development of novel magnesium alloys and the implementation of advanced surface modification techniques.

1.4.1. Alloying

Alloying represents a primary approach to enhance the mechanical performance of metals. Specifically, incorporating suitable alloying elements can lead to grain refinement and optimize the type, size, and distribution of second phases in the material, consequently boosting the corrosion resistance of magnesium alloys. Furthermore, these alloying elements have the capability to create passive films or corrosion product layers that act as barriers, preventing the corrosion from further propagation. Presently, aluminum, zinc, manganese, calcium, strontium, lithium, and zirconium elements are extensively employed as alloying elements for this purpose [9]. The alloy utilized in this study is AZ31, where "A" & "Z" denote aluminum and zinc, respectively. The alloy contains 3 wt% of aluminum and 1 wt% of zinc. This particular composition offers a favorable combination of desirable mechanical properties, corrosion resistance, and a relatively low concentration of aluminum [16].

1.4.2. Surface Modification

Surface modification is a crucial method to enhance the corrosion resistance of Mg alloys, alongside its impact on other aspects. By employing suitable surface modification techniques, we can not only improve the mechanical properties and corrosion resistance of Mg alloys but also enhance their biological functionality, including biocompatibility and bioactivity.

1.4.2.1. Parameters Affecting Surface Modification

Numerous parameters influence the surface characteristics of orthopedic implants and their subsequent cell response [17].

1) Surface Characteristic

Orthopedic implants must not only exhibit non-toxicity and stability in terms of cytotoxicity and degradation but also need to be designed to closely resemble the structure of bone. This structural compatibility aims to optimize the interaction between the implant surface and the living tissue, promoting better integration and functionality.

2) Surface Roughness

Surface roughness; Surface roughness plays a critical role in determining the osseointegration rate and biomechanical fixation of orthopedic implants to bone. For

magnesium alloys, specifically, an important finding is that increasing the surface roughness of the Mg alloy results in a significant improvement in bone cell adhesion. Consequently, this enhanced adhesion leads to an increase in the deposition of hydroxyapatite, which is essential for the successful integration of the implant with the surrounding bone tissue.

3) Porous Structure

The size and morphology of pores significantly influence cell attachment and proliferation on implant surfaces. However, it is important to note that as the pore size increases, the mechanical properties of the implants tend to decrease, leading to a more brittle behavior.

4) Wettability

The biological response of a biomaterial is influenced by its wettability, which refers to its hydrophobicity or hydrophilicity. Wettability is affected by various factors, including surface roughness, chemical composition, surface energy, and heterogeneity. A hydrophilic surface, which exhibits a preference for water, is known to enhance cell adhesion on the implant surface.

1.4.2.2. Types of Surface Modification

Surface modification methods can be categorized into three types: chemical modification, physical modification, or a combination of these two approaches [18,19].

1) Chemical Modification

This particular type of modification involves the removal of the native oxide layer from the surface and its subsequent replacement with a new phase. As a result of this process, the adhesion to the substrate is improved due to the formation of chemical bonds between the modified surface and the substrate.

i) Acid Etching; this method of removing the native oxide layer, followed by the creation of uniform and compact layers, can be adopted to achieve a lower corrosion rate. By ensuring a consistent and tight surface, the implant's resistance to corrosion is improved, enhancing its overall durability and performance.

ii) Alkaline Treatment; After immersing Mg alloys in alkaline solutions, a new passive layer is formed on their surface. This passive layer primarily consists of compounds such as $Mg(OH)_2$, $MgCO_3$, and MgO.

2) Physical Modification

Indeed, physical coating, also known as a physical barrier coating, can be utilized through several approaches to form protective coatings on Mg substrates. This type of coating acts as a barrier between the metal and the corrosive environment, safeguarding the Mg from degradation. Several techniques can be employed for physical coating, including shot peening, laser surface treatment, anodization, and plasma electrolytic oxidation.

3) Coating

This technique entails applying a thin layer of material to the surface of Mg alloy, aiming to alter and enhance its surface properties. One such application is the use of bioactive glass coating, which can effectively improve the biocompatibility and osteointegration of Mg alloys

1.5. Bioactive Glass as Coating Materials

Around five decades ago, Bioactive glass 45S5 was first discovered by Professor Larry Hench at the University of Florida (USA). Since its discovery, it has remained one of the most extensively studied bioactive glass compositions [20]. Numerous novel glass compositions have been suggested and have found diverse biomedical applications, ranging from dental fillings and drug delivery systems to coatings for load-bearing metal implants and tissue engineering purposes [21]. The bioactive glass coating has demonstrated successful applications across a broad spectrum of implant materials, including titanium, stainless steel, and magnesium, for various orthopedic applications. As a result of these coatings, notable enhancements were observed in corrosion resistance, adhesion strength, and bioactivity. Among these properties, the bone-bonding capability of bioactive glass is particularly noteworthy, making it highly regarded for its material biocompatibility. Bioactive glass primarily consists of silicon dioxide (≤ 52 wt%) as a binding substance, sodium dioxide (≤ 32 wt%) as a strength provider, calcium oxide (≤ 16 wt%), and phosphorous pentoxide (≤ 6 wt%) as components that are bio-inert and promote bone formation. This unique composition enables bioactive glass not only to bond with bones but also with soft tissue. Its rapid surface activity facilitates uninterrupted and swift attachment to surrounding tissue through chemical bonding [22].

The mechanism of action of a bioactive glass-coated substrate in Hanks Balanced Salt Solution (HBSS) is depicted in **Fig. 1.2**. When the bioactive glass-coated substrate is exposed to HBSS, it releases alkaline or alkaline earth elements, leading to the replacement of cations with H_3O^+ and H^+ ions from the HBSS. As a result, $Si(OH)_2$ dissolves due to the action of hydroxyl ions. Meanwhile, calcium and phosphate ions migrate and react with CO_3^{2-} ions present in the HBSS, forming a calcium phosphate layer. The bone bonding capability of bioactive glass is closely associated with its ability to form a carbonated apatite layer, which facilitates strong bonding with the surrounding bone tissue. This process enhances the integration and long-term stability of the implant in the body [4].

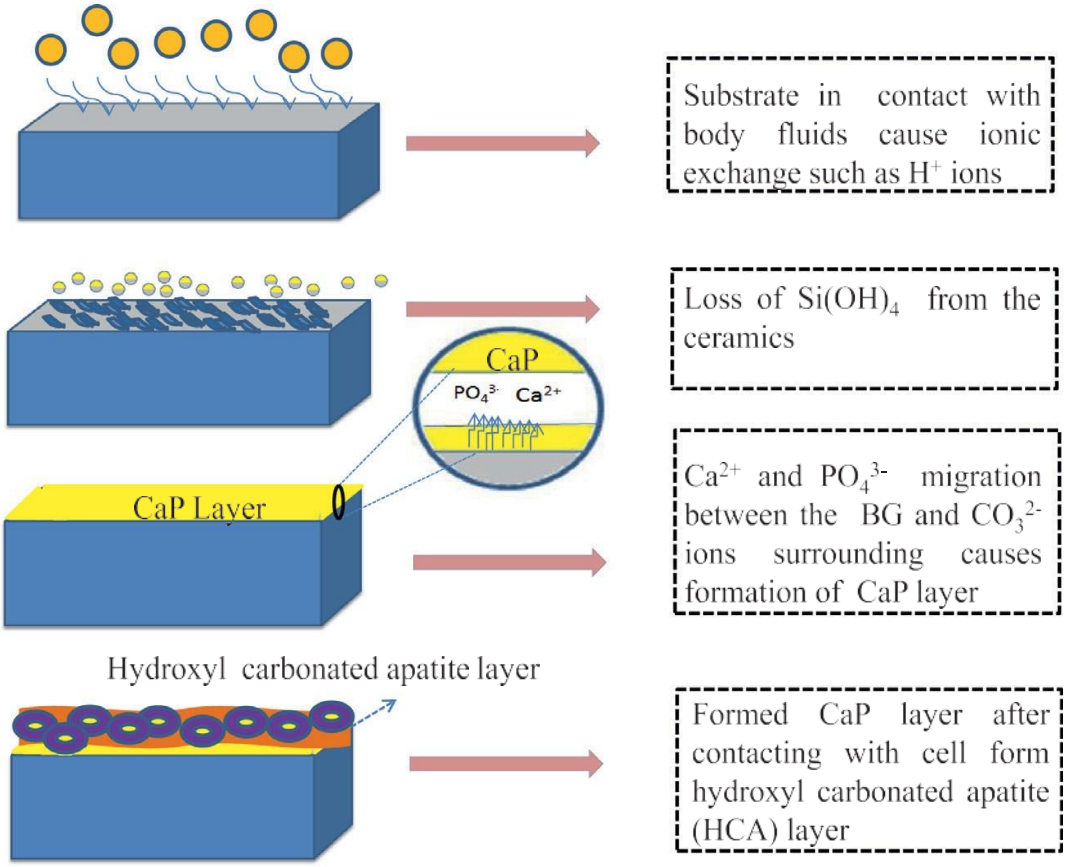

Fig. 1.2: The in-vitro mechanism of action of BG coated substrates in Hank's Balanced Salt Solution (HBSS)[4].

1.6. Major Objective of the Thesis

The major objectives of the thesis are as follows:

- ❖ Novel strategies to synthesize bioactive glass materials, by bio-inspired method and using as coating for Mg alloys for orthopedic application.
    - Synthesis of bioactive glass nanoparticles using Cetyltrimethylammonium bromide as template.
    - Synthesis of bioactive glass nanomaterials using folic acid as template.

- ❖ To develop surface modification coating strategies that facilitate controlled degradation of Mg alloys in physiological environments while concurrently improving the biocompatibility of the surface.

    - Fabricate zein, zein_ bioactive glass coating on Mg alloys via dip coating technique.
    - Design a novel coating, {soy protein hydrolysate, poly (allylamine) hydrochloride, and bioactive glass} layer by layer coating on alkaline treated Mg alloy surface, as SPI/$(PAH/BG)_n$ /AMgS via dip coating technique.

- ❖ Characterization of the coatings to determine their suitability for the proposed applications. For this purpose, a variety of techniques were considered, e.g. Fourier Transformed Infrared Spectroscopy (FTIR), X- Ray Diffraction (XRD), Thermogravimetric Analysis (TGA), X-ray photoelectron spectrometer (XPS) and Energy Dispersive Spectroscopy (EDS). Scanning Electron Microscopy (SEM) , Transmission Electron Microscopy (TEM) and Light Microscopy, were used to evaluate the macro and microstructure.

- ❖ To investigate the impact of the surface modification (coatings) on wettability, surface roughness, and adhesion strength.

- ❖ To evaluate the corrosion resistance and in – vitro bioactivity of uncoated and coated Mg alloys in Hanks balanced salt solution (HBSS) by weight loss, hydrogen

evolution and electrochemical measurement (Tafel slop and impedance spectroscopy).

1.7. Outline of the Thesis

The summary of the chapters included in the thesis is as follows:

Chapter II: In this chapter, discuss the synthesis of nanomaterial bioactive glass by using Cetyltrimethylammonium bromide as a template by bio – inspired method, the fabricated zein, (zein _ bioactive glass) coating on Mg alloy via dip technique and study the mechanical and corrosion resistance of un coated and coated Mg alloys in (HBSS) for different immersion time. Hence, the (zein _ bioactive glass) coating was showed favorable mechanical, biological and surface characterization for biomedical purpose and is a potential candidate for in – vivo investigations. Favorable mechanical, biological and surface characterization for biomedical purpose and is a potential candidate for in – vivo investigations.

Chapter III: In this chapter, discuss the synthesis of nanomaterial bioactive glass by using folic acid as a template, then design a novel coating by using {soy protein hydrolysate, poly (allylamine) hydrochloride, and bioactive glass} layer by layer coating on treatment Mg alloy surface, as SPI/$(PAH/BG)_n$ /AMgS via dip technique and evaluate the mechanical and corrosion properties of uncoated and coated Mg alloy. Hence, the SPI/$(PAH/BG)_n$ /AMgS, proven multifunctional (anti – cancerous, anti – oxidant and anti- inflammatory) properties for biomedical applications of Mg alloys.

Chapter IV: Summarizes the outcomes of the present research work. This chapter ends with the conclusion of major results of the study and suggestions of suitable material for future applications.

References:

[1] A. Al Hegy, Surface Modification of Biodegradable Magnesium Implant Materials for Controlled Biodegradation . (PhD) thesis in Materials Science, Laurentian University, 2019.

[2] L.E. Cordero Arias, Electrophoretic deposition of organic/inorganic composite coatings on metallic substrates for bone replacement applications: mechanisms and development of new bioactive materials based on polysaccharides, (PhD) thesis, Friedrich-Alexander-Universität Erlangen-Nürnberg Tag, 2015.

[3] N. Sezer, Z. Evis, S.M. Kayhan, A. Tahmasebifar, M. Koç, Review of magnesium-based biomaterials and their applications, J. Magnes. Alloy. 6 (2018) 23–43. https://doi.org/10.1016/j.jma.2018.02.003.

[4] L.M. Pandey, V.S. Yadav , M.R. Sankar, Coating of bioactive glass on magnesium alloys to improve its degradation behavior: Interfacial aspects, J. Magnes. Alloy. 8 (2020) 999–1015.

[5] R. Walter, Understanding and improving the degradation behaviour of magnesium-based biomaterials, (PhD) thesis, James Cook University, 2015. http://researchonline.jcu.edu.au/46520/.

[6] F.Y. Stuart, B. Goodman, Zhenyu Yao, Michael Keeney, The Future of Biologic Coatings for Orthopaedic Implants Stuart, Biomaterials. 34 (2013) 1–20. https://doi.org/10.1016/j.biomaterials.2013.01.074.The.

[7] M. Navarro, A. Michiardi, O. Castaño, J.A. Planell, Biomaterials in orthopaedics, J. R. Soc. Interface. 5 (2008) 1137–1158. https://doi.org/10.1098/rsif.2008.0151.

[8] L. Marina, Fabrication And Characterisation Of Bioactive/Biodegradable Materials For Tissue Engineering, (PhD) thesis, Università Degli Studi Di Cagliari , 2020.

[9] Y. Lu, Microstructure and degradation behaviour of Mg-Zn(-Ca) alloys, (PhD) thesis, University of Birmingham, 2014. http://etheses.bham.ac.uk/5301/.

[10] S.A. Arshanapalli, Fabrication Of Hydroxyapatite Coated Magnesium Alloy For Orthopedic Bio-Degradable Metallic Implant Applications, (M.Sc.) thesis, Wichita State University , (2013).

[11] R. Thornton, Magnesium Alloys As A Bioresorbable Implant Material, (PhD) thesis, University Of Manchester , 2010.

[12] D. Technischen, H.M.S.M. Höhlinger, Biodegradable coating development and analysis for a WE43 Mg alloy with focus on corrosion, surface analysis and biocompatibility, (PhD) thesis, Friedrich-Alexander-Universität Erlangen-Nürnberg, 2021.

[13] M.W. Diab, The Effect of Aluminum Cold Spray Coating on Corrosion Protection and Corrosion Fatigue Life Enhancement of Magnesium Alloy AZ31B, (M.Sc.) thesis University of Waterloo, 2015.

[14] R.F. and G.W. Liming Xu , Xingwang Liu , Kang Sun, Corrosion Behavior in Magnesium-Based Alloys for Biomedical Applications, Materials (Basel). 13 (2022) 1–31. https://doi.org/https://doi.org/10.3390/ma15072613.

[15] M.D. Helal Hossain, N. Hossain, M. Asaduzzaman Chowdhury, M. Arefin Kowser, M. Masud Rana, Surface synthesization of magnesium alloys for improving corrosion resistance and implant applications, Arab. J. Chem. 16 (2023) 104465. https://doi.org/10.1016/j.arabjc.2022.104465.

[16] A. Tahmasebifar, Surface Morphology Investigation of a Biodegradable Magnesium Alloy, (PhD) thesis, Middle East Technical University, 2015.

[17] T. Zhang, J.L. , Wen Wang, Y.T. and K.W. , Liqiang Wang, A review on magnesium alloys for biomedical applications Ting, Front. Bioeng. Biotechnol. (2022) 1–25. https://doi.org/10.3389/fbioe.2022.953344.

[18] D. Cuartas-Marulanda, L. Forero Cardozo, A. Restrepo-Osorio, P. Fernández-Morales, Natural Coatings and Surface Modifications on Magnesium Alloys for Biomedical Applications, Polymers (Basel). 14 (2022). https://doi.org/10.3390/polym14235297.

[19] S.A. Rahim, M.A. Joseph, T.S. Sampath Kumar, T. Hanas, Recent Progress in Surface Modification of Mg Alloys for Biodegradable Orthopedic Applications, Front. Mater. 9 (2022) 1–21. https://doi.org/10.3389/fmats.2022.848980.

[20] E. Andronescu, Bioactive Glass — An Extensive Study of the Preparation and Coating Methods, Coatings. 11 (2021) 1–28.

[21] S. Nilawar, M. Uddin, K. Chatterjee, Surface engineering of biodegradable implants: Emerging trends in bioactive ceramic coatings and mechanical treatments, Mater. Adv. 2 (2021) 7820–7841. https://doi.org/10.1039/d1ma00733e.

[22] A.B. Edathazhe , Investigation of properties, corrosion and bioactivity of novel BaO added phosphate glasses and glass-ceramic coating on biomedical metallic implant materials, (PhD) thesis, National Institute of Technology Karnataka, 2018.

CHAPTER 2

Zein_Bioactive Glass Nano Composite Coating on Magnesium Alloy Substrate for Orthopedic Applications

Chapter Two

Zein_Bioactive Glass Nano Composite Coating on Magnesium Alloy Substrate for Orthopedic Applications

2.1. Introduction:

Metallic biomedical materials such as stainless steel, cobalt chromium, or titanium alloys are extensively employed in orthopedic transplants [1–3]. Temporary fracture in these metallic fixation devices or inflammation at the implant site during the healing of fracture might lead to second surgery for their removal. This might increase patient trauma and medical costs. In recent years, a new class of biomedical implant materials made up of magnesium (Mg) alloy is extensively used [4,5]. The modulus of Mg alloy is very similar to natural tissue that provides resistance against stress and helps in bone resorption in the vicinity of the implant. Additional surgery for the elimination of implants is not essential because Mg alloy naturally deteriorates in living tissue [6]. However, implants made up of Mg alloy typically undergo rapid electrochemical disintegration in the physiological environment at high chloride ions concentration. Before fracture heals, rapid corrosion of Mg alloys not only compromises its mechanical integrity but also increases the alkalinity of surrounding tissues. These shortcomings of Mg alloys in clinical applications can be overcome by various chemical treatments and biocompatible surface coatings [7,8].

Bioactive glasses (BG) are recognized material for bone regeneration applications, which contain calcium and phosphate ions in similar proportion to the bone hydroxyapatite. These materials are currently used as bone grafts, scaffolds and coating material in orthopedics due to their bone-bonding ability and biocompatibility [9]. In the case of BG, more than 2.6 non-bridging oxygen ions are constituted in silica tetrahedron and cause bioactivity of the materials [10]. Due to the bioactivity of BG, hydroxyapatite forms its contact surface with physiological fluids and integrates with soft/hard tissue. The contents of BG differ from the conventional soda-lime-silica glasses constituting more than 65 wt. % of silica. The composition required for a glass for its bioactivity are SiO_2, Na_2O, CaO, and P_2O_5 [11]. The bioactive nature of BG can function as an excellent coating material by well-integrating implants with host tissue through hydroxyl apatite formation at the implant-tissue interface and can even stop the corrosion behavior of Mg alloys. Excellent adherence as well as mechanical strength and uniformity of BG coating on implants is possible only with a biocompatible polymer [12].

Chapter 2: Zein_Bioactive Glass Nano Composite Coating on Magnesium Alloy Substrate for Orthopedic Applications

Zein, derived from the endosperm of maize, is a macromolecular protein with a lengthy chain that falls under the prolamins family. Zein has effective film-forming capabilities due to its chemical structure, degree of polymerization, and molecular weight. Since it is also amphiphilic, it can be blended with both hydrophilic as well as hydrophobic materials for tailored properties. Importantly, zein is a suitable material for biodegradability, biocompatibility cell attachment, and proliferation capabilities [13]. These attractive properties have made zein the most suitable polymer in combination with bone regenerative BG as zein and BG (zein_BG) composite coating on a temporary degradable Mg alloy surface.

Several coating methodologies are being used to coat implant surfaces, such as thermal spraying, plasma spraying, physical vapor deposition, radio frequency sputtering, electrophoretic deposition, and dip coating [14,15]. Among all, dip coating is a sustainable and reproducible method, which does a uniform coating on a solid surface via a liquid suspension at room temperature. A few researchers have shown successful deposition of biopolymer _BG composite coating on alloy surfaces by electrophoretic deposition [16,17]. The electrophoretic deposition needs a judicious choice of solvent media and only conducting substrates. In addition, organic solvents are common media for electrophoretic deposition, which has environmental concerns. Aqueous electrophoretic deposition is expensive and uneconomical for electrophoretic deposition[18].

The present study is aimed to synthesize BG nanoparticles by a bio-inspired method using CTAB as a template. The obtained BG powder was mixed with zein solution and the resulting zein_BG composite was dip-coated on the Mg alloy surface at room temperature. Both BG and zein_BG coated Mg alloy substrates were analyzed using X-ray diffraction (XRD), scanning electron microscopy (SEM), energy dispersive spectroscopy (EDS), thermogravimetric analysis (TGA), and Fourier transform infrared spectroscopy (FTIR) along with only zein coated Mg alloy as a control sample. Nano size of BG particles was confirmed by transmission electron microscope (TEM). Using the biopolymer zein, the Mg alloy substrate is dip-coated both with and without the BG nanoparticles. In addition, corrosion characteristics of zein and zein_BG coated Mg alloy substrates were subjected to weight loss analyses, potentiodynamic polarization, and electrochemical impedance

spectroscopy (EIS) in the presence of Hanks balanced salt solution (HBSS) at 37 ℃. The coated Mg alloy substrates are also tested for mechanical properties, wettability, adhesion strength, and surface roughness. The degradation of the uncoated and coated alloy materials is tested by hydrogen evolution in HBSS solution and subjected to an X-ray photoelectron spectrometer (XPS) for surface characterization.

2. 2. Experimental Procedure

2.2.1. Materials

Zein powder (CAS number 9010-66.6), cetyltrimethylammonium bromide (CTAB) (CAS No- 57-09-0), tetraethyl orthosilicate (TEOS) (CAS No- 78-10-4), triethyl phosphate (TEP) (CAS No- 78-40-0), sodium acetate (NaAC) (CAS No- 127-09-3), calcium acetate (CaAC) (CAS No- 114460-21-8) and Hanks' balanced salt solution (HBSS), which is otherwise called simulated body fluid (SBF) were purchased from a standard chemical company, Sigma-Aldrich, USA. AZ31B magnesium (Mg) alloy (composition in **Table 2.1**) was obtained from Parshwamani Metals, Mumbai, India. All other chemicals used throughout the study were of AR grade with high purity. In this investigation, Milli Q water was utilized. All the experimentations were performed in triplicated and analyzed for error prediction using Analysis of Variance (ANOVA) from Origin Lab 2021 software.

Table 2.1: Composition of AZ31B Mg alloy.

Element	Al	Zn	Mn	Mg
Wt. %	2.4	0.5	0.05	Bal.

2.2.2. Synthesis of Bioactive Glass

An aqueous solution of 10 mM tris (hydroxymethyl) aminomethane (TRIZMA) buffer at pH 8 was prepared by dissolving 61.4 mg/mL of TRIZMA HCl and 74 mg/mL of TRIZMA base in Milli-Q water. The CTAB stock solution was prepared by mixing 1 mg/mL of CTAB in 100 mL of 10 mM TRIZMA buffer solution at pH 8. In 100 mL CTAB (1 mg/mL) solution in TRIZMA buffer at pH 8, the BG precursors namely TEOS (9.29 g), TEP (1.0 g), NaAC (6.36 g), and CaAC (4.21 g) were consecutively added at an interval of 30 min **(Scheme 1)** and kept for continuous stirring at 37 ℃ overnight as per our earlier

procedure [19]. Following this, the resulting white BG precipitate was centrifuged and washed with 70 % ethanol to remove unreacted components.

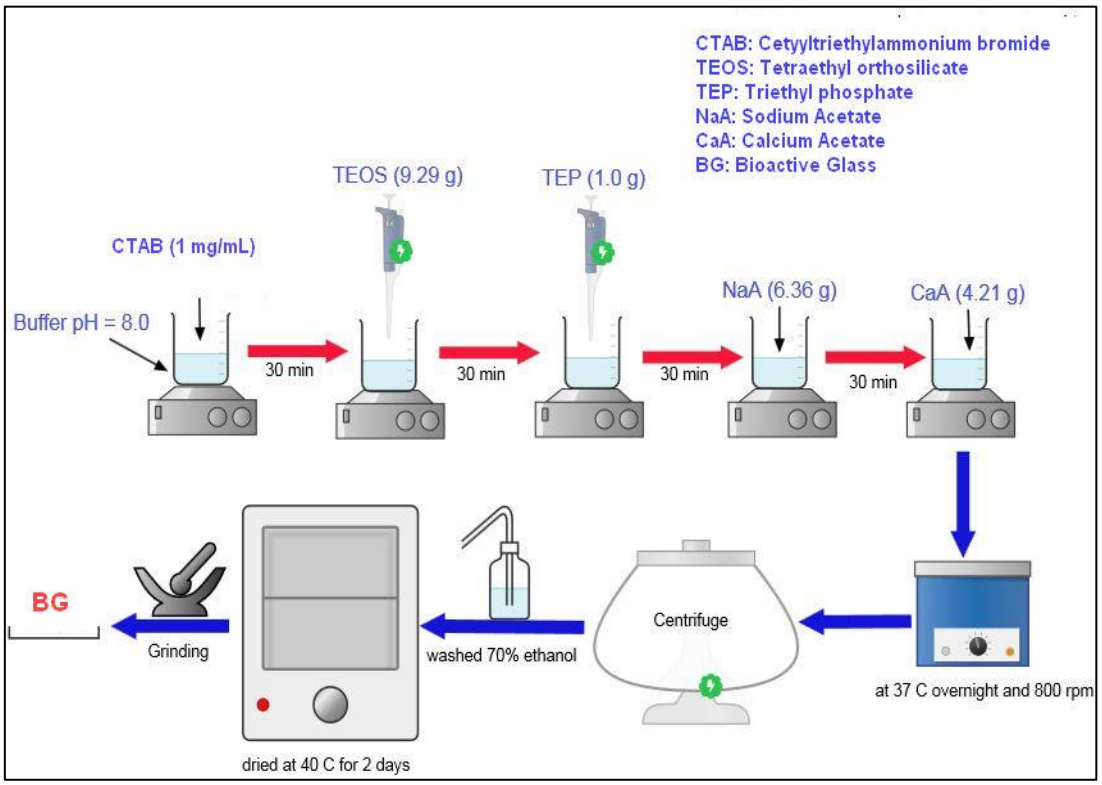

Scheme 1: Schematic representation depicting CTAB templated BG synthesis.

2.2.3. Dip Coating Procedure

A hole (2mm diameter) was drilled in AZ31B Mg alloy of size (20 mm × 10 mm × 4 mm) and was also brazed using silicon carbide paper (220 – 2000 grits). The alloy surface was cleaned using ultrasonication for 10 min with acetone to remove impurities followed by air drying. A 100 ml of 1.2 wt % zein solution was prepared in 20 % ethanol solution by heating to 37 ℃ using a hot plate and kept for continuous stirring for 30 min to ensure homogeneity. The pH of the zein solution was kept at 7.0 by acetic acid, mixed with 0.025 wt % of BG, and sonicated for an hour in ultra-sonicator bath. Then the Mg alloy was submerged for 2 h in zein_BG suspension, removed, and air dried for 15 min before being baked at 40 ℃ in an oven overnight. Similarly, the Mg alloy surface was also coated with zein alone.

2.2.4. Characterization studies

2.2.4.1. Morphological Analysis

The surface morphology and size of BG were recorded using Transmission electron microscopy (TEM) (CM200 – FEG – Philips) operating at an accelerating voltage of 200 kV as well as required magnification and elemental content. The BG particle size was analysed using ImageJ bundled with 64-bit Java 1.8.0_172 software.

Zein and zein _ BG coated Mg alloy substrates were subjected to scanning electron microscopy (SEM) (FEI Quanta 200 F) at 500 X magnification and an accelerating voltage of 20.0 kV. The uncoated and coated Mg alloy samples were also visualized through optical microscopy at magnification (1000 X) after immersing with HBSS.

2.2.4.2. Energy Dispersive Spectroscopy (EDS)

Energy dispersive X-ray spectroscopy was performed to find the chemical composition of zein and zein_BG coatings on the Mg alloy surface using the detector XFlash 6|60 part of Quanta 650 (FEI).

2.2.4.3. Fourier Transform Infrared Spectroscopy (FTIR):

Native BG as well as zein and coated Mg alloy substrates (zein and zein _BG) were subjected to FTIR analysis using NICOLET 380 FTIR spectroscopy. The FTIR spectrometer was operated in the spectral range of 4000 cm^{-1} to 400 cm^{-1} with a resolution of 1 cm^{-1}.

2.2.4.4. Thermogravimetric Analysis (TGA):

The thermal stability of native zein as well as BG and zein _ BG composite film samples were investigated using a thermogravimetric analyzer (SDT, Q600, TA instrument). Under a nitrogen atmosphere, the substrates were gradually heated from room temperature to 800 ℃ at a rate of 5 ℃ per minute. Throughout the heating process, a constant nitrogen flow rate of 50 mL/min was maintained.

2.2.4.5. X-ray Diffraction (XRD) Analysis:

XRD analysis on native zein as well as BG and zein _ BG composite film substrates was performed using a BRUKER D4 X-ray diffractometer operating at 30 kV and 15 mA

with the Cu- Kα radiation at room temperature. For analysis, the 2θ range of 5° to 90° with a step size of 0.01 and a counting time of 6s per step was maintained**.**

2.2.4.6. Contact Angle Measurement

The contact angle of water drops (20 µl of deionized water) on the coated and uncoated (zein and zein _BG) surface of the Mg alloy substrates was measured using a DSA25 drop shape analyzer, Kruss Scientific, India. The image of a sessile drop at the points of intersection (three-phase contact points) between the drop contour and the projection of the surface (baseline) was used for the measurement.

2.2.4.7. X-ray Photoelectron Spectrometer (XPS)

The elemental composition of zein_BG coatings on the Mg alloy surface was investigated by XPS before and after immersion in HBSS. The analyses were performed using the VGESCALAB II system with AlK_{α} radiation of energy1486.6 eV. The binding energies were determined regarding the C1s line at 285.0 eV (from an adventitious carbon).

2.2.4.8. Surface Roughness Tests

The surface roughness of the uncoated and coated Mg alloy substrates was tested by TR-100 (TestLab) surface roughness tester by following ASTM (D3359-B) protocol. For the adhesion test, a perpendicular lattice pattern with 12 cuts in each direction was made through the alloy sample surface and a prescribed pressure-sensitive tape was applied over the lattice and then removed. To assess the adhesion of the film, a 0 to 5 scale was utilized, and it was evaluated by comparing with standard descriptions and illustrations.

2.2.4.9. Corrosion Characterization

The corrosion behavior of the uncoated and coated (zein and zein_ BG) Mg alloy substrates was assessed after immersing in HBSS at pH 7.4 for (3, 7, and 10) days at 37 ℃ by weight loss method followed by microscopic examination and electrochemical impedance spectroscopy (EIS) analysis. The clean alloy substrates were weighed before and after immersing in HBSS as per ASTM G61 – 86 procedures. The corrosion rate (CR) and protection efficiency (PE %) of the alloy substrates were calculated by using EQs. (2.1) and

(2.2) as given below [20] :

$$CR\ (mg/cm^2.d) = \frac{w_2 - w_1}{A\ t} \quad (2.1)$$

$$PE\ \% = \frac{(CR\ uncoated - CR\ coated)}{CR\ uncoated} \times 100 \quad (2.2)$$

Where; w_1 & w_2 are the weight of substrates before and after immersion; respectively.

A; area of the sample (cm^2) and t; time (h).

An electrochemical analyzer (PAR Model 2273, Princeton, USA) was employed to acquire the potentiodynamic polarization curve and electrochemical impedance spectra (EIS).A three-electrode cell set-up was used in which the prepared substrates with an exposed area of (1.0 cm^2) were the working electrode (coated sample), saturated calomel electrode (SEC), and a platinum sheet were used as the reference and counter electrodes, respectively. The polarization started from -2.0 V to -1.0 V at a scan rate of (1 mV/s). The electrochemical parameters corrosion potential (E_{corr}, V), corrosion current density (I_{corr}, A/cm^2), and Tafel slopes (β_a & β_c) (V dec^{-1}) were fitted using the Tafel extrapolation method. EIS was recorded at open circuit potential for 10-mV sinusoidal amplitude over a frequency range of 100 kHz to 0.01 Hz. The obtained EIS Nyquist plots were analyzed using ZSimp Win software (version 3.1 USA) and were best fitted to the appropriate equivalent circuit model. A stable open circuit was established within 1 h before the EIS testing. The experiment was conducted in HBSS.

The polarization resistance (R_p, V) and corrosion protection efficiency (% IE) were calculated using Eq.(2.3)[21] :

$$R_p = \frac{\beta_a \beta_c}{2.303\ I_{corr}\ \beta_a \beta_c} \quad (2.3)$$

Where; β_a and β_c are anodic and cathodic slopes (V dec^{-1}); respectively.

2.2.4.10. Hydrogen Evolution Test

To conduct the hydrogen evolution test, an experimental setup was devised as described below. The substrates were immersed in HBSS at a temperature of 37 ℃, positioned beneath an inverted funnel. The funnel was connected to a graduated burette, which was properly sealed. Throughout the test, the water level in the burette was periodically measured over a duration of 240 h, with the substrates fully exposed to the surface.

2.3. Results and Discussion

In the present study, CTAB templated BG synthesis was carried out by a bio-inspired approach by sequential addition of TEOS, TEP, NaAC, and CaAC as per our earlier procedure [22,23]. The template is well known for directing the particle size including textural features of BG through micellar aggregation [22]. The CTAB micellization results in higher positive charge density at its surface. Initial addition of TEOS hydrolysis at pH 8 results in negatively charged silica molecules. The charge attraction between negatively charged silica and positively charged CTAB micellar aggregation leads to heterogeneous nucleation of the SiO_2 network on the micellar surface. Further TEP addition in the reaction mixture similarly includes P_2O_5 in the existing SiO_2 network and is followed by the homogenous nucleation of the other precursor molecules. This includes the formation of Na_2O and CaO, which are network modifiers and occupy the interstitial sites of the network and resulting in the formation of BG nanoparticles. The interesting structure directing property of template in the synthesis of other oxide materials through bioinspired approach has been well demonstrated in the literature [24].

2.3.1. Material Characterization

2.3.1.1. TEM

The TEM micrograph of the BG sample is portrayed in **Fig. 2.1(a).** Based on the micrographs, BG particles were of more or less uniform spherical shape with aggregated morphology. An average particle size of 6.67 ± 0.06 nm was reported by image J analysis software on TEM micrographs **Fig. 2.1(b).**

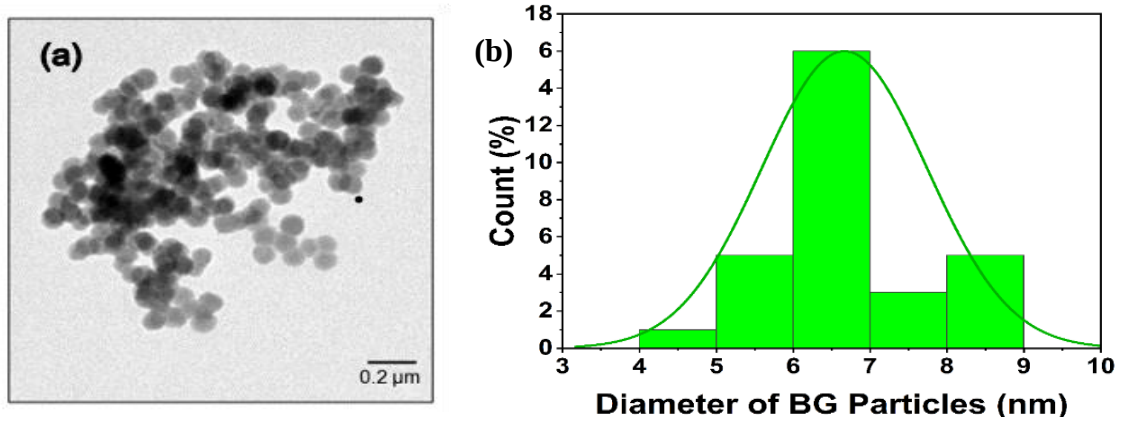

Fig. 2.1: (a) TEM micrograph of BG particles and **(b)** Average particle diameter of BG ImageJ analysis software (included with 64-bit Java 1.8.0 _ 172) was used to analyses the particle size distribution from TEM micrograph.

2.3.1.2. FTIR

The FTIR spectrum for native **zein** protein is portrayed (**Fig. 2.2(b)**). The Broadband corresponding to stretching of the N-H and O-H bonds (amide A) of protein appeared between 3500 cm^{-1} to 2800 cm^{-1}. Amide I band corresponding to stretching of carbonyl (-C=O) group of peptide bond was seen at 1655 cm^{-1}. Amide II band due to angular deformation of N-H as well as C-H stretching vibrations were reported at 1528 cm^{-1} and -COO^- symmetrical stretching was seen as a small peak at 1439 cm^{-1}. Due to the deformation of the C-N bond, a small shoulder at 1246 cm^{-1} (amide III) appeared. The FTIR spectrum of **BG** showed a broad band centered around 3451 cm^{-1} and a small shoulder at 1615 cm^{-1} due to O – H stretching as well as bending vibrations of silanol groups of BG and absorbed water molecules. As per our previous reports a sharp peak reported at 1572 cm^{-1} was assigned to C – O stretching group of the template molecule (CTAB)[25]. The peaks at 1422 cm^{-1} and 788 cm^{-1} were assigned to bending vibrations of Si–OH and Si – O – Si groups, respectively. The intense band centered at 1100 cm^{-1} was due to the P – O bending vibration. A small shoulder reported at 973 cm^{-1} corresponds to the Si – O stretching bond. The reported native zein and BG FTIR spectra is in line with earlier findings [26].

Zein_BG FTIR spectrum contains a characteristic zein peak due to amide I (1660 cm^{-1}), amide II (1536 cm^{-1}), and due to C-N bending (1239 cm^{-1}). Apart from characteristic zein peaks, BG peaks were also seen in the zein_BG sample. For example, peaks due to bending vibrations of Si – OH (1444 cm^{-1}), Si – O – Si (702 cm^{-1}) along with a small shoulder due to P – O bending (1100 cm^{-1}) as well as Si – O stretching (929 cm^{-1}). Interestingly, amide I and amide II peaks of zein in zein_BG were slightly shifted to a higher wavenumber (about 5 cm^{-1}) compared to native zein, which confirms the physical interaction between zein and BG particles in the zein_BG sample. Similarly, the characteristic Si – OH (1444 cm^{-1}), bending vibrations of BG in zein_BG showed about 1422 cm^{-1} shifts compared to native BG confirming a chemical interaction between BG and zein in zein_BG. On the other hand, the Si – O – Si (702 cm^{-1}) bending vibration of zein_BG appeared as a small broadband at the lower wavenumber compared to the Si – O – Si (788 cm^{-1}) sharp peak of native BG.

2.3.1.3. XRD

The XRD patterns of native zein coating and BG nanoparticles, as well as zein _ BG composite coating, are shown in **(Fig. 2.2(c)).** XRD pattern of **zein** indicated two broad diffracting domains (2θ) centered at 9.2^{o} and 20.3^{o}. The characteristic diffractions of zein in the 2θ range of 9.2^{o} and 20.3^{o} revealed the average intermolecular distances of the skeleton in the α-helical structure of the protein (4.6°) and α-interhelix diffracting domain (8.96°) in zein ; respectively [19]. Native **BG** powder showed a broad hump in 2θ range of 18° to 30° indicating the amorphous nature of the sample. The XRD pattern of the **zein _BG** showed two broad diffracting domains of zein centered around 2θ range of 9.8^{o} and $19.2^{o.}$ along with few other diffracting domains at 2θ values of 28.6° and 38.7°. The observed diffraction maxima correspond to JCPDS Card No.: 01-084-0151 (Na_3Ca (SiO_3) (PO_4)).

2.3.1.4. TGA

The TGA curve of zein and BG powder and zein _ BG film are shown in **(Fig. 2.2(a)).** For **zein**, the initial weight loss of 8.2 wt % at 103.4 ℃ was because of the elimination of water molecules. Thereafter weight (93.4 wt %) of the sample remains more

or less the same up to 255 ℃ and drastically reduced to 15.8 wt % at 364.6 ℃ indicating the degradation of zein. After 364.6 ℃ a complete degradation of the protein was reported. For **BG** the initial weight loss of (15.7 wt %) occurred at the temperature around 77 ℃ due to the adsorbed water. Further, a slight gradual weight loss (28.1 wt %) was reported indicating loss of remnant CTAB template molecules up to around 325 ℃. Thereafter, up to 442 °C, around 47.8 wt % of BG remained after the stabilization of the inorganic network and remained more or less constant up to 800 ℃. **Zein _BG** film showed initial weight loss of 14.1 wt % in the temperature range 34.6 ℃ – 94.7 ℃ due to loss of adsorbed and occluded water molecules. The major weight loss of 74.34 wt % was reported between the temperature range of 216 ℃– 318 ℃ indicating the degradation of zein as observed in the case of native zein molecule. Thereafter, 28 wt % remnant of the zein_BG composite confirms the existence of the BG inorganic network. Remarkably, the range of zein degradation in the zein_BG composite was reported more or less the same (216 ℃– 373 ℃) compared to native zein (251 ℃– 375 ℃) indicating the existence of zein in the composite as observed by FTIR **(Fig. 2.2(b)).**

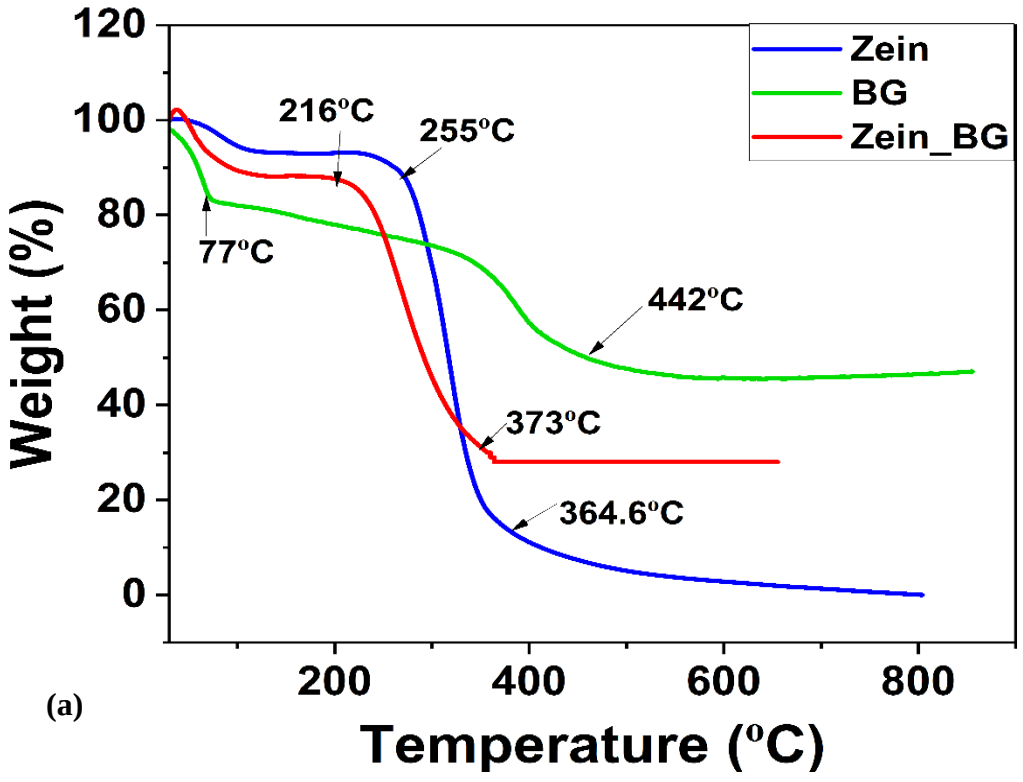

(a)

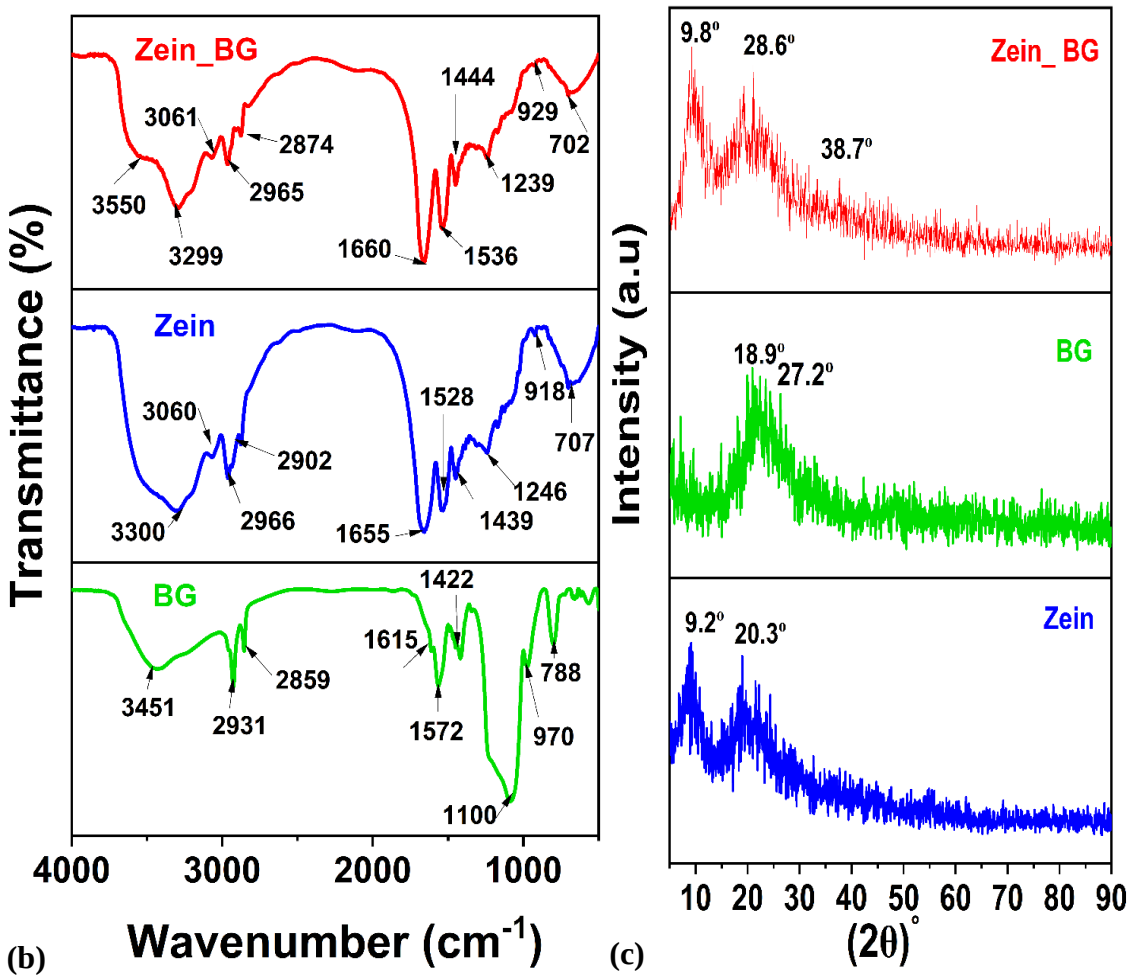

Fig. 2.2: (a) TGA **(b)** FTIR spectra and **(c)** XRD patterns of BG nanoparticle, zein and zein_BG coating on the Mg alloy substrate.

2.3.1.5. SEM

Fig. 2.3 (a and b) shows SEM images of Mg alloy substrates coated with zein and zein _ BG respectively at 500 KX magnification and 20 µm resolution. Zein deposition on the Mg alloy surface was fairly uniform with porous microstructure as reported in the literature [22]. SEM micrographs of the Mg alloy surface deposited with zein_BG composite displayed a denser rough surface coverage compared to the zein surface. In zein_BG film, BG particles were well integrated with zein. The reported integration supports the findings of FTIR **(Fig. 2.2(b)),** which evidenced physical and chemical bonding between zein and BG in the zein_BG composite.

The cross-sectional SEM images at 1.00 KX magnification and 20 μm resolution of the zein and zein_BG coated Mg alloys are presented in **Fig. 2.3 (c and d),** respectively. As per the micrographs, the thickness of zein and zein_BG coatings on Mg alloy were observed as 14.65 μm and 27.26 μm, respectively. zein_BG coating on Mg alloy was visualized as more compact than zein coating on the alloy substrate.

The chemical composition of zein and zein_BG coated Mg alloy surfaces were obtained by EDS analysis and are shown in **Fig. 2.3 (e and f).** The EDS results demonstrated the existence of Mg, C, O, and P on the zein-coated alloy surface. Zein_BG coated alloy surface was reported with Mg, Si, C, O, and P. From the intensity of the EDS spectra, the wt (%) of Mg, Si, C, O, and P were obtained. The results showed the higher distribution of C , O, and P for native zein coating, while after the addition of BG in zein_BG, the amount of P and O was increased due to the presence of Si in the composition of BG [13].

The above findings evidence zein_BG composite formation as follows: The plant protein zein contains both hydrophobic amino acids as well as hydrophilic residues and as a whole zwitterionic with complex molecular structure. In detail, the zein molecule is composed of both negatively charged deprotonated hydroxyls, and carboxyl, as well as phenols and also positively charged protonated amines and amides [27]. These functional groups are likely to interact through physical as well as chemical interaction **(Fig. 2.2 (b))** with negatively charged BG particles and result in zein_BG composite formation.

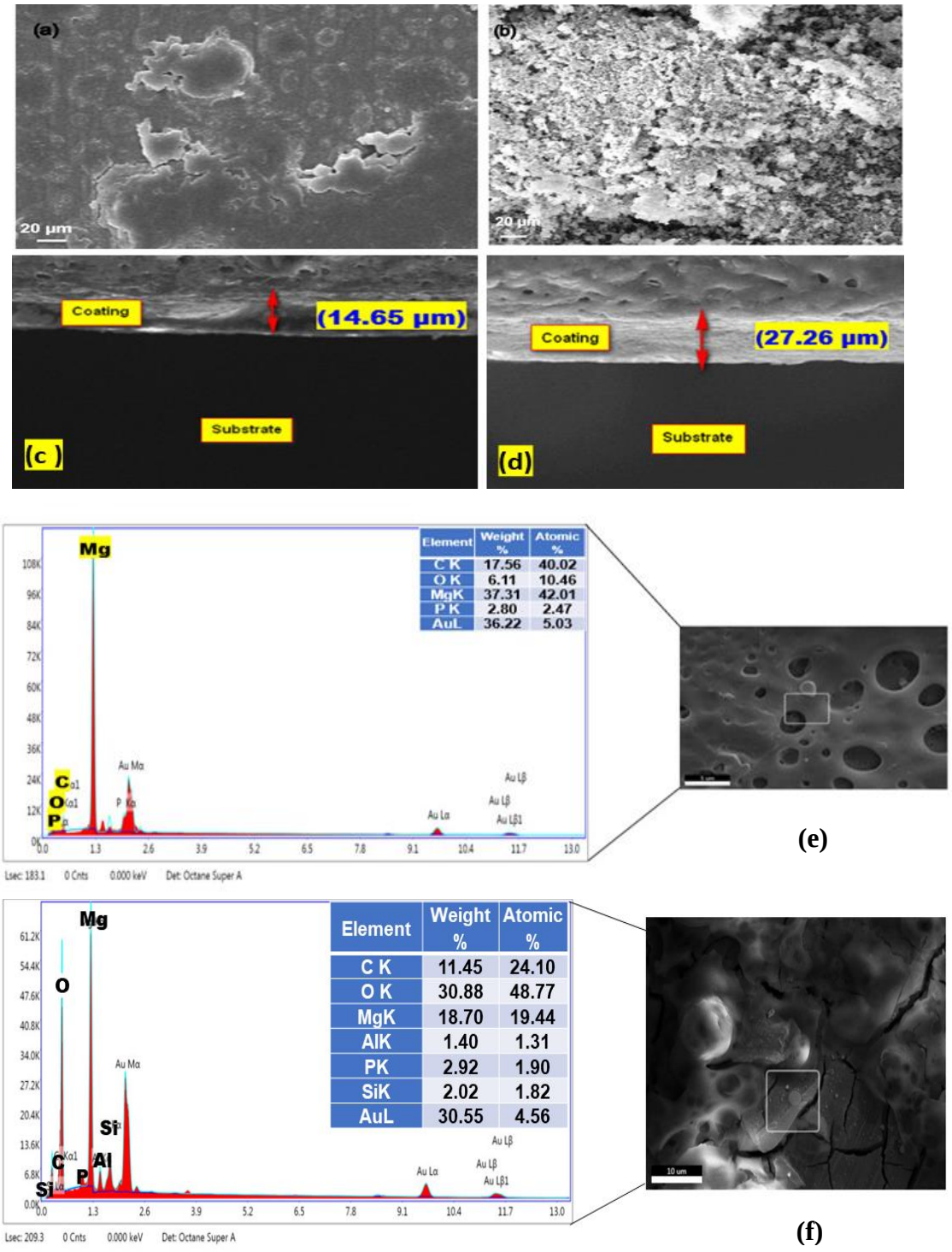

Fig. 2.3: (a & b) SEM micrographs at 500X magnification and 20.0 kV accelerating voltage, **(c & d)** Cross – sectional view and **(e & f)** EDS anlysis on zein and zein _ BG coated Mg alloy substrates; respecively.

2.3.2. Surface Wettability and Roughness

Surface wettability and roughness determine the performance of coated substrate by enhancing the reactivity between the coating and the host tissue. The value of the contact angle determines the hydrophilicity or hydrophobicity of the surface. Surfaces with > 90° contact angle are hydrophobic, whereas surfaces with < 90° are hydrophilic [28–30] .**Fig. 2.4(a)** reports water contact angle data of uncoated and coated (zein and zein_BG) Mg alloy surfaces. The contact angle of the native Mg alloy substrate was 70.6° ± 3.7°, which indicates the hydrophobic nature of the alloy surface. After zein coating, the water contact angle of the Mg alloy surface reduces to 31.7° ± 2.7°. The reported reduction in the value of contact angle 70.6° ± 3.7° (uncoated) to 31.7° ± 2.7° (zein coated) indicates the interaction between the hydrophobic part of amphiphilic zein protein (amino acids such as; proline, leucine, isoleucine, alanine) with hydrophobic alloy surface. As a result, the hydrophilic (glutamine) portion of the protein is exposed on the zein-coated alloy surface and reduces the value of contact angle (31.7° ± 2.7°) compared to uncoated alloy surface (70.6° ± 3.7°) [31]. Interestingly, zein_BG coating on the Mg alloy surface (30.3° ± 2.3°) was reported with the water contact value, which is very similar to that of zein coated substrate surface (31.7° ± 2.7°). The observation indicates that hydrophilic silanol (Si-OH) groups of BG particles interact with hydrophilic zein molecules and retain the overall wettability more or less the same. As a result, the hydrophilic zein_BG coating on the Mg alloy surface makes the substrate a suitable implant material for excellent performance.

The surface roughness of uncoated and coated (zein and zein_BG) Mg alloy surfaces are portrayed In **Fig.2. 4 (b).** The Mg alloy substrates coated with zein (R_a = 1.2 μm ± 0.02 μm) and zein_ BG (R_a = 1.4 μm ± 0.06 μm) significantly displayed more surface roughness compared to the bare substrate (R_a = 0.1 μm ± 0.005 μm). Interestingly, maximum surface roughness was reported for zein_BG coated substrate, which is in line with the required surface roughness for attachment and growth of osteoblast-like cells and bone marrow-derived ST-2 cells[14].

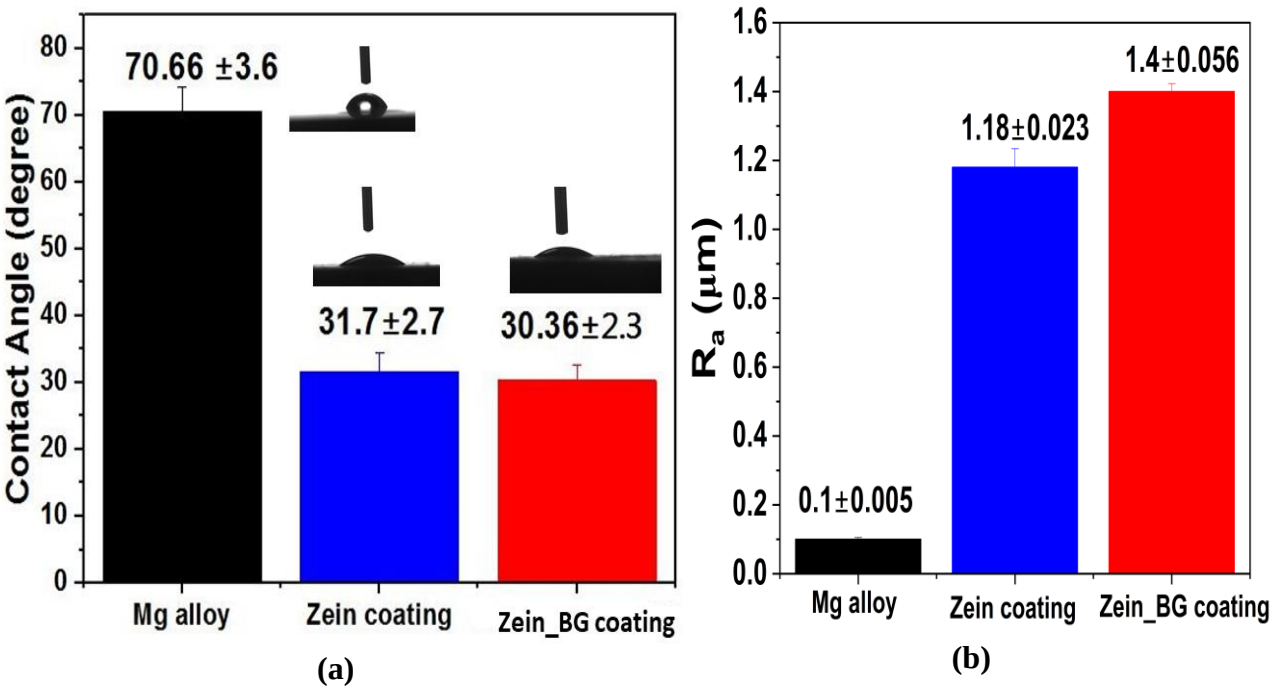

Fig. 2.4: (a) Water contact angle measurements and **(b)** surface roughness of uncoated and coated (zein and zein_ BG) Mg alloy substrates.

2.3.3. Adhesion Test

Mechanical integrity and long-term durability of coating materials are highly influenced by how well the coating adheres to the substrate [32,33]. To evaluate the adherence of zein and zein_BG coatings, a tape adhesion test was performed on coated Mg alloy substrate and inspected under an optical microscope after removing the tape as per ASTM (D 3359 – B) **(Fig. 2.5 (a and b)).** Zein-coated substrate **(Fig. 2.5(a))** was observed to lose the integrity of coating at the edge and on the surface of a few squares. The affected surface area was reported in the range of 15 % – 35 % for zein coating. In the case of zein _ BG coating **(Fig. 2.5(b)),** only a small portion of the coating was delaminated at the intersection of squares, which is less than 5%.

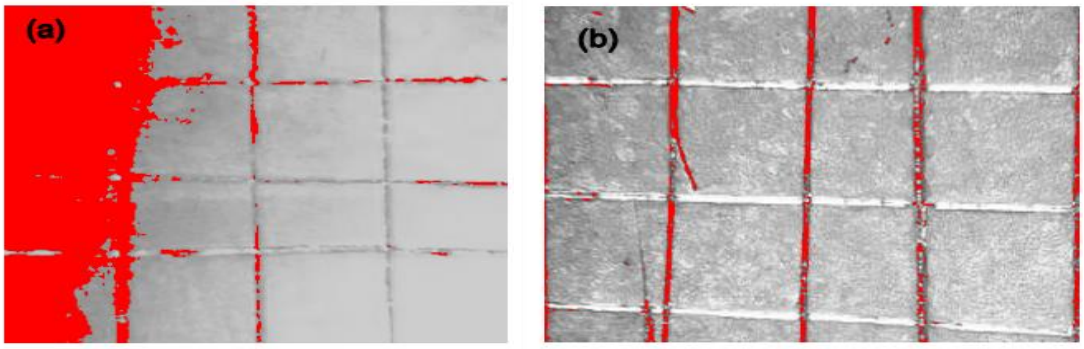

Fig. 2.5: Microscopic images of adhesion test results on **(a)** Zein coated and **(b)** Zein_ BG coated Mg alloy surfaces.

2.3.4. Corrosion Behavior Evaluation

The findings of weight loss tests on the uncoated and coated substrates were compiled in **(Table 2.2)** after 3, 7, and 10 d of submergence in HBSS at 37 ℃. In general, the weight loss of the Mg substrate increased with the immersion time in HBSS. The uncoated Mg showed the highest incidence of corrosion by reporting the highest weight loss (60.1 mg ± 0.94 mg) after 10 d of interaction with HBSS. Since the bare Mg alloy surface was highly susceptible to fluid and air, the highest weight loss was reported after HBSS treatment on the polished specimen surface. Zein and zein_BG coated Mg alloy surfaces showed resistance to fluid, as well as air penetrating through the surface and resulted in 15.7 mg ± 0.25 mg and 8.0 mg ± 0.12 mg weight loss respectively after 10 d treatment with HBSS. The zein_BG coated substrate indicated the maximum protection efficacy (95.99 %) after 3 d immersion with HBSS and demonstrated the efficiency of zein_BG coating on the substrate.

The electrochemical polarization curves of uncoated Mg alloy, zein, and zein_BG coated Mg alloy substrates are shown in **(Fig. 2.6).** The corrosion potential (E_{corr}) of the uncoated Mg alloy substrate was observed as -1.62 V_{SCE} and was increased to -1.302 V_{SCE} after zein coating. Interestingly, for zein_BG coated alloy substrate, the highest E_{corr} was reported (-1.240 V_{SCE}) among uncoated and zein-coated substrates. The reported E_{corr} values of uncoated and coated substrates indicate that the BG nanoparticles in zein_BG

composite could resist the penetration of ions from HBSS due to their bioactive nature [34]. Electrochemical parameters of uncoated, zein and zein_BG coated Mg alloy substrates in HBSS are listed in (**Table 2.3)**. The value of the corrosion current density (I_{corr}) for zein coating was reported as 6.28 E^{-6} $A.cm^{-2}$, whereas for zein_BG coating I_{corr} = 2.41 E^{-6} $A.cm^{-2}$. The observed lower I_{corr} value for zein_BG coating compared to the zein coating on the alloy substrate is attributed to its higher thickness and uniformity as reported by SEM analysis **(Fig. 2.3).**

The observed fluctuations in the anodic polarization curves **(Fig. 2.6)** of the zein and zein_BG-coated Mg alloy substrates are due to the evolution of hydrogen gas at the cathode, which ruptures the coating and leaves the substrate surface. A corresponding increase in R_p values of coated Mg alloy substrates (zein coating, 1.56 E^{+3} $\Omega.cm^2$ and zein_BG coating 2.05 E^{+3} $\Omega.cm^2$) was observed compared to uncoated substrate (1.15 E^{+2} $\Omega.cm^2$) (**Table 2.3**). The reported huge increase in R_p values for zein and zein_BG coated substrates indicate the thicker and uniform coverage of the coating material on the alloy surface [35].

Interestingly, the corrosion rate of zein_BG (0.86 mm/year), and zein coated (1.85 mm/year) substrates are significantly lower compared to the uncoated Mg alloy (6.95 mm/year). The use of BG particles in coating the implant materials are well known to reduce their corrosion rate due to the bioactivity [27].

Table 2.2: The weight loss data of uncoated and coated (zein and zein_BG) Mg alloy substrates after immersion with HBSS for 3, 7 and 10 d at 37 ℃.

S.N.	Type	Days	Δw (mg)	CR ($mg/cm^2.d$)	PE %	Θ
1	Un coated Mg alloy	3	5.8464	0.3045	-	-
2		7	32.3097	0.7212	-	-
3		10	60.1024	0.9391	-	-
4	Zein	3	0.6393	0.0333	89.0640	0.8906
5		7	4.3722	0.0989	86.2839	0.8628
6		10	15.7184	0.2456	73.8473	0.7384
7	Zein _ BG	3	0.2342	0.0122	95.9934	0.9599
8		7	3.0464	0.0680	90.5712	0.9057
9		10	7.9552	0.1243	86.7639	0.8676

Table 2.3: Electrochemical parameters of uncoated and coated (zein and zein_BG) Mg alloy substrates in HBSS for 10 d at 37 ℃ obtained from linear polarization test.

Type	E_{corr} (V/SCE)	I_{corr} ($A.cm^{-2}$)	βa ($V.dec^{-1}$)	βc ($V.dec^{-1}$)	R_p ($\Omega.cm^2$)	CR (mm/years)
Un coated Mg alloy	-1.62	3.04×10^{-4}	0.19	0.16	1.15×10^{2}	6.96
Zein coated	-1.30	6.28×10^{-6}	0.49	0.19	1.56×10^{3}	1.85
Zein_BG coated	-1.24	2.41×10^{-6}	0.12	0.11	2.05×10^{3}	0.86

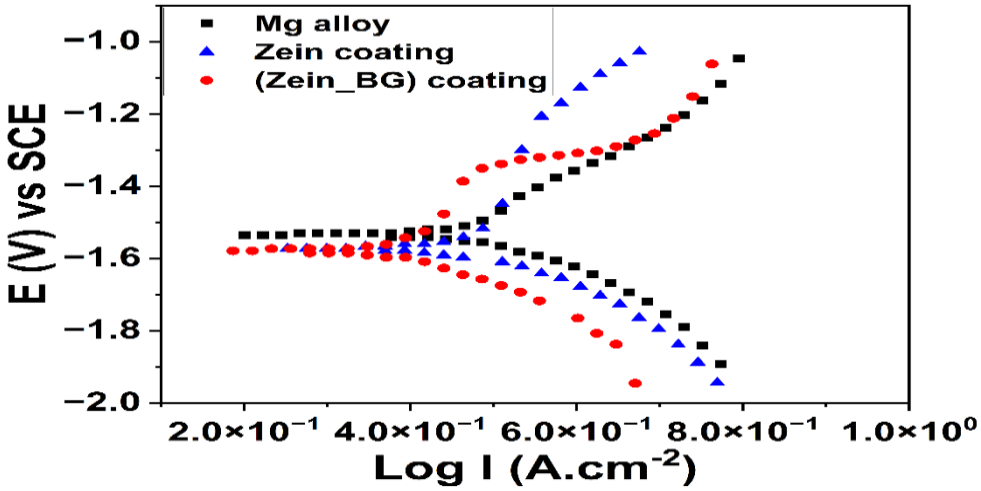

Fig.2.6: Potentiodynamic polarization curves of uncoated and coated (zein and zein_BG) Mg alloy substrates immersed in HBSS for 10 d at 37 ℃.

The corrosion-resistant performance of the uncoated, zein-coated and zein_BG-coated Mg alloy substrates can be further analyzed by EIS. The EIS spectra of the uncoated and coated substrates after 10 d of interaction in HBSS at 37 ^{o}C are shown in **Fig. 2.7(a, b, and c).** The EIS spectrum of the uncoated substrate portrayed a single small semicircle, whereas, zein coated Mg surface resulted in merged two semicircles with larger diameters. Interestingly, the EIS spectrum of the zein _BG coated substrate reveals merged two semicircles into the largest semicircle compared to zein-coated and uncoated surfaces. This observation revealed an increase in impedance and indicated the high corrosion resistance behavior of zein_BG coated substrate [36,37]. To obtain detailed information on the degradation processes at interfaces of the (uncoated and coated) substrates and HBSS

solution, the EIS data were also fitted using equivalent circuits **Fig. 2.7 (d, e, and f).** In this model, Rs corresponds to solution resistance between the reference electrode and working electrode and R_1, R_2, and R_3 are resistance due to surface deposits such as oxides/hydroxides, zein/zein_BG coating, and defects through the film respectively. C_1 represents the capacitance due to components of the zein/zein_BG coating (protective corrosion layer), and C_2 is the capacitance associated with the corroded coating after immersing with HBSS.

A constant phase element (CPE) in contrast to pure capacitive is used, defined by admittance (Y_0) and power index number (n), and can be calculated by following the formula [33]:

$$Y_{CPE}(\omega) = \frac{1}{Z_{CPE}} = Y_0 (j\omega)^n \quad (2.4)$$

where; Z_{CPE}, represents the impedance of the constant phase element.

j: imaginary unit and (ω) angular velocity (rad/sec)

Calculation of polarization resistance (Rp) values was estimated to evaluate the corrosion resistance of the systems under this study using R_p ($R_p = R_s + R_2 + R_3$)[38]. According to the proposed equivalent circuit model, EIS spectra were best fitted and obtained values of equivalent circuit parameters are listed in **Table (2.4)**. Interestingly, it can be observed that n_1 for zein_BG is 1.0, indicating a capacitive behavior but for uncoated Mg alloy, decreased to 0.14, which showed a diffusion process. These findings are consistent with the corrosion behavior of zein/45S5 BG-coated Mg substrate in SBF [39].

Table 2.4: Corrosion parameters obtained from the Nyquist fitted impedance data on uncoated and coated (zein and zein_BG) Mg alloy substrates.

Sample	R_s ($\Omega.cm^2$)	R_1 ($\Omega.cm^2$)	R_2 ($\Omega.cm^2$)	R_3 ($\Omega\ cm^2$)	CPE_1 ($\Omega^{-1}.S^n\ cm^{-2}$)	n_1	C_1 ($\Omega^{-1}.S^n\ cm^{-2}$)	CPE_2 ($\Omega^{-1}.S^n\ cm^{-2}$)	n_2	C_2 ($\Omega^{-1}.S^n\ cm^{-2}$)	CPE_3 ($\Omega^{-1}.S^n\ cm^{-2}$)	C_3 ($\Omega^{-1}.S^n\ cm^{-2}$)	n_3
Un coated Mg alloy	1.00×10^{-6}	1.00×10^{-6}	-	-	2.40×10^{-7}	0.1	1.21×10^{-10}	4.70×10^{-4}	0.99	4.51×10^{-4}	2.68×10^{-9}	-	0.83
Zein coated	$1.35\times10^{—3}$	5.40×10^{-26}	24988	-	5.00×10^{-9}	0.58	8.19×10^{-13}	1.90×10^{-7}	0.11	1.18×10^{-10}	3.34×10^{-10}	-	0.84
Zein _BG coated	$4.18\times10^{—1}$	4.10×10^{-4}	9.68×10^{-13}	4.31×10^{-13}	1.10×10^{-12}	1.0	5.00×10^{-4}	1.30×10^{-9}	0.8	8.50×10^{-11}	6.97×10^{-9}	1.20×10^{-10}	0.91

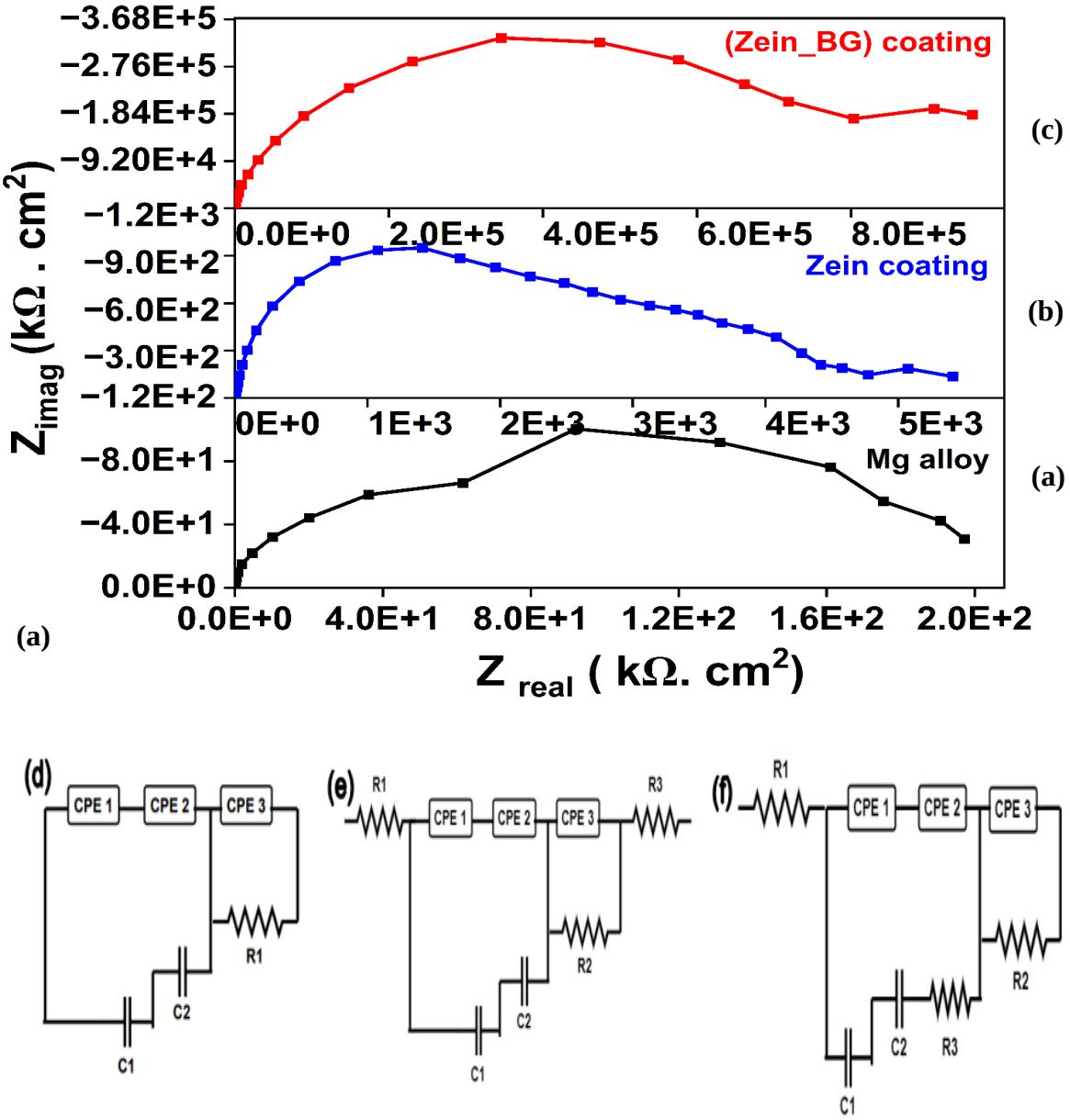

Fig. 2.7: (a) Nyquist plots of **(a)** uncoated , **(b)** zein and **(c)** zein_BG coated Mg alloy substrates after 10 d immersion in HBSS at 37 ℃, and **(d-f)** the corresponding fitted equivalent electrical circuits for the impedance data.

2.3.5. Analysis of Degradation Behavior

The volume of hydrogen gas released from uncoated and coated Mg alloy substrates immersed in HBSS is reported in **Fig. 2.8 (a)** as a function of time. The lowest amount of released hydrogen from the Mg alloy substrate due to the reaction with HBSS [40] exhibits the lowest corrosion rate. As observed in **Fig. 2.8 (a),** the zein and zein_BG coated substrates released the minimum volume of hydrogen gas, whereas the maximum volume of hydrogen gas was released by the uncoated Mg alloy and in good agreement with electrochemical measurements (Section 2.3.4).

The volume of released hydrogen gas from 24 h to 240 h of immersion in HBSS increases from 9.5 $ml.cm^{-2}$ to 73.4 $ml.cm^{-2}$ for uncoated Mg alloy, from 6.5 $ml.cm^{-2}$ to 48.7 $ml.cm^{-2}$ for zein coated substrate and from 3.5 $ml.cm^{-2}$ to 37.7 $ml.cm^{-2}$ for zein_BG coated substrate. After 72 h of immersion in HBSS, the hydrogen evolution was faster for all substrates. Among all substrates, zein_BG coated Mg alloy showed the lowest evolution of hydrogen due to the formation of thicker protective oxide layer on its surface after a longer time (>72 h) exposure to HBSS [41].

The elemental and chemical state of the zein_BG coated Mg substrate surface was analyzed before and after immersion in HBSS for 10 d at 37 ℃ using XPS **(Fig. 2.8 (b)).** The XPS survey scan on zein_BG coated Mg alloy substrate indicated that the existence of Mg1s (1303.39 eV), O1s (531.54 eV), C1s (284.97 eV),Ca2p (346.73 eV), P2p (133.11 eV) and Si2p (101.73 eV) before immersion in HBSS. The XPS peaks demonstrated the successful coating of zein_BG composite on the alloy substrate and in good agreement with the findings of FTIR, XRD, TGA and SEM **(Figs. 2.2 and 2.3).** After immersion in HBSS for 10 d, peaks corresponding to similar elements were also reported for the substrate as seen in the case of before immersion in HBSS. On the other hand, the XPS peaks of the substrate after interaction with HBSS were shifted to lower binding energy values for Mg1s (1303.33 eV), O1s (531.52 eV) and C1s (284.46 eV) compared to the control. In comparison with the control, XPS peaks corresponding to Ca2p (347.23 eV), P2p (133.21 eV) and Si2p (101.89 eV)) of the substrate after interaction with HBSS were emerged at higher binding energy values. These changes indicate the surface deposition of corrosion products of the Mg alloy substrate. In addition, bioactivity of BG contents of zein_BG composite on the coated alloy surface during immersion in HBSS also expected

to cause the observed shifts in binding energies of the reported elements.

High resolution XPS spectra of Mg1s, O1s, C1s, Ca2p, P2p and Si2p are further collected to reveal the chemical information of the existing elements, as shown in **Figs.2. 8(c) and 2.8(d).** For precise analysis, the resulted high-resolution peaks were subjected to Gaussian model fit using Origin Lab 2021 software and finding on the surface of Mg alloy substrates before and after immersion in HBSS are discussed below:

Bare Mg alloy surface showed XPS peaks correspond to Mg^{2+} (1303.54 eV Mg1s), O^{2-} (531.33 eV O1s), C – C (284.3 eV C1s), C= C (288.2 eV C 1s), Ca^{2+} (346.71 eV Ca2p), CaO (350.56 eV Ca2p) , P – O^{-} (132.78 eV P2p). P-OH (133.64 eV P2p), SiO_2 (101.37 eV Si 2P) and SiO_4 (101.31 eV) before immersion in HBSS[42] .The findings confirmed the existence of BG nanoparticles in zein_BG composite coating. The XPS analyses of Mg alloy surface after 10 d of interaction with HBSS report the following findings. The observed Mg1s peak at 1303.41 eV corresponds to $MgHPO_4.H_2O$[43]. O1s peak showing maximum at 531.34 eV indicates the existence of [$–OH^{-}$], [PO_4^{3-}], and [CO_3^{2-}] [44]. In most of Mg alloys, as the most dominant surface corrosion product is $Mg(OH)_2$ due to its low solubility compared to magnesium phosphate and magnesium carbonate[35]. In the C1s spectra, the peaks representing C1s at 284.10 eV and 285.56 evidenced the existence of $MgCO_3$ and $CaCO_3$; respectively on the alloy surface as corrosion products[43].

In Ca2p spectra, the higher sub – peak centered at (350.64 eV) corresponds to Ca2p1/2, proving the presence of calcium salts. The other peak centered at (346.63 e V) is Ca2p3/2 peak evidencing calcium-based corrosion products. The observation corresponds to existence of Ca^{2+} ions in the form of $CaHPO_4.H_2O$ and $CaCO_3$, which are the most possible corrosion products on the Mg alloy surface in HBSS [43]. P2p peaks observed at 132. 66 eV and 133.57 eV represent the existence of $Ca(PO_4)_2$ and $MgPO_4$[43]. Finally, the appearance of Si2p at 101.30 eV and 101.91 eV) evidences the existence of silicon containing species in the corrosion product layer such as SiO_2 [43]. In summary, the zein_BG coated Mg alloy could contain corrosion products composed of $Mg(OH)_2$, $MgHPO_4.H_2O$, $CaHPO_4.H_2O$, SiO_2 , $MgCO_3$ and $CaCO_3$.

Microscopic examination of uncoated and coated surfaces confirmed surface deposition of corrosion products **(Fig. 2.8 (e)).** The lowest surface deposition was visualized for uncoated substrate immersed in HBSS, which increased with an increase in contact time with HBSS (3 d to 10 d) as illustrated in **Fig. 2.8 ((a1) – (c1))** and developed numerous micro-cracks throughout the surface. The zein_BG coated alloy surface was visualized with thicker surface deposition due to the bioactivity of BG along with the corrosion products of the Mg alloy substrate **Fig. 2.8 ((g1) – (i1))** compared to zein coating **Fig. 2.8 ((d1) – (f1)).** The *in-vitro* observation is indicative of a decreased biodegradability and increased integrity of the zein_BG coated substrate with the host [45,46].

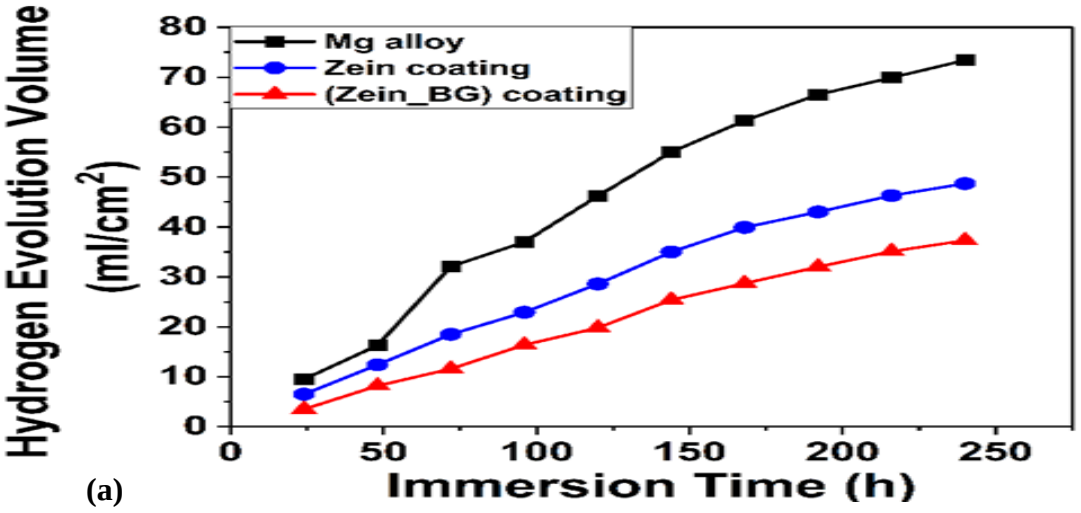

(a)

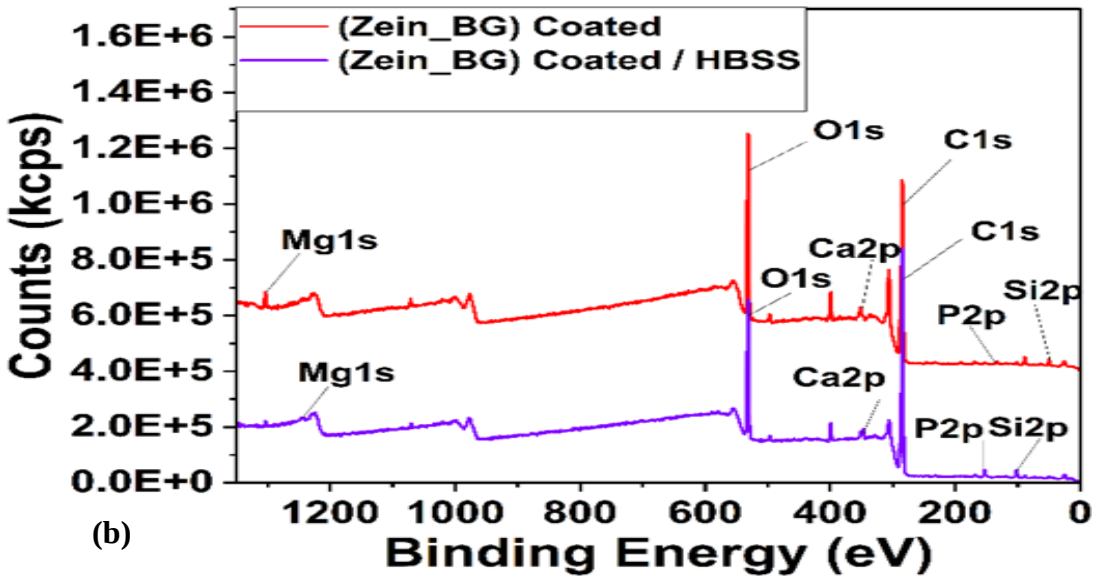

(b)

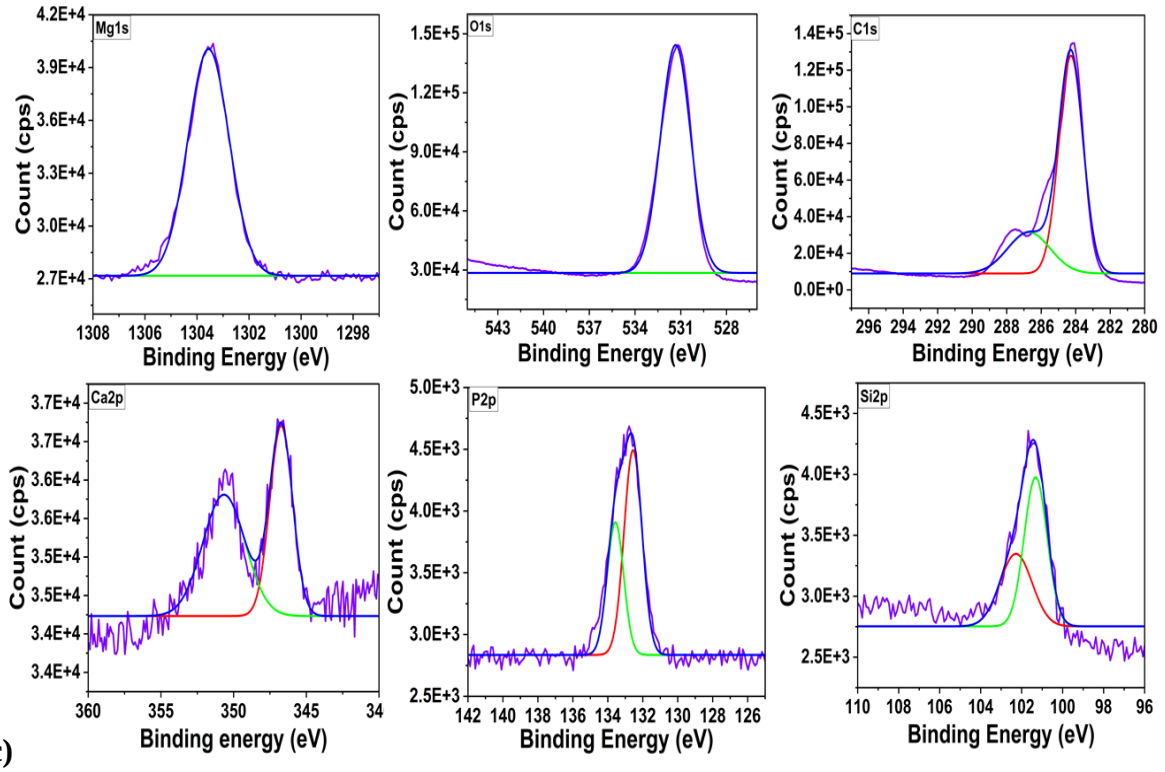
Mg1s
Count (cps)
Binding Energy (eV)
O1s
Count (cps)
Binding Energy (eV)
C1s
Count (cps)
Binding Energy (eV)
Ca2p
Count (cps)
Binding energy (eV)
P2p
Count (cps)
Binding Energy (eV)
Si2p
Count (cps)
Binding Energy (eV)

(c)

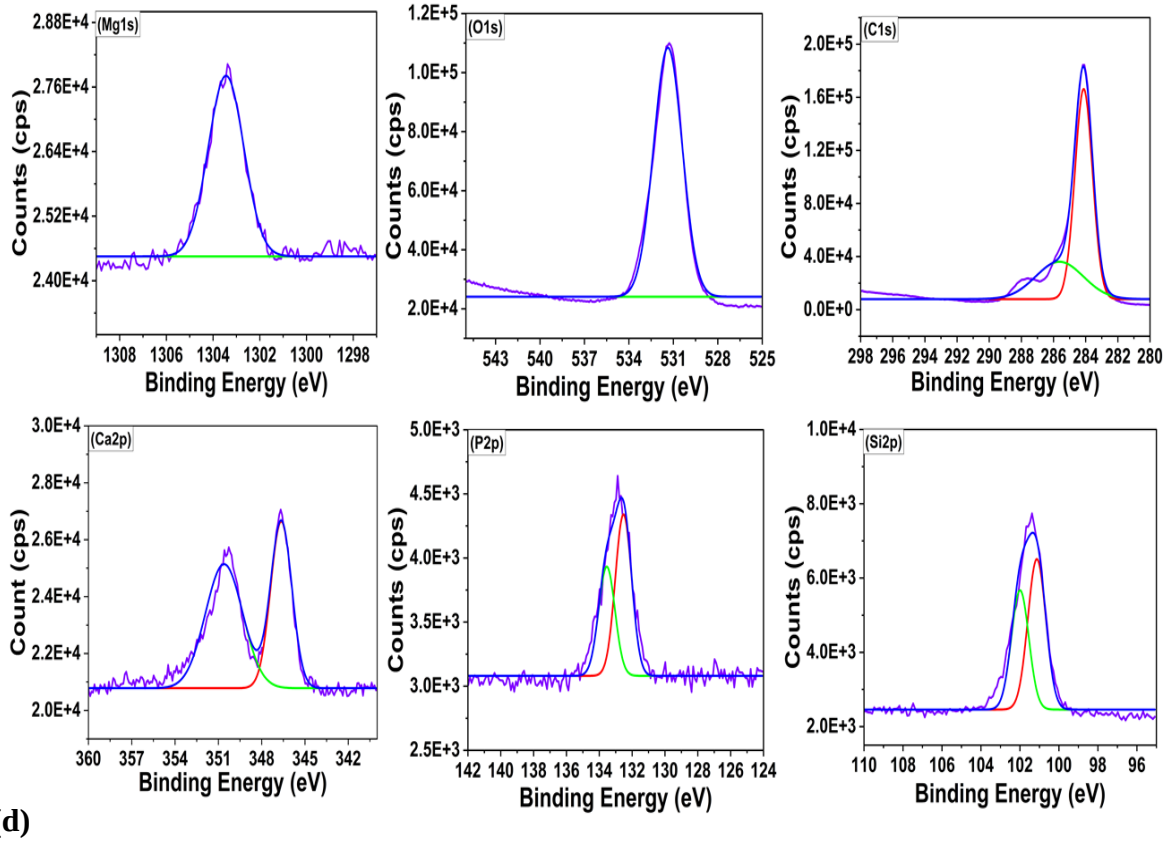
(Mg1s)
Counts (cps)
Binding Energy (eV)
(O1s)
Counts (cps)
Binding Energy (eV)
(C1s)
Counts (cps)
Binding Energy (eV)
(Ca2p)
Count (cps)
Binding Energy (eV)
(P2p)
Counts (cps)
Binding Energy (eV)
(Si2p)
Counts (cps)
Binding Energy (eV)

(d)

(e)

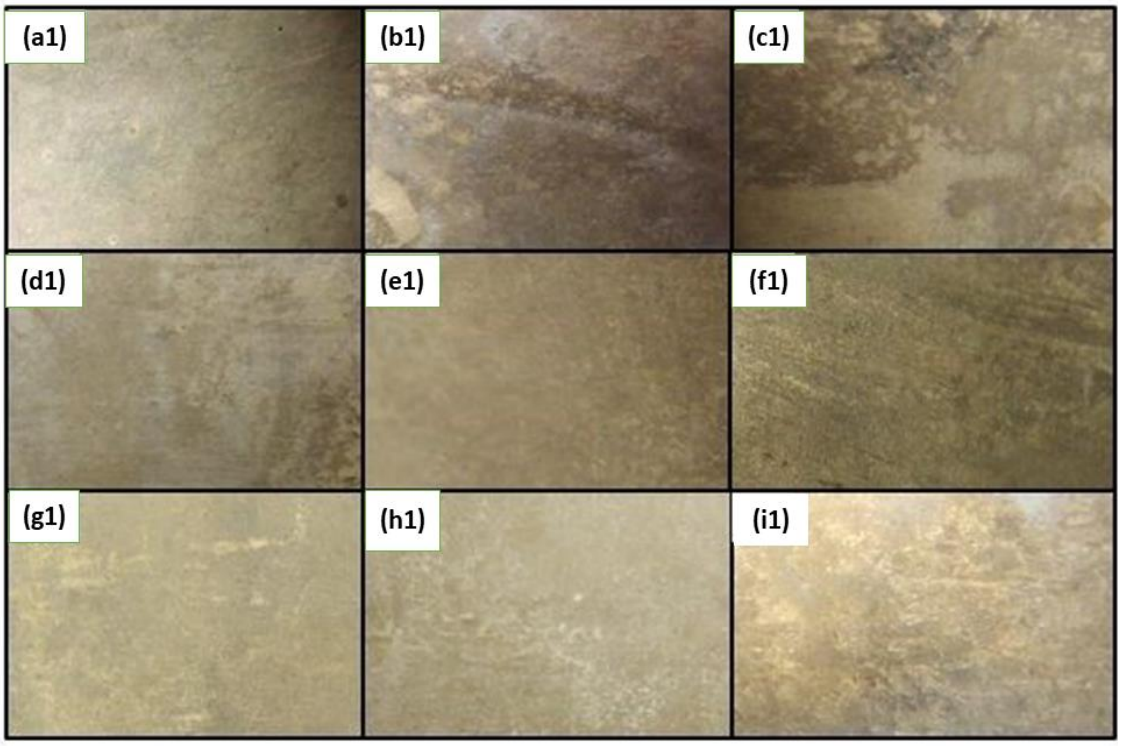

Fig. 2.8: (a) Hydrogen evolution of uncoated and coated Mg alloys as a function of immersion time in HBSS at 37 ℃ for 10 d, **(b)** XPS analysis on zein_BG coated Mg alloy substrate before and after immersion in HBSS at 37 ℃ for 10 d, **(c)** XPS with the high resolution scan region representing Mg1s, O1s, C1s, Ca2p, P2p and Si2p for zein_BG **(d)** XPS with the high resolution scan region representing Mg1s, O1s, C1s, Ca2p, P2p and Si2p for zein_BG in HBSS **(e)** Microscopic images at 1000X magnification of (a1-c1) uncoated **(d1 – f1)** zein coated and **(g1 – i1)** zein_BG coated Mg alloy substrates after 3, 7 and 10 d of immersion in HBSS; respectively.

2.4. Conclusions

In this study, bio-inspired approach was employed to synthesize nano-sized BG with CTAB as template. The resulting BG Nano powder was utilized to make zein_BG composite coating on AZ31B Mg alloy substrate by the dip coating technique. FTIR spectra reported the existence of physical as well as chemical bonding between zein and BG in composite coating. SEM morphology of zein_BG coated alloy surface showed compact and rough microstructure. The coating adhered strongly to the surface of substrate and was

bioactive upon immersion in HBSS. The zein_BG coating demonstrated a suitable water contact angle of 30.36^{o} appropriate for protein attachment. Composite coating presented an appropriate roughness value preferred for cell attachment and proliferation. Interestingly, the excellent corrosion-resistant performance of coating material was demonstrated by EIS. Additionally, in zein_BG coated alloy substrates, the highest corrosion potential was reported for uncoated and zein-coated substrates. The observation indicates that BG nanoparticles in the zein_BG composite could resist the penetration of ions from HBSS due to their bioactive nature. These findings revealed that zein_BG composite coating on the Mg alloy substrate could eliminate dissolution of toxic metallic ions from the substrate in physiological environments. As a result, zein_BG coatings developed via the dip coating technique showed favorable mechanical, biological, and surface characteristics for biomedical purposes and is a potential candidate for *in–vivo* investigations.

References:

[1] A. Cunha, A. Cunha, A. Paula, V. Oliveira, A. Almeida, Wetting behaviour of femtosecond laser textured Ti-6Al-4V surfaces Applied Surface Science Wetting behaviour of femtosecond laser textured Ti – 6Al – 4V surfaces, Appl. Surf. Sci. 265 (2013) 688–696. https://doi.org/10.1016/j.apsusc.2012.11.085.

[2] J. anne N. Oliver, Y. Su, X. Lu, P.H. Kuo, J. Du, D. Zhu, Bioactive glass coatings on metallic implants for biomedical applications, Bioact. Mater. 4 (2019) 261–270. https://doi.org/10.1016/j.bioactmat.2019.09.002.

[3] Z. Zhong, J. Qin, J. Ma, Cellulose acetate/hydroxyapatite/chitosan coatings for improved corrosion resistance and bioactivity, Mater. Sci. Eng. C. 49 (2015) 251–255. https://doi.org/10.1016/j.msec.2015.01.020.

[4] Y. Ahmed, A. Nawaz, R. Singh Virk, A. Wadood, M.A. Ur Rehman, Fabrication and characterization of zein/bioactive glass deposited on pretreated magnesium via electrophoretic deposition, Int. J. Ceram. Eng. Sci. 2 (2020) 254–263. https://doi.org/10.1002/ces2.10066.

[5] M. Mehdipour, A. Afshar, A study of the electrophoretic deposition of bioactive glass-chitosan composite coating, Ceram. Int. 38 (2012) 471–476. https://doi.org/10.1016/j.ceramint.2011.07.029.

[6] H. Moldovan, E. Plopeanu, G. Dan, M. Vasilescu, M. Dobrescu, C. Milea, K. Earar, D. Gheorghita, Contributions on biodegradability of Mg-Ca alloys for orthopedic implants, UPB Sci. Bull. Ser. B Chem. Mater. Sci. 80 (2018) 229–246.

[7] M. Alizadeh-Osgouei, Y. Li, C. Wen, A comprehensive review of biodegradable synthetic polymer-ceramic composites and their manufacture for biomedical applications, Bioact. Mater. 4 (2019) 22–36. https://doi.org/10.1016/j.bioactmat.2018.11.003.

[8] S. Kaya, A.R. Boccaccini, Electrophoretic deposition of zein coatings, J. Coatings Technol. Res. 14 (2017) 683–689. https://doi.org/10.1007/s11998-016-9885-2.

[9] H. Qu, RSC Advances Biomaterials for bone tissue engineering sca ff olds :, (2019) 26252–26262. https://doi.org/10.1039/c9ra05214c.

[10] J. Antonio, E. Pedro, VA. Maria, Tissue engineeing approach based on the use of bioceramics for bone repair. Biomater Sci. 1 (2013) 1–100.

[11] J.R. Jones, Acta Biomaterialia Reprint of : Review of bioactive glass : From Hench to hybrids, Acta Biomater. 23 (2015) S53–S82. https://doi.org/10.1016/j.actbio.2015.07.019.

[12] B.Garrido,V.Albaladejo, I.G.Cano, S. Dosta, Development of Bioglass / PEEK Composite Coating by Cold Gas Spray for Orthopedic Implants, J. Therm. Spray Technol. 31 (2022) 186–196. https://doi.org/10.1007/s11666-021-01312-w.

[13] N. Meyer, L.R. Rivera, T. Ellis, J. Qi, A.R. Boccaccini, Bioactive and antibacterial coatings based on zein / bioactive glass composites by electrophoretic deposition. Coatings. 8 (2018) 1–12 . https://doi.org/10.3390/coatings8010027.

[14] Y. Ahmed, M. Atiq, U. Rehman, Improvement in the surface properties of stainless steel via zein / hydroxyapatite composite coatings for biomedical applications, Surfaces and Interfaces. 20 (2020) 100589. https://doi.org/10.1016/j.surfin.2020.100589.

[15] B. Mavis, A.C. Taş, Dip coating of calcium hydroxyapatite on Ti-6Al-4V substrates, J. Am. Ceram. Soc. 83 (2000) 989–991. https://doi.org/10.1111/j.1151-2916.2000.tb01314.x.

[16] Y. Ahmed, A. Nawaz, M. Atiq, U. Rehman, Fabrication and characterization of zein / bioactive glass deposited on pretreated magnesium via electrophoretic deposition, Inter. J. Ceram. Eng. Sci.,(2020) 254–263. https://doi.org/10.1002/ces2.10066.

[17] Z.M. Al-Rashidy, M.M. Farag, N.A. Abdel Ghany, A.M. Ibrahim, W.I. Abdel-Fattah, Orthopaedic bioactive glass/chitosan composites coated 316L stainless steel by green electrophoretic co-deposition, Surf. Coatings Technol. 334 (2018) 479–490. https://doi.org/10.1016/j.surfcoat.2017.11.052.

[18] L. Besra, M. Liu, A review on fundamentals and applications of electrophoretic deposition (EPD), Prog. Mater. Sci., 52 (2007) 1–61. https://doi.org/10.1016/j.pmatsci.2006.07.001.

[19] D. Santhiya, F. Anjum, glass-ceramic using CT-DNA as a template, J. Mater. Chem. B. 1 (2013) 6329–6338. https://doi.org/10.1039/c3tb21212b.

[20] W. Liu, Z. Yan, X. Ma, T. Geng, H. Wu, Z. Li, Mg-MOF-74/MgF2 composite coating for improving the properties of magnesium alloy implants: Hydrophilicity and corrosion resistance, Materials (Basel). 11 (2018). https://doi.org/10.3390/ma11030396.

[21] H.R. Bakhsheshi-Rad, E. Hamzah, M.R. Abdul-Kadir, S.N. Saud, M. Kasiri-

Asgarani, R. Ebrahimi-Kahrizsangi, The Mechanical Properties and Corrosion Behavior of Double-Layered Nano Hydroxyapatite-Polymer Coating on Mg-Ca Alloy, J. Mater. Eng. Perform. 24 (2015) 4010–4021. https://doi.org/10.1007/s11665-015-1661-4.

[22] N. Gupta, D. Santhiya, A. Aditya, Tailored smart bioactive glass nanoassembly for dual antibiotic: In vitro sustained release against osteomyelitis, J. Mater. Chem. B. 4 (2016) 7605–7619. https://doi.org/10.1039/c6tb01528j.

[23] N. Gupta, D. Santhiya, A. Aditya, K. Badra, RSC Advances, RSC Adv. 5 (2015) 56794–56807. https://doi.org/10.1039/C5RA04441C.

[24] J.J. Schneider, R.C. Hoffmann, J. Engstler, A. Klyszcz, E. Erdem, P. Jakes, R.A. Eichel, L. Pitta-Bauermann, J. Bill, Synthesis, characterization, defect chemistry, and FET properties of microwave-derived nanoscaled zinc oxide, Chem. Mater. 22 (2010) 2203–2212. https://doi.org/10.1021/cm902300q.

[25] D. Santhiya, H.K. Alajangi, F. Anjum, S. Murugavel, M. Ganguli, Bio-inspired synthesis of microporous bioactive glass-ceramic using CT-DNA as a template, J. Mater. Chem. B. 1 (2013) 6329–6338. https://doi.org/10.1039/c3tb21212b.

[26] Q.Z. Chen, I.D. Thompson, A.R. Boccaccini, 45S5 Bioglass®-derived glass-ceramic scaffolds for bone tissue engineering, Biomaterials. 27 (2006) 2414–2425. https://doi.org/10.1016/j.biomaterials.2005.11.025.

[27] S. Naseri, J. Hum, W. Lepry, A. Miri, S. Nazhat, A. Boccaccini, Fabrication and characterization of zein – bioactive glass scaffolds, Bio. Biomim. Nanobiomaterials 4 (2014) 73–78.

[28] A.S. Gnedenkov, S. V. Lamaka, S.L. Sinebryukhov, D. V. Mashtalyar, V.S. Egorkin, I.M. Imshinetskiy, M.L. Zheludkevich, S. V. Gnedenkov, Control of the Mg alloy biodegradation via PEO and polymer-containing coatings, Corros. Sci. 182 (2021) 109254. https://doi.org/10.1016/j.corsci.2021.109254.

[29] S. Prithivirajan, M.B. Nyahale, G.M. Naik, S. Narendranath, A. Prabhu, P.D. Rekha, Bio-corrosion impacts on mechanical integrity of ZM21 Mg for orthopaedic implant application processed by equal channel angular pressing, J. Mater. Sci. Mater. Med. 32 (2021). https://doi.org/10.1007/s10856-021-06535-5.

[30] G. Manivasagam, S. Suwas, Biodegradable Mg and Mg based alloys for biomedical

implants, Mater. Sci. Technol. (United Kingdom). 30 (2014) 515–520. https://doi.org/10.1179/1743284713Y.0000000500.

[31] L. Muthuselvi, A. Dhathathreyan, Contact angle hysteresis of liquid drops as means to measure adhesive energy of zein on solid substrates, Pramana - J. Phys. 66 (2006) 563–574. https://doi.org/10.1007/BF02704499.

[32] P. Xiong, J.L. Yan, P. Wang, Z.J. Jia, W. Zhou, W. Yuan, Y. Li, Y. Liu, Y. Cheng, D. Chen, Y. Zheng, A pH-sensitive self-healing coating for biodegradable magnesium implants, Acta Biomater. 98 (2019) 160–173. https://doi.org/10.1016/j.actbio.2019.04.045.

[33] G. Manivasagam, D. Dhinasekaran, A. Rajamanickam, Biomedical Implants: Corrosion and its Prevention - A Review~!2009-12-22~!2010-01-20~!2010-05-25~!, Recent Patents Corros. Sci. 2 (2010) 40–54.

[34] J. Hum, S. Naseri, A.R. Boccaccini, Bioactive glass combined with zein as composite material for the application in bone tissue engineering, Biomed. Glas. 4 (2018) 72–81. https://doi.org/10.1515/bglass-2018-0007.

[35] M. Kavyani, G.R. Ebrahimi, H.R. Ezatpour, M. Jahazi, Microstructure refinement, mechanical and biocorrosion properties of Mg–Zn–Ca–Mn alloy improved by a new severe plastic deformation process, J. Magnes. Alloy. 10 (2022) 1640–1662. https://doi.org/10.1016/j.jma.2020.11.013.

[36] R. Kumar, P. Katyal, M. Gupta, V. Singh, Electrochemical Corrosion Behaviour Analysis of Mg-Alloys Used for Orthopaedics and Vascular Implants, IOP Conf. Ser. Mater. Sci. Eng. 1225 (2022) 012063. https://doi.org/10.1088/1757-899x/1225/1/012063.

[37] L. Floroian, M. Florescu, F. Sima, G. Popescu-Pelin, C. Ristoscu, I.N. Mihailescu, Synthesis of biomaterial thin films by pulsed laser technologies: Electrochemical evaluation of bioactive glass-based nanocomposite coatings for biomedical applications, Mater. Sci. Eng. C. 32 (2012) 1152–1157. https://doi.org/10.1016/j.msec.2012.03.001.

[38] S. Nezamdoust, D. Seifzadeh, Z. Rajabalizadeh, Application of novel sol–gel composites on magnesium alloy, J. Magnes. Alloy. 7 (2019) 419–432. https://doi.org/10.1016/j.jma.2019.03.004.

[39] M. Atiq, U. Rehman, S. Ammara, Development of sustainable antibacterial coatings based on electrophoretic deposition of multilayers : gentamicin - loaded chitosan / gelatin /

bioactive glass deposition on PEEK / bioactive glass layer, Int. J. Adv. Manuf. Technol. (2022) 3885–3900. https://doi.org/10.1007/s00170-022-09024-3.

[40] S.H. Salleh, S. Thomas, J.A. Yuwono, K. Venkatesan, N. Birbilis, Enhanced hydrogen evolution on Mg (OH)2 covered Mg surfaces, Electrochim. Acta. 161 (2015) 144–152. https://doi.org/10.1016/j.electacta.2015.02.079.

[41] Z. Li, Z. Peng, Y. Qiu, K. Qi, Z. Chen, X. Guo, Study on heat treatment to improve the microstructure and corrosion behavior of ZK60 magnesium alloy, J. Mater. Res. Technol. 9 (2020) 11201–11219. https://doi.org/10.1016/j.jmrt.2020.08.004.

[42] B.R. Barrioni, E. Norris, J.R. Jones, M.D.M. Pereira, The influence of cobalt incorporation and cobalt precursor selection on the structure and bioactivity of sol – gel-derived bioactive glass, J. Sol-Gel Sci. Technol. (2018). https://doi.org/10.1007/s10971-018-4823-7.

[43] B. Di Tie, F. Feyerabend, N. Hort, R. Willumeit, D. Hoeche, XPS Studies of Magnesium Surfaces after Exposure to Dulbecco ' s Modified Eagle Medium , Hank ' s Buffered Salt Solution , and Simulated Body Fluid, Adv. Eng. Mater. (2010) 699–704. https://doi.org/10.1002/adem.201080070.

[44] G. Duan, L. Yang, S. Liao, C. Zhang, X. Lu, Y. Yang, Designing for the chemical conversion coating with high corrosion resistance and low electrical contact resistance on AZ91D magnesium alloy, Corros. Sci. 135 (2018) 197–206. https://doi.org/10.1016/j.corsci.2018.02.051.

[45] L. Ramos Rivera, J. Dippel, A.R. Boccaccini, Formation of Zein/Bioactive Glass Layers Using Electrophoretic Deposition Technique, ECS Trans. 82 (2018) 73–80. https://doi.org/10.1149/08201.0073ecst.

[46] Y. Jin, C. Blawert, H. Yang, B. Wiese, F. Feyerabend, J. Bohlen, D. Mei, M. Deng, M. Silva, N. Scharnagl, K. Strecker, J. Bode, C. Vogt, R. Willumeit-römer, Microstructure-corrosion behaviour relationship of micro-alloyed Mg-0 . 5Zn alloy with the addition of Ca , Sr , Ag , In and Cu, Mater. Des. 195 (2020). https://doi.org/10.1016/j.matdes.2020.108980.

CHAPTER 3

Multifunctional Poly(AllylamineHydrochloride) / Bioactive Glass Layer by Layer surface coating on Magnesium Alloy for biomedical applications

Chapter Three

Multifunctional Poly(Allylamine Hydrochloride) / Bioactive Glass Layer by Layer surface coating on Magnesium Alloy for biomedical applications

3.1. Introduction:

At present, magnesium (Mg) and its alloys are widely regarded as highly appealing materials for the production of orthopedic implants. These Mg-based substrates have properties similar to natural bone in terms of load bearing and elastic modulus [1,2]. Compared to titanium and stainless steel, Mg-based substrates can effectively prevent the need for a second surgery[2]. However, the rate of degradation of Mg-based implants in body fluids is too high to maintain mechanical integrity [3]. One effective way to protect these Mg based implants from deterioration is through surface coating technology. Interestingly, surface coatings not only reduce the erosion rate of Mg composites, but also enhance their biocompatibility by increasing their antibacterial characteristics [4,5]. So far, a complex coating strategy known as layer-by-layer (LbL) assembly has been utilized for fundamentally upgrading the application of Mg composites. LbL assembly is a simple aqueous-based assembling process of various molecules. LbL assembly mostly depends on electrostatic interactions between oppositely charged molecules/particles, making it suitable for depositing sensitive biological molecules on a variety of material surfaces [6–8]. The LbL surface coatings on the implants could also be used for antimicrobial properties, self-healing capabilities, and controlled delivery of various therapeutic targets such as small molecules, supramolecular, biomolecules and nanoparticles [6,9,10].

The current state of the art of LbL coating on Mg alloy substrates is discussed as follows: Fan *et al*. [11] coated a multilayer comprising a cerium-based conversion layer, a graphene oxide layer, and a branched poly(ethylene imine) (PEI)/poly(acrylic acid) (PAA) on the Mg alloy (AZ31). The incorporated graphene oxide acted as a corrosion inhibitor, while the PEI/PAA multilayers provided self-healing ability to LbL coating system. Biodegradable multilayers containing nano-hydroxyapatite particles (nHA) and poly(lactide) nanofibers were coated on the Mg alloy (AM50) surface using a facile single-step air jet spinning approach. The adhesion strength of the LbL coating was greatly improved by the nHA particles and the biodegradation rate of the substrate in Hank's balanced salt solution (HBSS) decreased [12].

Chapter 3: Multifunctional Poly(Allylamine Hydrochloride) / Bioactive Glass Layer by Layer surface coating on Magnesium Alloy for biomedical applications

LbL-assembled layers of anionic and cationic synthetic polymers were used to improve corrosion resistance, cytocompatibility, cellular adhesion, and proliferation on biodegradable Mg alloy [13]. Multilayered polyethyleneimine (PEI)/(polyglycolic acid (PGA)/chitosan (CHI))$_5$ film on the Mg alloy surface exhibited enhanced antibacterial capability [14]. A dip-coated SiO_2/ (polyvinylpyrrolidone (PVP)/PAA)$_5$ soft multilayer on AZ31 Mg alloy was developed as a Mg-based cardiovascular stent with enhanced corrosion resistance [15]. A ((PVP)/(DNA))$_n$ (n= 5, 10, 20 and 40) multilayer film over Mg alloy (AZ31) showed enhanced corrosion resistance, and increased calcium phosphate deposition, creating a biomimetic and biocompatible coating [16]. A superhydrophobic zeolitic imidazolate framework-8 (ZIF-8)/polyvinylidene fluoride (PVDF)/ layered double hydroxide (LDH) coating on Mg alloys, achieved through electrodeposition and dip-coating methods, displayed enhanced anticorrosion properties. The underlying LDH transition layer hindered the passage of corrosive ions, while the top superhydrophobic ZIF-8-based coating reduced the contact area with the corrosive solution [17]. A PVP/ PAA multilayer coating design on the Mg alloy surface improved the homogeneity and binding force of calcium phosphate deposition, providing appropriate corrosion protection [18]. Silver nanoparticles and polymethyltrimethoxysilane were introduced on the Mg alloy (AZ31) surface through LbL assembly and siloxane self-condensation reaction. The resulting composite film exhibited smooth and uniform morphologies, enhancing the corrosion resistance of the substrate through physical barrier and self-healing functionality of polysiloxane [19].

The novelty of the current study resides in the inaugural utilization of therapeutic-loaded bioactive glass (BG) nanoparticles in the process of LbL dip-coating on a magnesium (Mg) substrate. Additionally, biocompatible and biodegradable polymers such as soy protein hydrolysate (SPH) and poly-(allylamine hydrochloride) (PAH) are also used in the LbL coating. The engineered multilayer coating will provide multiple functionalities for the Mg substrate, apart from simple anticorrosion behavior. BG particles are highly biocompatible, and have a higher likelihood of integrating with both hard and soft human tissues [20]. The integration of BG with living tissue makes it the best option for enhancing bioactivity and biocompatibility of metal implants [21,22].

The connection between bone and BG coatings becomes stronger and is comparable to that of bone within 3 to 6 months of implantation. Interestingly, BG coating on metal implants can regulate or inhibit their deterioration in biological environments[20]. For example, electrophoretic deposition of a more adhesive polyvinyl alcohol/natural chitosan/BG composite coating on the surface of 316L stainless steel increased the corrosion resistance of the substrate [23]. A similar composite coating was also reported to improve the biomedical properties of the substrate when applied through electrophoretic deposition on AZ91D Mg alloy [24].The possibility of varying the BG chemical composition by adding secondary elements makes the coatings highly attractive for tunable bioactivity. Although the higher dissolution rate of BG promotes bone growth through the formation of hydroxy apatite (HA), the manufacturing of BG coatings over complicated 3D structures remains complicated. The microstructure, thickness, surface roughness, porosity, and stability directly affect the performance of BG coatings on implants [25].

In this study, the aim was to synthesize a new class of BG nanoparticles by incorporating folic acid (FA) molecules into the BG network through a bio-inspired route. The BG nanoparticles were characterized using FTIR, XRD, TGA, and TEM. The bio-inspired route for BG synthesis is a novel approach developed by Santhiya *et al*, which involves the use of various organic and inorganic templates[26]. This method allows for the synthesis of BG under atmospheric conditions, resulting in exceptional textural properties and good biocompatibility, making it suitable for tissue engineering applications [27]. The layout folic acid, otherwise called folate or nutrient B9, is a fundamental supplement that assumes a pivotal role in the synthesis of DNA, RNA, and proteins, as well as development of platelets and cell division [28]. Importantly, folic acid is also used for cancer prevention [29].

To modify the surface properties of the alkaline treated Mg alloy substrate (AZ31Mg) (AMgS), it was initially coated with soy protein hydrolysate (SPH). This not only changed the positive surface charge of the substrate to negative but also provided a smooth surface coverage. SPH is widely used in in food, nutrition, and health care products [30]. The important biomedical benefits of SPH include anti-inflammatory, antioxidant,

hypocholesterolemia, immunomodulatory, and reduced risk of cancer [30]. The SPH coated Mg alloy substrate was further subjected to multilayer Poly (allylamine hydrochloride) $(PAH/BG)_n$ coatings. Among the various polymers of both natural and synthetic origin, PAH is FDA-approved and frequently employed for surface coating due to its adhesiveness [31]. The degradation products of PAH are metabolically digestible and highly biocompatible. Additionally, the polymer allows for tailorable *in-vivo* degradation rates and hence can be used for drug delivery [31]. Therefore, the multilayer coating of PAH onto the Mg-related alloys, along with adsorption of BG nanoparticles, can provide better corrosion protection and biocompatibility [32]. To combine the benefits of PAH and BG, a novel approach was carried out by LbL dip coating of PAH and BG onto the SPH covered Mg alloy surface. The $SPH/(PAH/BG)_n$ (n= 5 and 7) coated Mg alloy substrates $SPH/(PAH/BG)_n$/AMgS were then analyzed for corrosion properties, mechanical properties, wettability, adhesion strength, and surface roughness . The degradation properties of $SPH/(PAH/BG)_n$/AMgS were also tested for hydrogen evolution in HBSS solution and subjected to FTIR, XRD and X-ray photoelectron spectrometer (XPS) analyses with appropriate control samples. The $SPH/(PAH/BG)_n$/AMgS samples were finally subjected to a hemolysis assay to test their biocompatibility.

3.2. Experimentation

3.2.1. Materials and Methodology

The substrate used for the study was an extruded AZ31 Mg alloy (Al 2.4, Zn 0.5, Mn 0.05, balance Mg (w/w %)). The Mg substrate was supplied by Parshwamani Metals Co., Ltd, India. Soy protein hydrolysate (SPH) (Mw = 670,000) (C.N. S S1674) and PAH (Mw = 58000) (C.N. 71550-12-4) were purchased from Sigma – Aldrich. The synthesis of BG was done using precursors, namely, tetraethyl orthosilicate (TEOS) (C.N. 86578), triethyl phosphate (TEP) (C.N 821141), sodium acetate (NaAC) (C.N. S2889), calcium acetate (CaAC) (C.N. 1086334) and template folic acid (Mw = 441.40) (C.N. F7876) obtained from Sigma –Aldrich. Hanks' balanced salt solution (HBSS) (C.N. H9394), which is otherwise called simulated body fluid (SBF) was purchased from a standard chemical company, Sigma-Aldrich, USA.

The other chemical formulations used in the study were of high purity AR grade. Milli-Q water was used in the experiment. Analysis of Variance (ANOVA) from Origin Lab 2023 was used to forecast errors for each experiment, which was carried out in triplicates.

3.2.2. Alkaline Treatment

Mg substrates were cut into rectangles of size 20 mm × 10 mm ×4 mm and sanded with silicon carbide paper with 2000 grid. The polished substrates were washed with an alcohol solution and deionized water; respectively. The substrates were then gently cleaned with distilled water and dried using warm air, followed by immersion in a1M NaOH solution at 60 ℃ for 20 minutes.

3.2.3. Synthesis of Bioactive Glass

An aqueous solution of 10 mM tris (hydroxymethyl) aminomethane (TRIZMA) buffer, pH 8, was prepared by mixing TRIZMA HCl (61.4 mg/mL) and TRIZMA base (74 mg/mL) in Milli-Q water. Folic acid stock solution (1 mg/mL) was prepared using 100 mL of 10 mM TRIZMA buffer. The BG precursors were added one by one (order of addition: 9.29 g of TEOS, 1.0 g of TEP, 6.36 g of NaAC, 4.21 g of CaAC) slowly and gradually in to 100 mL TRIZMA buffer containing folic acid with 30 min interval for each precursor at 37 ℃. The mixture was left for 24 h in continuous stirring to obtain BG precipitate. It was then centrifuged, washed with 70 % v/v ethanol, dried for three days at 40 ℃ in an oven, and preserved in a desiccator.

3.2.4. Surface Coating

The surface coating process carried out on AMgS is demonstrated in **Scheme (1)**. LBL coatings were formed via a dip coating technique. Layers SPH/$(PAH/BG)_n$ were produced in the following sequence: “ABCBCBCBCBCBCBC”. Negatively charged solutions A and C were 20 g L^{-1} SPH solution at pH 7.10 and 10 g L^{-1} BG at pH 7.34 in distilled water; respectively. Solution B was a cationic aqueous 20 g L^{-1} PAH solution at pH 6.20 in distilled water. The substrate was immersed in solution A for a period of 30 mins, followed by B and C solutions for each 10 mins, n =5 and 7 cycles were performed to attain SPH/$(PAH/BG)_n$ coating on AMgS.

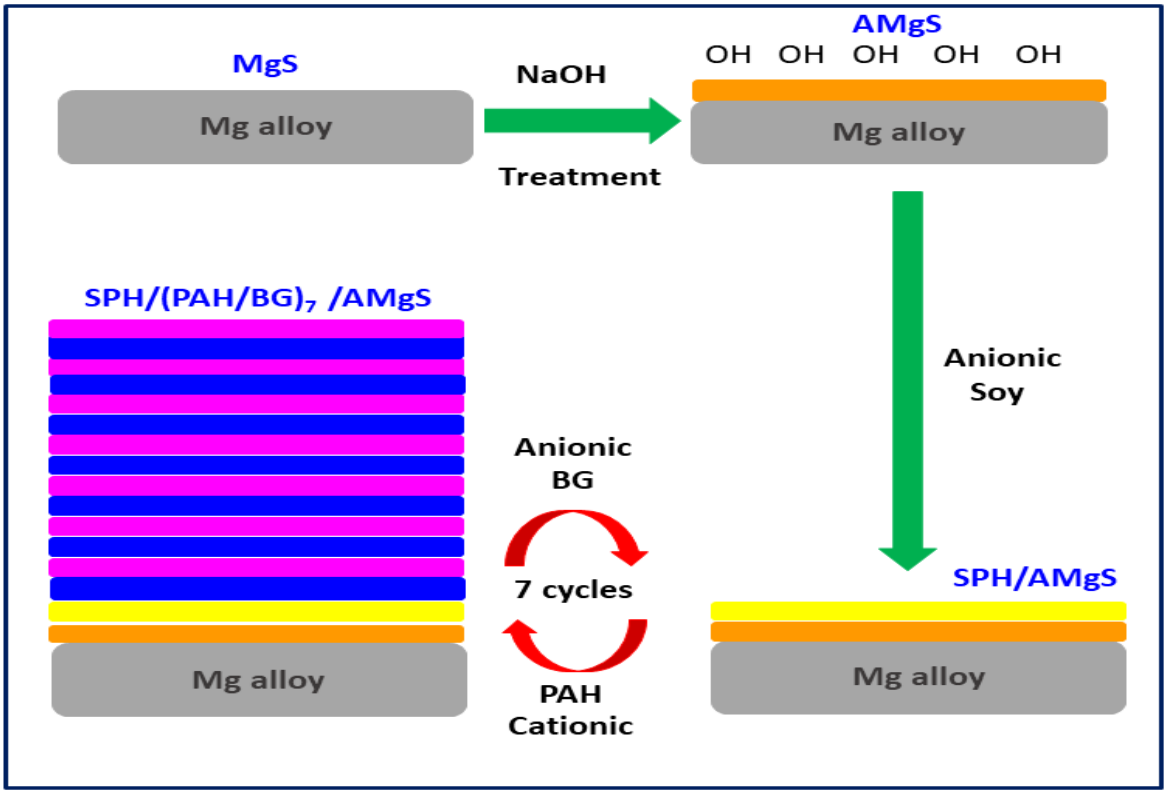

Scheme. 1: Schematic representation of the preparation of SPH/(PAH/BG)$_7$ coating on AMgS.

3.2.5. Characterization

3.2.5.1. Morphological Analysis

Transmission electron microscopy (CM200 - FEG - Philips) was used to record the morphology of BG nanoparticles at the required magnification. The average BG particle size was estimated using the ImageJ program included with 64-bit Java 1.8.0_172.

SPH/(PAH/BG)$_n$/AMgS was exposed to field emission scanning electron microscopy (FE-SEM, Nova Nano SEM 450, USA) at 500 X, 2.5 KX, 50 KX and 150 KX magnifications and an accelerating voltage of 20.0 kV to record the morphology of the surface coating. The uncoated, alkaline treated and after each layer of SPH/(PAH/BG)$_n$ coating (Section 3.2.4), Mg alloy samples were visualized through optical microscopy at a magnification of 1000 X. Similarly, coated Mg alloy surfaces were also examined using optical microscopy after immersion in HBSS.

3.2.5.2. Energy Dispersive Spectroscopy (EDS)

Energy dispersive spectroscopy with the X Flash 6|60 detector component of the Quanta 650 (FEI) was used to estimate the chemical constituents of SPH/$(PAH/BG)_n$ coatings on AMgS.

3.2.5.3. Fourier Transform Infrared Spectroscopy:

FTIR spectra of native FA, BG, as well as SPH/$(PAH/BG)_n$/AMgS, were recorded using a NICOLET 380 FTIR spectroscopy with a resolution of 1 cm^{-1}. The FTIR spectroscopy was used to record spectra in the range of in 4000 cm^{-1} to 400 cm^{-1}.

3.2.5.4. Thermogravimetric Analysis (TGA):

The thermal stability of native FA and BG was investigated using a thermogravimetric analyzer (SDT, Q600, TA instrument). The samples were warmed from room temperature to 800 ℃ at warming temperature of 5 ℃/min beneath nitrogen surroundings, preserving a nitrogen circulation pace of 50 mL/min.

3.2.5.5. X-ray Diffraction (XRD) Analysis:

Native BG as well as SPH/ $(PAH/BG)_n$/AMgS, were subjected to XRD analyses using a BRUKER D4 X-ray diffractometer. The instrument operated at 30 kV, 15 mA with Cu- Kα radiation. For the investigation, a 2θ range of 10°- 80° with a 0.01 step size and 6s per step count time was maintained.

3.2.5.6. Measurement of Contact Angle

Water drops contact angle (20 µL of deionized water) on the uncoated MgS, AMgS, SPH/AMgS and SPH/$(PAH/BG)_n$ / AMgS was measured using a DSA25 drop shape analyser, Kruss Scientific, India. For the measurement, a sessile drop was photographed at points of junction between the drop contour and surface projection (baseline).

3.2.5.7. Surface Roughness Test

The surface roughness of uncoated MgS, AMgS, SPH/AMgS and SPH/$(PAH/BG)_n$ / AMgS was tested using a TR-100 (Testlab) surface roughness tester following ASTM (D3359-B) protocol. For the adhesion test; a perpendicular lattice pattern showing 12 cuts in every path was formed on the alloy sample surface. A prescribed pressure-sensitive tape was overlaid over the substrate surface, followed by its elimination. The film adhesion was then evaluated by comparison with a 0 to 5 scale standard descriptions.

3.2.5.8. X-ray Photoelectron Spectrometer (XPS)

The elemental composition of SPH/$(PAH/BG)_7$ coatings on AMgS was investigated by XPS before and after immersion with HBSS for 10 d at 37 ℃. The analyses were performed using the VGESCALAB II system with AlKα radiation of energy1486.6 eV. Binding energies were estimated with reference to the C1s line at 285.0 eV.

3.2.5.9. Corrosion Characterization

The corrosion behavior of the uncoated and SPH/$(PAH/BG)_n$/AMgS was assessed by the weight loss method. The experiments were conducted after immersing in HBSS at pH 7.4 for 3, 7 and 10 d at 37 ℃ ; respectively. The clean alloy samples were weighed before and after immersing in HBSS as per ASTM G61 – 86 protocols. The corrosion rate (CR) and protection efficiency (PE %) of the alloy samples were calculated by using EQs. (1) and (2) as given below [33] :

$$\text{CR}\ (\text{mg}/cm^2.\text{d}) = \frac{(\text{w2}-\text{w1})}{\text{A t}} \quad (3.1)$$

$$\text{PE}\ \% = \frac{(CR\ uncoated - CR\ coated)}{CR\ uncoated} \times 100 \quad (3.2)$$

Where w_1 and w_2 are the weight of samples before and after immersion respectively.
A is the area of the sample (cm^2) and t is the time (h).

A three-electrode cell set-up was used in an electrochemical analyzer (PAR Model 2273, Princeton, USA) to obtain a potentiodynamic polarization curve and electrochemical impedance spectra (EIS) in HBSS. The coated and uncoated substrates with an exposed area of 1.0 cm^2 were working electrodes, a saturated calomel electrode (SEC), and a platinum

sheet were used as control and counter electrodes respectively. The polarization was applied from -2.0 V to -1.0 V at a scan rate of 1 mV/s. The corrosion potential (E_{corr}, V), corrosion current density (I_{corr}, A/cm^2), and Tafel slopes (β_a & β_c) (V dec^{-1}) data were fitted using the Tafel extrapolation method. EIS was recorded at open circuit potential at a 10-mV sinusoidal amplitude over a frequency range of 100 kHz to 0.01 Hz. The obtained EIS Nyquist plots were analyzed using ZSimp Win software (version 3.1 USA) and were best fitted to the appropriate equivalent circuit model. A stable open circuit was established within 1 h before the EIS testing [15]. The polarization resistance (R_p,V) and corrosion protection efficiency (% IE) were calculated using Eq.(3) [34]:

$$R_p = \frac{\beta_a \beta_c}{2.303\, I_{corr}\, \beta_a \beta_c} \quad (3.3)$$

Where, β_a and β_c demonstrate anodic and cathodic slopes (V dec^{-1}).

3.2.5.10. Hydrogen Evolution Test

The uncoated and SPH/(PAH/BG)n/AMgS in HBSS at 37 °C were placed in an inverted funnel linked to a graduated burette for hydrogen evolution. The water level in the burette was recorded occasionally for 240 hours by full surface exposure. The substrates were arranged to evaluate the evolution of modest hydrogen from samples [35].

3.2.5.11. In-Vitro Hemocompatibility Test

To evaluate the blood compatibility of native Mg alloy, AMgS, SPH/(PAH/BG)$_5$/AMgS, and SPH/(PAH/BG)$_7$/AMgS, a hemolysis test was conducted according to ISO 10993-4:2002 standards[36]. Healthy blood was obtained from adult volunteers and collected in heparinized tubes.

Preparation of phosphate buffered saline (PBS): Samples with dimensions of 20 mm×10 mm×4 mm, according to ISO 10993-4:2002 standards, were dipped in a centrifuge tube containing 10 mL of PBS. The sample surface area to PBS volume ratio was 3:1 cm^2 mL^{-1}. All the centrifuge tubes were maintained in a shaking bath at 37℃ for half an hour. Then, 0.2 mL of diluted blood (2 mL whole blood diluted by 2.5 mL of PBS) was added to the tubes, and the mixtures were incubated for one hour at 37℃ . 10 mL of PBS was used

as a negative control, and 10 mL of distilled water was used as a positive control. The tubes were centrifuged for 15 min at 15000 rpm, and the supernatant was removed and transferred to cuvettes for spectroscopic analysis (UNIC – 7200, CHINA) at a wavelength of 545 nm.

The hemolysis ratio (HR) was calculated according to the following equation[37] :

$$HR(\%) = \left[\frac{D_{test} - D_{negative}}{D_{positive} - D_{negative}}\right] \times 100 \quad (3.4)$$

Where, D_{test} is the absorbance of the testing sample, and $D_{positive}$ and $D_{negative}$ are the absorbance of the positive control (10 mL of distilled water with 0.2 mL of diluted blood) and the negative control (10 mL of PBS with 0.2 mL of diluted blood); respectively.

3.3. Result and Discussion

3.3.1. BG particle characterization

Fig. 3.1 (a) provides a TEM micrograph of BG nanoparticles. The TEM results revealed that BG nanoparticles were more or less spherical in shape with aggregated morphology. The ImageJ analysis software of micrographs revealed an average particle size of 12.53 ±2.22 nm **(Fig. 3.1(b)).**

The FTIR spectrum of native **FA Fig. 3.2(a)** showed a characteristic peak positioned at 1609 cm^{-1} because of −C=O stretching (amide I), α-carboxyl vibrations of amide linkage (−CONH) and N−H (amide II) bending of FA **(Fig. 3.2(c))** also seen at 1507 cm^{-1} as an overlap. The expected carboxyl (C—O stretching, ≈1564 cm^{-1}) was not seen and must be overlapped in the region from 1609 cm^{-1} to 1507 cm^{-1}. A sharp peak at 1415 cm^{-1} indicates the existence of the phenyl ring of FA [3]. The peaks 3542 cm^{-1}, 3418 cm^{-1} and 3322 cm^{-1} appeared in the wavenumber range from 3500 cm^{-1} to 3000 cm^{-1} due to O-H and N−H stretchings of FA [38]. The FTIR spectrum of **BG** showed peaks at 1091 cm^{-1} (broad), 802 cm^{-1}, and 474 cm^{-1}, which attributed to asymmetric stretching, symmetric stretching and symmetrical bending vibrations of the Si −O−Si bond [39]. The amide I vibration of FA was seen as a small shoulder at 1616 cm^{-1} in the case of BG. A sharp peak at 1572 cm^{-1} is due to C— O stretching,which might have originated from template FA. A broad band centered around 3452 cm^{-1} due to N−H/ O-H stretching showed a shift towards higher

wavenumber in comparison with free FA. Interestingly, the peak corresponding to the phenyl ring of FA was seen at 1425 cm^{-1} in the FTIR spectrum of BG. The existence of the characteristic peak of FA in BG confirms the presence of FA as template molecules in the BG network. The reported higher wavenumber shift (3418 cm^{-1} to 3452 cm^{-1}) of N−H / O-H stretching, amide I (from 1609 cm^{-1} to 1616 cm^{-1}) vibrations along with the phenyl ring (1415 cm^{-1} to 1425 cm^{-1}) of template FA peaks in the BG sample compared to native FA confirm the physical and chemical interaction of FA molecules with BG network through groups N−H, O-H, −C=O, and the phenyl ring. The results presented are in line with our previous findings[40].

The XRD pattern of **BG (Fig. 3.2(b))** was dispersive and showed a broad diffracting domain in the 2θ range of 10^{o} to 40^{o}. The observation revealed an amorphous structural characteristic of BG [41].

The TGA for **FA (Fig. 3.2(d))** showed that the initial weight loss of 2.5 w/w % at 142 ℃ was due to the removal of water molecules. Thereafter, 54.2 w/w % of the sample remained at 415 ℃ and 88.3 w/w % degraded at 616℃ [42]. For **BG**, the initial weight loss of 15 w/w % occurred at a temperature of 71 ℃ due to water absorbed. Further, the weight loss increased slightly from 15 w/w % to 28.4 w/w % at 346 ℃ and then increased steeply to 52.3 w/w % at 440 ℃. The observed BG weight loss at 440 ℃ is more or less in good agreement with the weight loss of native FA at 415 ℃ , indicating the loss of the remnant folic acid template molecules. The reported increase in temperature (25℃) for FA degradation in BG indicates the interaction of template molecules with the BG network and supports the FTIR finding (Fig. 2(a)). Thereafter, up to 900 ℃, around 46.9 w/w % of BG remained [43]. These findings evidence the existence of FA in the BG network and are in good agreement with our earlier reports [39].

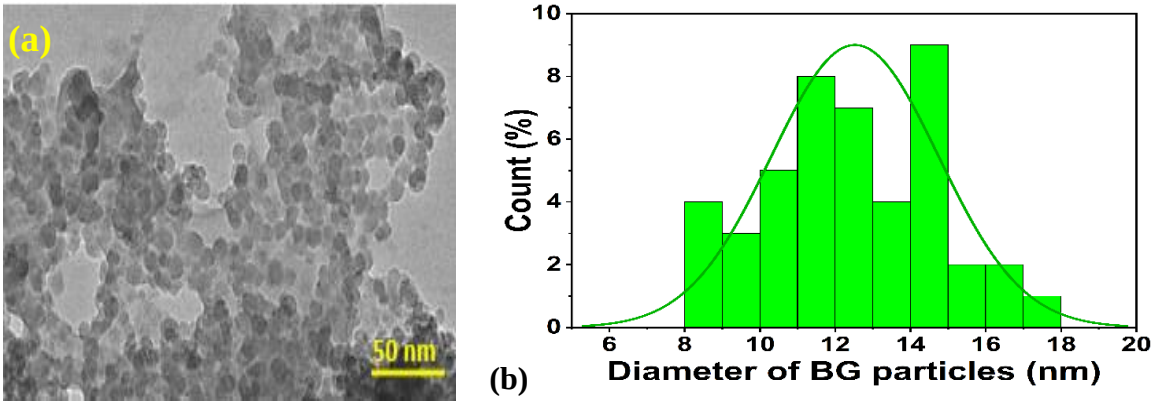

Fig. 3.1: (a) TEM micrograph of BG particles and **(b)** Average particle diameter of BG that is evaluated by ImageJ analysis software (included with 64-bit Java 1.8.0 _ 172) along with descriptive statistics using TEM micrograph.

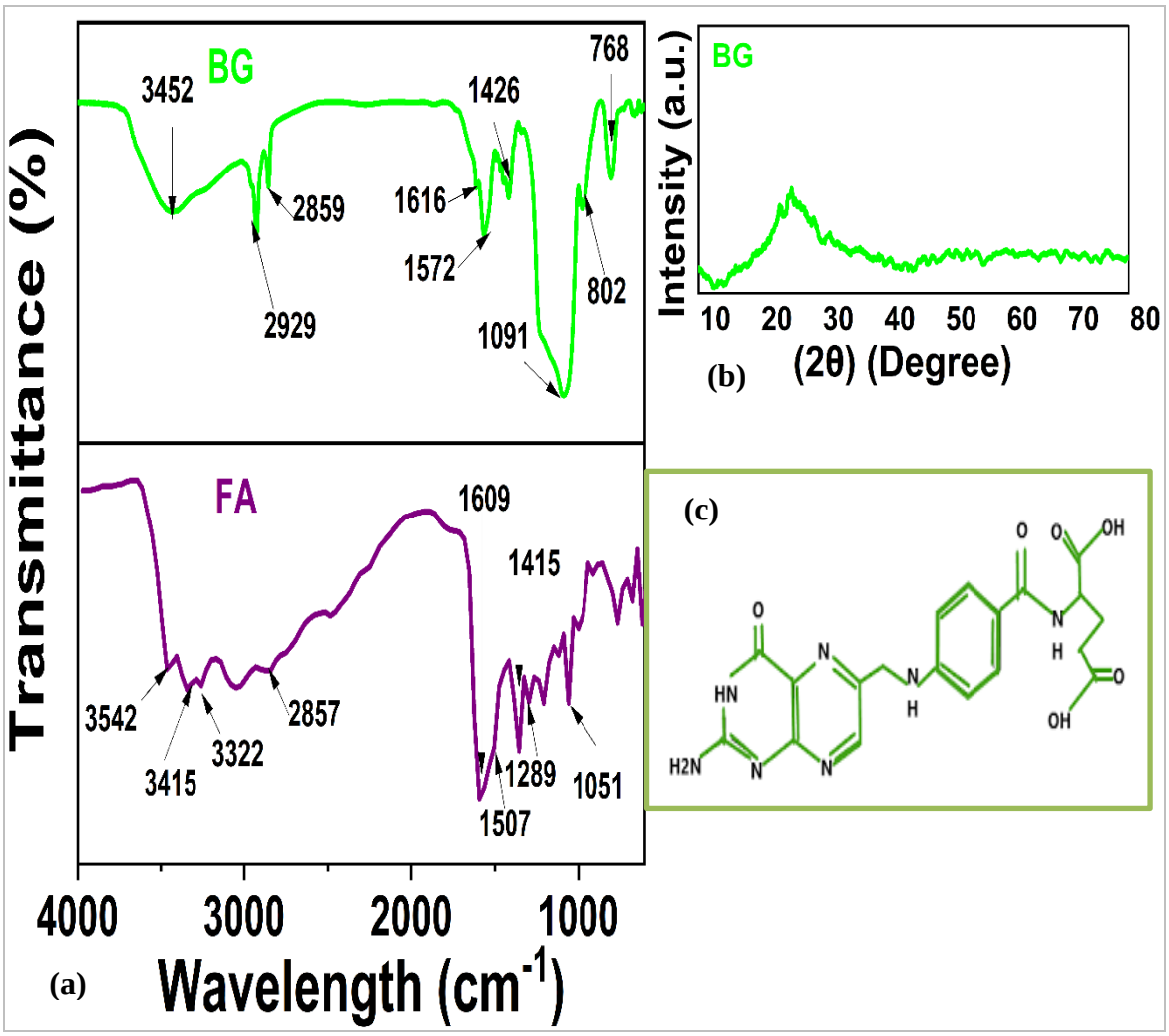

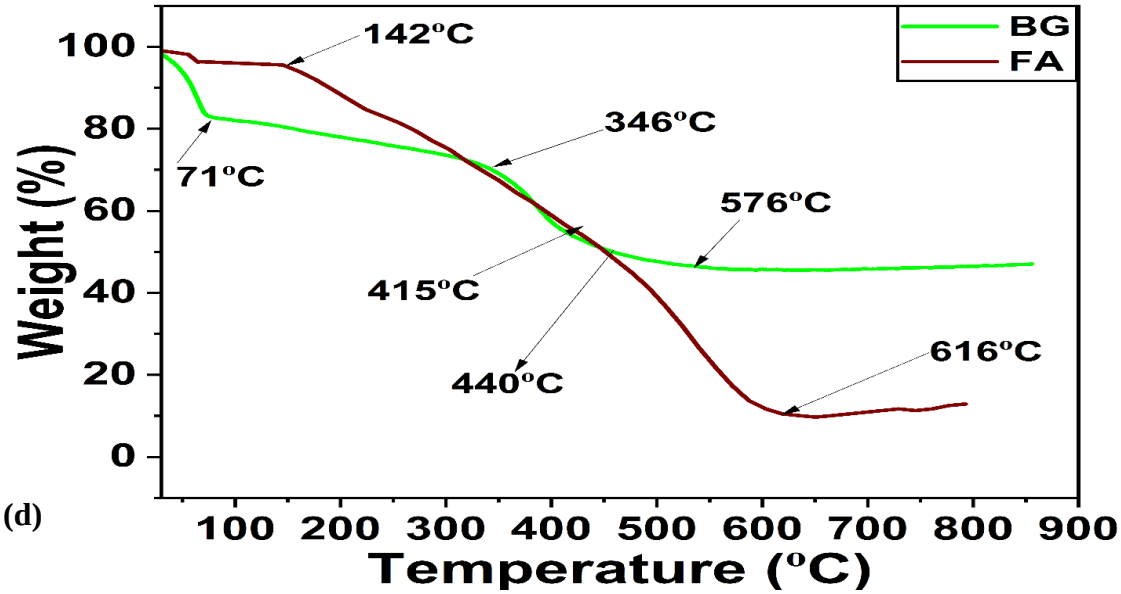

Fig. 3.2: (a) FTIR spectra **(d)** TGA of native FA and FA templated BG nanoparticles, **(b)** XRD pattern of FA templated BG and **(c)** Chemical structure of FA.

3.3.2. Characterization of Coated Mg Alloy Surface

3.3.2.1. Microstructure of Mg alloy subsequent to alkaline pre-treatment

Figs. 3.3((a)-(e)) provides microscope images of the bare, alkaline-treated, and SPH-coated AMgS, PAH/AMgS, and BG/AMgS for one cycle at 1000 X magnification. The microscopic image of the bare alloy surface exhibited grinding residues, which were recognized through long grooves. In contrast, the microscopic image of the 1M NaOH-treated MgS (AMgS) **(Fig. 3.3(b))** portrayed a white-colored coverage instead of long grooves on the bare substrate. These observations might indicate the hydroxylation of the Mg surface due to the alkaline treatment[8]. Interestingly, the SPH coated AMgS was visualized as the smoothest among all substrates with uniform coverage **(Fig. 3.3(c)).** The difference in the optical visualization of various stages of coatings (Native Mg alloy, AMgS, SPH/AMgS, SPH/PAH/AMgS, and SPH/PAH/BG/AMgS) from **Fig. 3.3(a)** to **Fig.3.3(e)** confirmed surface changes on the substrate.

3.3.2.2. Characterizations of SPH(PAH/BG)$_n$/AMgS Coatings

Fig. 3.4 shows the FESEM micrographs of SPH/(PAH/BG)$_5$ and SPH/(PAH/BG)$_7$ LBL coatings on AMgS at different magnifications (500X, 2.5KX, 50KX and 150KX) with

an accelerating voltage of 20.0 kV. The micrographs reveal the presence of BG particles on the surface of the coated Mg substrate **Figs. 3.4 (a - d). Figs. 3.4 (e - h)** demonstrate that SPH/$(PAH/BG)_5$/AMgS has a rough and uneven morphology with shallow scratches compared to SPH/$(PAH/BG)_7$/AMgS. The SPH/$(PAH/BG)_7$ coating completely covered the AMgS surface, unlike SPH/$(PAH/BG)_5$. Cross-sectional images of SPH/$(PAH/BG)_5$/AMgS and SPH/$(PAH/BG)_7$/AMgS are presented in **Figs. 3.4(i)** and **3.4(j);** respectively. The reported thickness of SPH/$(PAH/BG)_5$ and SPH/$(PAH/BG)_7$ coatings on AMgS is 28.15 ± 0.1 µm and 31.06 ± 0.1 µm; respectively. Among these two LBL coatings, the SPH/$(PAH/BG)_7$ /AMgS coating exhibits the most compact microstructure with a homogeneous morphology.

Figs. 3.4 (k - n) show the EDS mapping and spectra for SPH/$(PAH/BG)_n$/AMgS. EDS mapping on the SPH/$(PAH/BG)_n$/AMgS coated alloy surface revealed the presence of elements such as Si, Ca, Na, P, Mg, and O [18]. These findings suggest that BG and PAH are present on the coated alloy surface. Importantly, the highest coverage of Si, Ca, Na, P, and O elements was observed on SPH/$(PAH/BG)_7$/AMgS compared to SPH/$(PAH/BG)_5$/AMgS, while the amount of Mg decreased. These observations indicate a denser coverage of BG particles on AMgS with the 7-layer coating compared to the 5-layer coating.

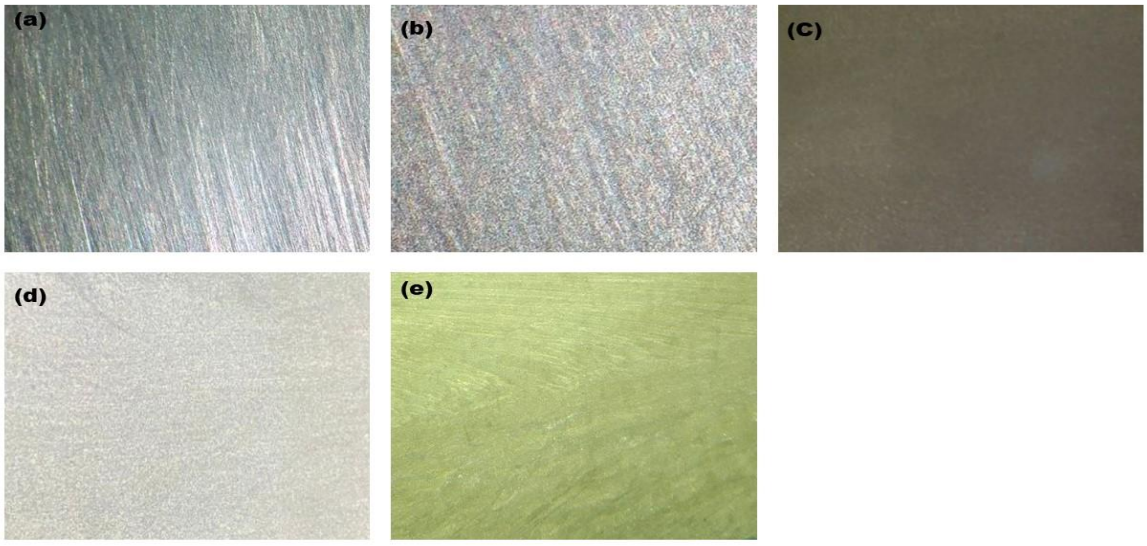

Fig. 3.3: Optical microscopic images of **(a)** MgS **(b)** AMgS and (c) SPH/AMgS, **(d)** SPH/PAH/AMgS, and **(e)** SPH/PAH/BG/AMgS for one coating cycle at 1000 X magnification.

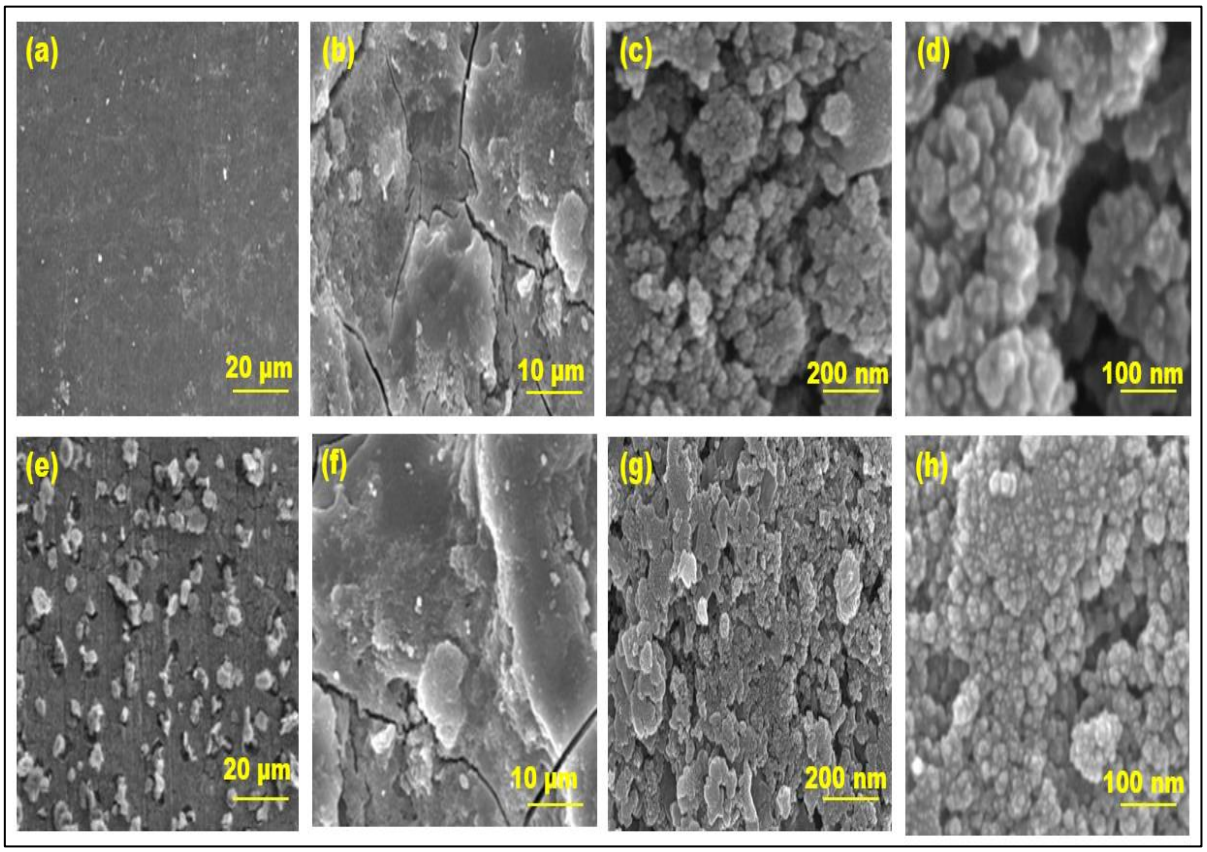
(a)
20 µm
(b)
10 µm
(c)
200 nm
(d)
100 nm
(e)
20 µm
(f)
10 µm
(g)
200 nm
(h)
100 nm

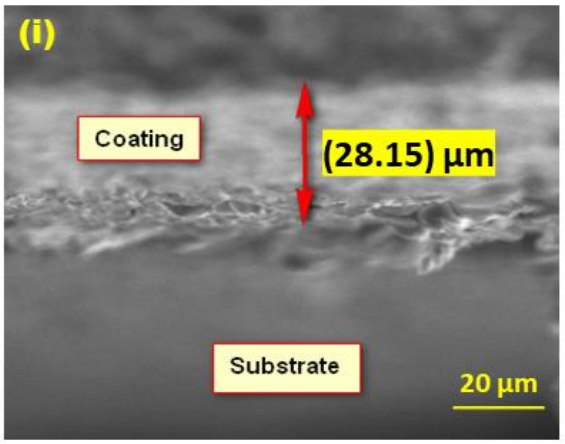
(i)
Coating
(28.15) µm
Substrate
20 µm

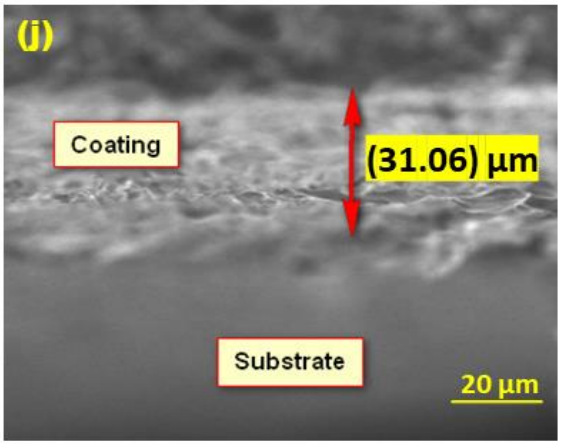
(j)
Coating
(31.06) µm
Substrate
20 µm

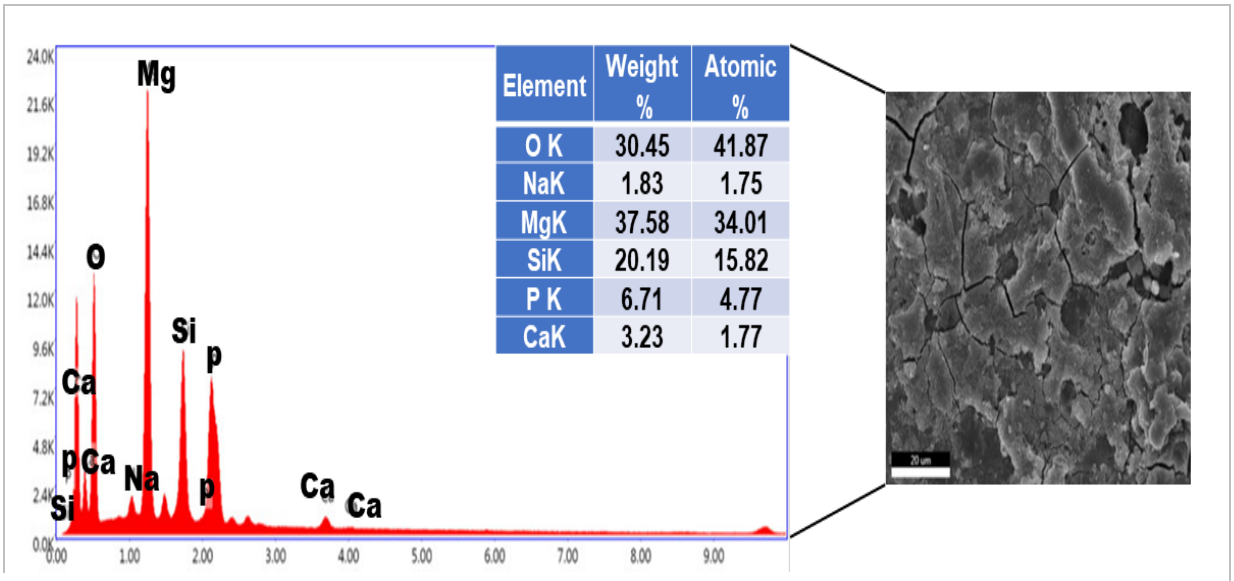
Mg
O
Si
p
Ca
p Ca
Na
p
Ca
Ca
Si
Element | Weight % | Atomic %
O K | 30.45 | 41.87
NaK | 1.83 | 1.75
MgK | 37.58 | 34.01
SiK | 20.19 | 15.82
P K | 6.71 | 4.77
CaK | 3.23 | 1.77

(k)

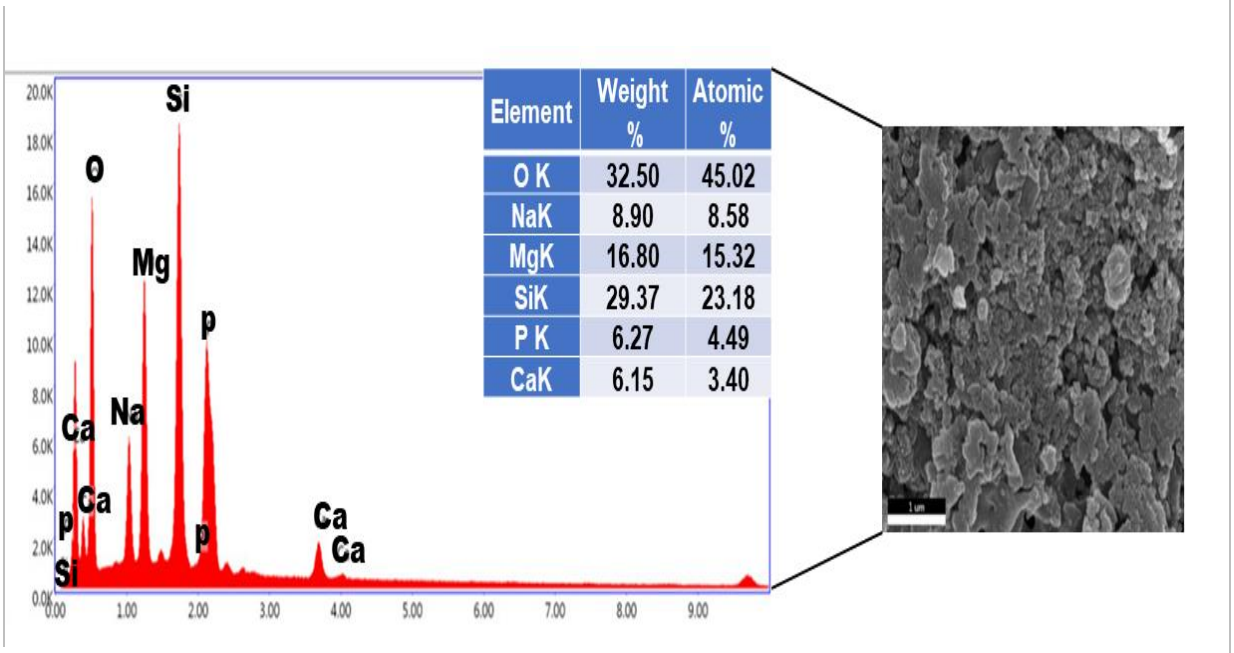
Si
O
Mg
p
Ca
Na
Ca
p
p
Ca
Ca
Si
Element | Weight % | Atomic %
O K | 32.50 | 45.02
NaK | 8.90 | 8.58
MgK | 16.80 | 15.32
SiK | 29.37 | 23.18
P K | 6.27 | 4.49
CaK | 6.15 | 3.40

(l)

(m)

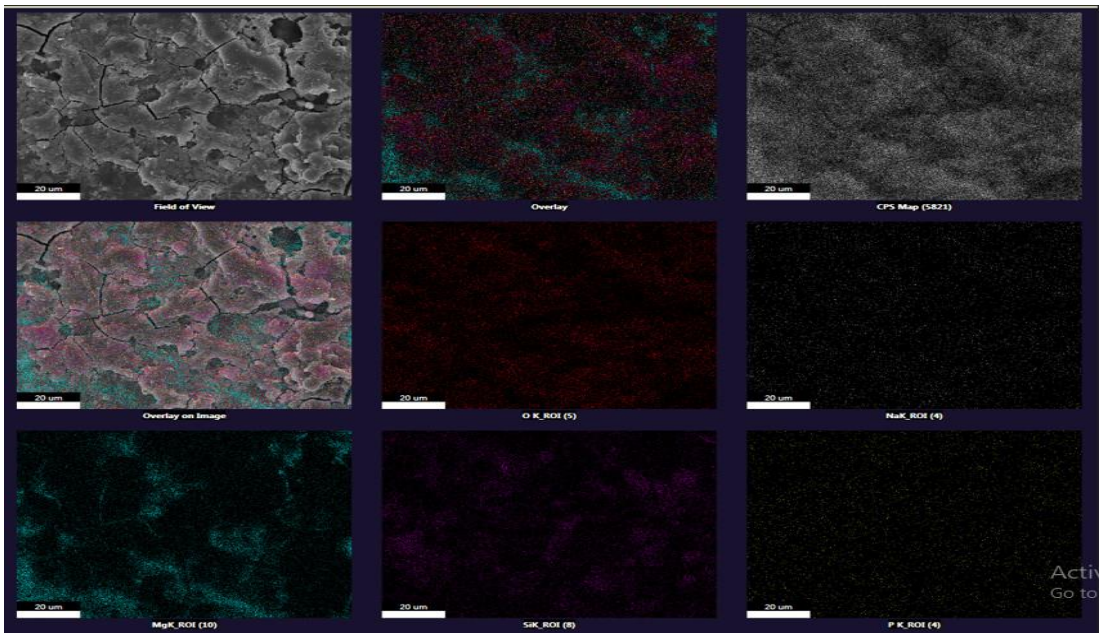

(n)

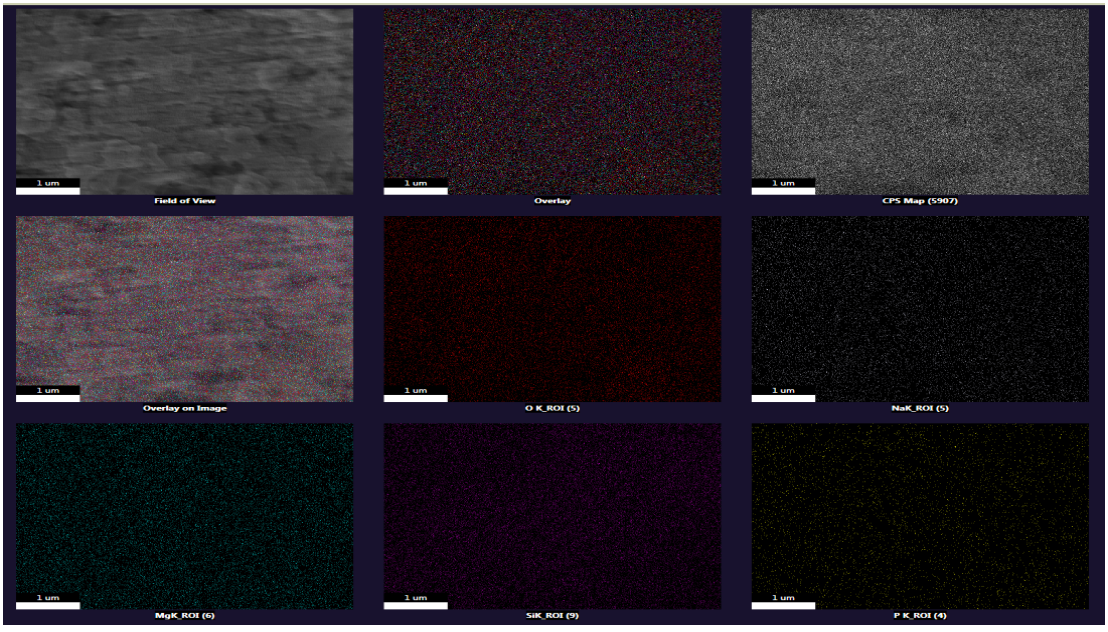

Fig. 3.4: (a), 4(b), 4(c), 4(d), 4(e), 4(f), 4(g) and **4(h)** FESEM micrographs at 500 X, 2.5K X, 50K X and 150K X magnifications; respectively**, 4(i)** and **4(j)** cross – sectional view at 500 X magnification of SPH/$(PAH/BG)_5$ and SPH/$(PAH/BG)_7$; respectively. **4(k), 4(l), 4(m)** and **4(n)** represent EDS analyses and map on SPH/$(PAH/BG)_5$/AMgS and SPH/$(PAH/BG)_7$/AMgS; respectively.

3.3.2.3. Surface Wettability and Roughness

Fig.3.5 (a) portrays water contact angle data on uncoated and coated Mg alloy surfaces. The reported water contact angle (84.02° ± 4.2°) on the bare Mg alloy substrate reveals its hydrophobic nature. The contact angle values of the Mg substrate decrease after alkaline treatment (72.63° ± 3.63°) and subsequent SPH coating (68.89° ± 3.44°). For five- and seven-layer coatings of SPH/$(PAH/BG)_n$, contact angle values were $66.67^{o} \pm 5.53^{o}$ and $61.85^{o} \pm 6.21^{o}$, respectively. Interestingly, both of these contact angles are in close proximity to the ideal range of wettability (35^{o}- 80^{o}) that is suitable for the initial protein attachment before cell growth [44]. These observations indicate an improvement in the AMgS wettability after SPH/$(PAH/BG)_n$ coating. In the multilayer coating of SPH$(PAH/BG)_n$, when n = 5 or 7 the last layer ends with BG, which has a net negative charge and is hence hydrophilic due to the existence of Si-O-Si and hydroxyl groups in the BG structure [45]. The incorporation of BG containing -OH,−CONH, C—O, and N-H groups (Fig. 2(a)) in the inner layers further enhances the hydrophilic nature of surface PAH layer, thus integrating both to form a hydrophilic nature of the multilayer coating [46].

Aside from wettability, surface topography plays a significant role in defining the responsiveness of coated AMgS to cellular contact. Various reports have recommended that the surface roughness, wettability, and chemistry should be fundamentally examined to design a good surface for the attachment of proteins as well as the adhesion of cells [47]. The average surface roughness of several coatings was used to assess the surface topography on the Mg substrate and is displayed in **Fig. 3.5(b).** SPH$(PAH/BG)_5$/AMgS and SPH/$(PAH/BG)_7$/AMgS showed surface roughness values Ra = 2.33 ± 0.03 and Ra = 2.95 ± 0.04; respectively. The observed roughness values of the multilayers displayed significant surface roughness in contrast to the bare substrate (Ra = 0.16 ± 0.03). The mean roughness of the SPH/$(PAH/BG)_n$ coating was in the range that is appropriate for the attachment and expansion of osteoblast-like cells and bone marrow derived ST-2 cells [46].

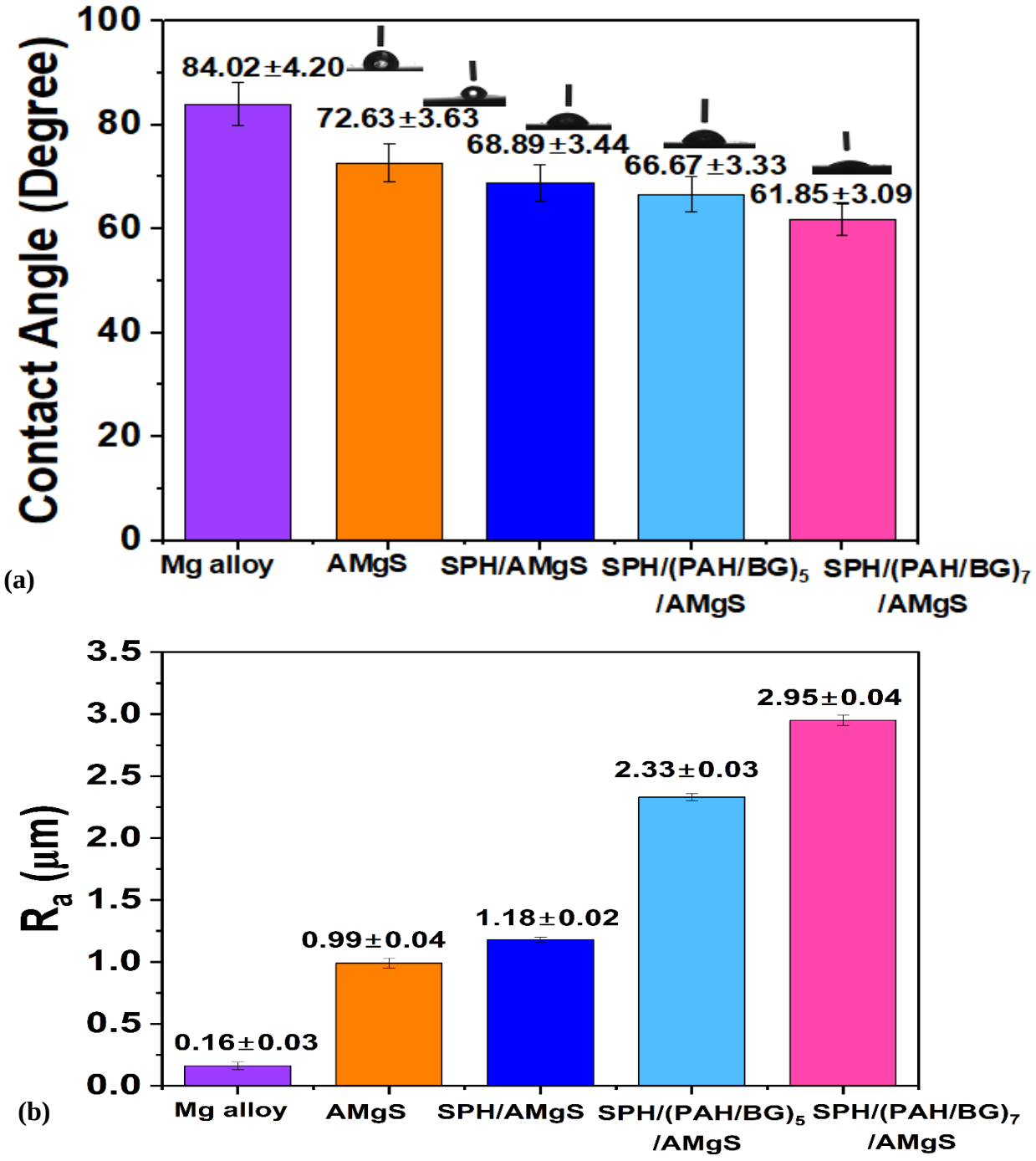

Fig. 3.5: (a) Water contact angle and **(b)** surface roughness measurements of MgS, AMgS, SPH/AMgS, SPH/$(PAH/BG)_5$/AMgS and SPH/$(PAH/BG)_7$/AMgS ; respectively.

3.3.3. Adhesion Test

The essential qualities of coating materials are their mechanical integrity with the substrate and long - term durability. These properties of the coating materials depend on their adherence on the substrate surface. The adherence of SPH(PAH/BG)$_n$ coatings on AMgS was evaluated as per ASTM (D 3359–B) [48]. A tape adhesion test was performed on SPH/(PAH/BG)$_n$/AMgS and viewed under an optical microscope after removing the tape **(Figs. 3.6(a) and (b)).** SPH/(PAH/BG)$_5$/AMgS **(Fig. 3.6(a))** was observed to lose small flakes of coating material laterally on the edges and joints of cuts. The delaminated area was reported as 5 % to 15% of the lattice. In the case of SPH/(PAH/BG)$_7$/AMgS **(Fig. 3.6(b)),** only a small portion of the coating was lost at the intersection of squares, which was less than 5%.

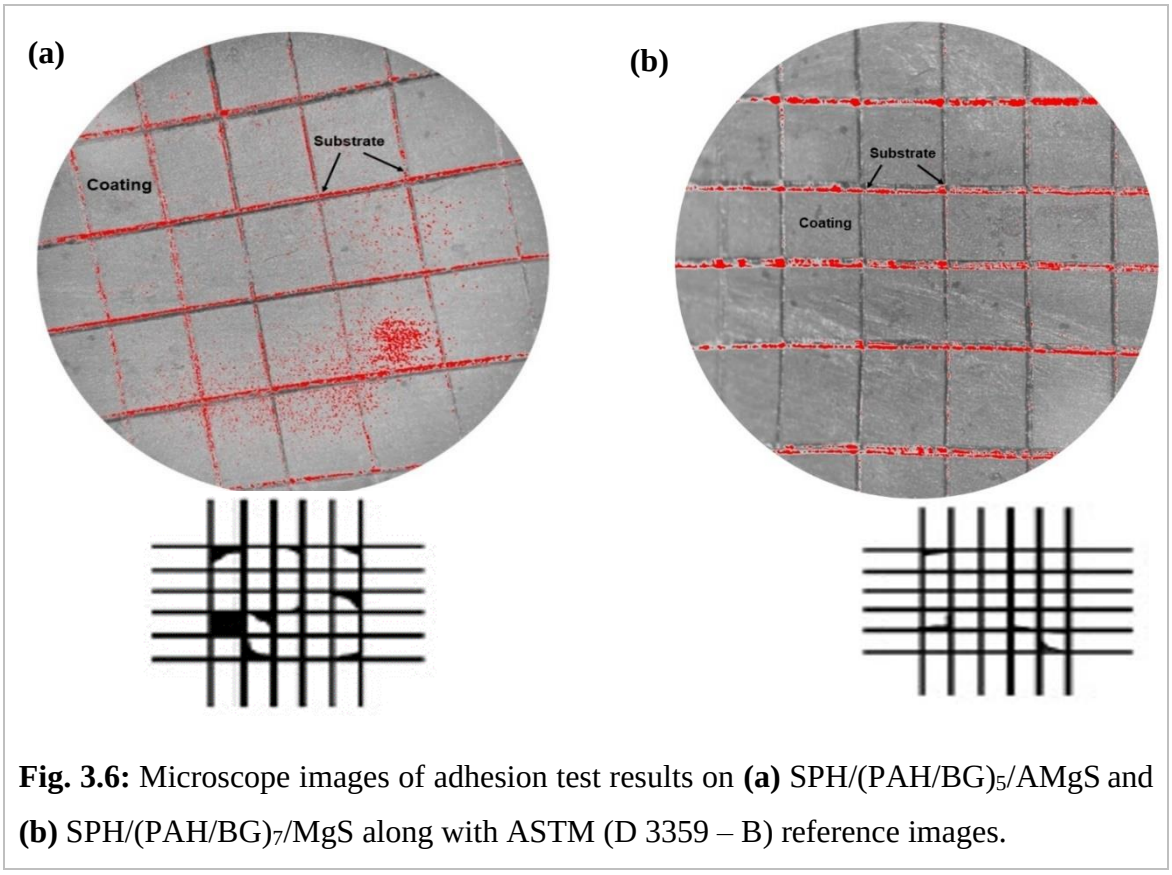

Fig. 3.6: Microscope images of adhesion test results on **(a)** SPH/(PAH/BG)$_5$/AMgS and **(b)** SPH/(PAH/BG)$_7$/MgS along with ASTM (D 3359 – B) reference images.

3.3.4. Corrosion Behaviors

3.3.4.1. Immersion Test and Electrochemical Analysis

Weight loss tests on uncoated and coated substrates were carried out for 3, 7, and 10 d immersion in HBSS at 37 ℃ and the results were compiled in **Table 3.1**. Weight loss of Mg substrate before and after coating generally increased with the immersion time in HBSS. The uncoated Mg alloy substrate exhibited the highest incidence of corrosion, with the maximum weight loss of 62.0 mg ± 0.35 mg after 10 d of interaction with HBSS. The highest weight loss of the bare Mg alloy surface in HBSS is due to the susceptibility to fluid and air. In contrast, the SPH/$(PAH/BG)_5$/AMgS and SPH/$(PAH/BG)_7$/AMgS coated Mg alloy surfaces showed resistance to fluid and air penetrating through the surface and resulted in 15.89 mg ± 0.3 mg and 6.24 mg ± 0.13 mg weight loss, respectively after 10 d treatment with HBSS. Interestingly, SPH/$(PAH/BG)_7$/AMgS exhibited the highest protection efficiency (98.4041 %) within 3 d immersion in HBSS compared to the 5-layer coating on AMgS. These findings are in line with the surface and cross-sectional FESEM micrographs of SPH/$(PAH/BG)_7$/AMgS **(Figs. 3.4((e), (f), (g), (h) and (j))),** which revealed a smooth and compact microstructure.

Table 3.1: The weight loss data of uncoated and coated SPH/$(PAH/BG)_5$ /AMgS and SPH/$(PAH/BG)_7$ /AMgS substrates after immersion with HBSS for 3, 7 and 10 d at 37 ℃.

S.N	Type	Days	Δw (mg)	CR ($mg/cm^2.d$)	PE %	Θ
1	Un coated Mg alloy	3	8.8464	0.5013	-	-
2		7	33.4562	0.8125	-	-
3		10	62.0023	1.0541	-	-
4	SPH/$(PAH/BG)_5$ /AMgS	3	0.5829	0.0303	93.4111	0.9341
5		7	4.3819	0.1064	86.9046	0.8690
6		10	15.8922	0.2701	74.3762	0.7437
7	SPH/$(PAH/BG)_7$/ AMgS	3	0.1411	0.0080	98.4041	0.9840
8		7	2.4521	0.0595	92.6769	0.9267
9		10	6.2485	0.1092	89.9250	0.8992

The electrochemical polarization curves of the uncoated, SPH/$(PAH/BG)_5$/AMgS, and SPH/$(PAH/BG)_7$/AMgS coated Mg alloy substrates are depicted in **Fig.3.7(a)** and the corresponding electrochemical measurements are provided in **Table 3.2.** The corrosion potential (E_{corr}) of the uncoated Mg alloy substrate was reported as -1.62 V_{SCE}, which increased to -1.24 V_{SCE} after coating with SPH/$(PAH/BG)_5$/AMgS. The SPH/$(PAH/BG)_7$ /AMgS coated alloy substrate exhibited the highest E_{corr} (-1.13 V_{SCE}) among the uncoated and SPH/$(PAH/BG)_5$ /AMgS coated substrates. The observed E_{corr} values of uncoated and coated Mg alloy substrates indicate that the BG nanoparticles in the SPH/$(PAH/BG)_n$ composite can resist the penetration of ions from HBSS due to their bioactivity [49]. The corrosion current density (I_{corr}) for the SPH/$(PAH/BG)_5$ /AMgS coating was reported as 6.81 E^{-6} $A.cm^{-2}$, while for the SPH/$(PAH/BG)_7$ coating, I_{corr} = 3.52 E^{-6} $A.cm^{-2}$. The observed higher I_{corr} value for the SPH/$(PAH/BG)_7$ coating compared to the SPH/$(PAH/BG)_5$ coating on AMgS can be attributed to its greater thickness and uniformity as reported by FESEM analysis **(Figs. 3.4((e), (f), (g), (h) and (j))).**

The reported fluctuations in the anodic polarization curves **Fig. 3.7(a)** of the SPH/$(PAH/BG)_5$ and SPH/$(PAH/BG)_7$ coated AMgS occur because of hydrogen gas evolution at the cathode, which ruptures the coating and exposes the substrate surface [2]. The corresponding increase in R_p values for the SPH/$(PAH/BG)_5$/AMgS and SPH/$(PAH/BG)_7$/AMgS coatings were reported as 2.01 E^{+3} $\Omega.cm^2$ and 3.10 E^{+3} $\Omega.cm^2$; respectively. The observed R_p values for the coated substrate are higher compared to the uncoated substrate (1.15 E^{+2} $\Omega.cm^2$) **(Table 3.2).** The significant increase in R_p values for the SPH/$(PAH/BG)_7$/AMgS coating indicates a thicker and more uniform coverage of the coating material on the alloy surface **(Figs.3. 4((e), (f), (g), (h) and (j))).**

Interestingly, the corrosion rate of the SPH/$(PAH/BG)_5$/AMgS (1.75 mm/year) and SPH/$(PAH/BG)_7$/AMgS (0.73 mm/year) was significantly lower compared to the uncoated Mg alloy (6.95 mm/year). The use of BG particles in the surface coating of Mg alloy substrates helps reduce their corrosion rate due to their bioactivity [50].

Table 3.2: Electrochemical parameters of uncoated and coated SPH/$(PAH/BG)_5$ /AMgS and SPH/$(PAH/BG)_7$ /AMgS after immersion with HBSS for 10 days at 37℃.

Type	E_{corr} (V/SCE)	I_{corr} ($_{A.cm^{-2}}$)	βa ($_{V.dec^{-1}}$)	βc ($_{V.dec^{-1}}$)	R_p ($_{\Omega.cm^2}$)	CR (mm/years)
Un coated Mg alloy	-1.62	3.04×10^{-4}	0.19	0.16	1.15×10^{2}	6.96
SPH/$(PAH/BG)_5$/ AMgS	-1.24	6.81×10^{-6}	0.27	0.08	2.01×10^{3}	1.75
SPH/$(PAH/BG)_7$/ AMgS	-1.13	3.52×10^{-6}	1.48	0.16	3.10×10^{3}	0.73

The corrosion behavior of the uncoated and SPH/$(PAH/BG)_n$/AMgS substrates was also investigated after 10 d of interaction in HBSS using EIS measurements. The results are shown in **Figs. 3.7 (b)** and **(c).** The EIS spectrum of the uncoated substrate displayed a single small semicircle, while for the SPH/$(PAH/BG)_5$/AMgS coating, the EIS spectrum showed a merge of two semicircles with larger diameters. The EIS spectrum of the SPH/$(PAH/BG)_7$/AMgS coated substrate also displayed a merge of two semicircles, with the largest semicircle compared to the SPH/$(PAH/BG)_5$/AMgS coated and uncoated surfaces. These observations indicate an increase in impedance and confirm the high corrosion resistance behavior of SPH/$(PAH/BG)_7$/AMgS [51]. The larger low–frequency impedance modulus ($|Z|_{10Hz}$) of the substrates indicates their better corrosion protection performance[16]. As shown in **Fig. 3.7(c),** the $|Z|_{10Hz}$ value of the uncoated Mg alloy is 82567.31 $\Omega.cm^2$, which is lower than the5-layer (189861.99 $\Omega.cm^2$) and seven-layer (1081324.04 $\Omega.cm^2$) SPH/$(PAH/BG)_n$ coatings on AMgS. These results also demonstrate that the SPH/$(PAH/BG)_7$ /AMgS coating significantly improves the corrosion resistance of the Mg alloy.

To obtain detailed information on the degradation processes at the interfaces of the uncoated and coated substrates and the HBSS solution, the EIS data were tailored using equivalent circuits shown in **Figs.3.7 (d) (a1 and b1).** In these models, R_1 and R_2 represent the electrolyte resistance and coating resistance, respectively. C_1 represents the capacitance due to components of the SPH/$(PAH/BG)_n$ /AMgS coating (protective corrosion layer), and

constant phase element (CPE), instead of pure capacitive behavior, is used and is characterized by the admittance (Y_0) and power index number (n), which can be calculated by using the formula [52]:

$$Y_{CPE}(\omega) = \frac{1}{Z_{CPE}} = Y_0 (j\omega)^n \quad (3.5)$$

where; Z_{CPE}, represents the impedance of the constant phase element.

J: imaginary unit and ω; angular velocity (rad/sec).

The proposed equivalent circuit model best fits the EIS spectra, and the derived values of the equivalent circuit parameters are reported in **Table 3.3**. Interestingly, it can be observed that n_1 for SPH/$(PAH/BG)_7$/AMgS is 1.0, indicating a capacitive behavior. However, for the uncoated Mg alloy, the corresponding value decreased to 0.58, indicating a diffusion process. These findings are consistent with the corrosion behavior of SPH/$(PAH/BG)_7$/AMgS in HBSS[53].

Table 3.3: Corrosion parameters obtained from the Nyquist fitted impedance data of MgS, SPH/$(PAH/BG)_5$/AMgS and SPH/$(PAH/BG)_7$/AMgS after immersion with HBSS for 10 days at 37℃.

Sample	R_1 ($\Omega.cm^2$)	R_2 ($\Omega.cm^2$)	CPE_1 ($\Omega^{-1}. S^n$ cm^{-2})	n_1	C_1 ($\Omega^{-1}. S^n$ cm^{-2})	CPE_2 ($\Omega^{-1}. S^n$ cm^{-2})	n_2
Un coated Mg alloy	25691	-	2.4×10^{-7}	0.70	1.54×10^{-9}	4.7×10^{-4}	0.58
SPH/$(PAH/BG)_5$/ AMgS	38534	28364	5×10^{-9}	0.94	7.83×10^{-10}	-	-
SPH/$(PAH/BG)_7$/ AMgS	40363	1.61×10^{5}	1.1×10^{-12}	1.0	3.31×10^{-10}	-	-

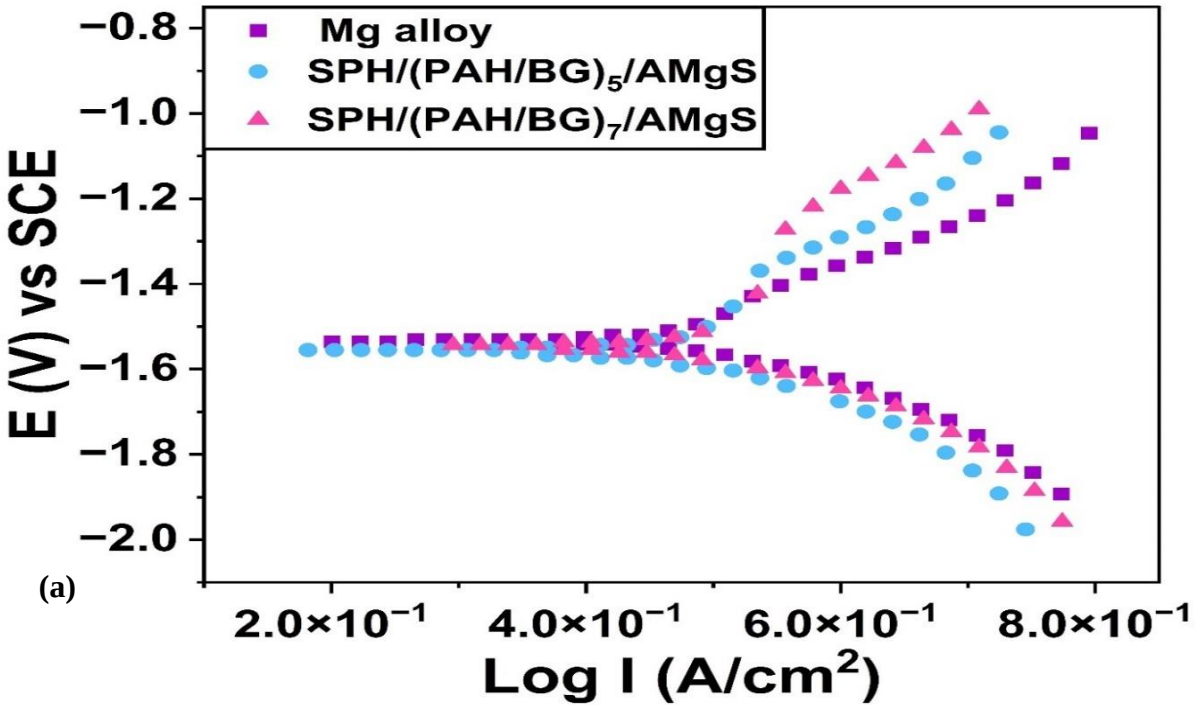
Mg alloy
SPH/(PAH/BG)5/AMgS
SPH/(PAH/BG)7/AMgS
E (V) vs SCE
−0.8
−1.0
−1.2
−1.4
−1.6
−1.8
−2.0
2.0×10−1
4.0×10−1
6.0×10−1
8.0×10−1
Log I (A/cm2)

(a)

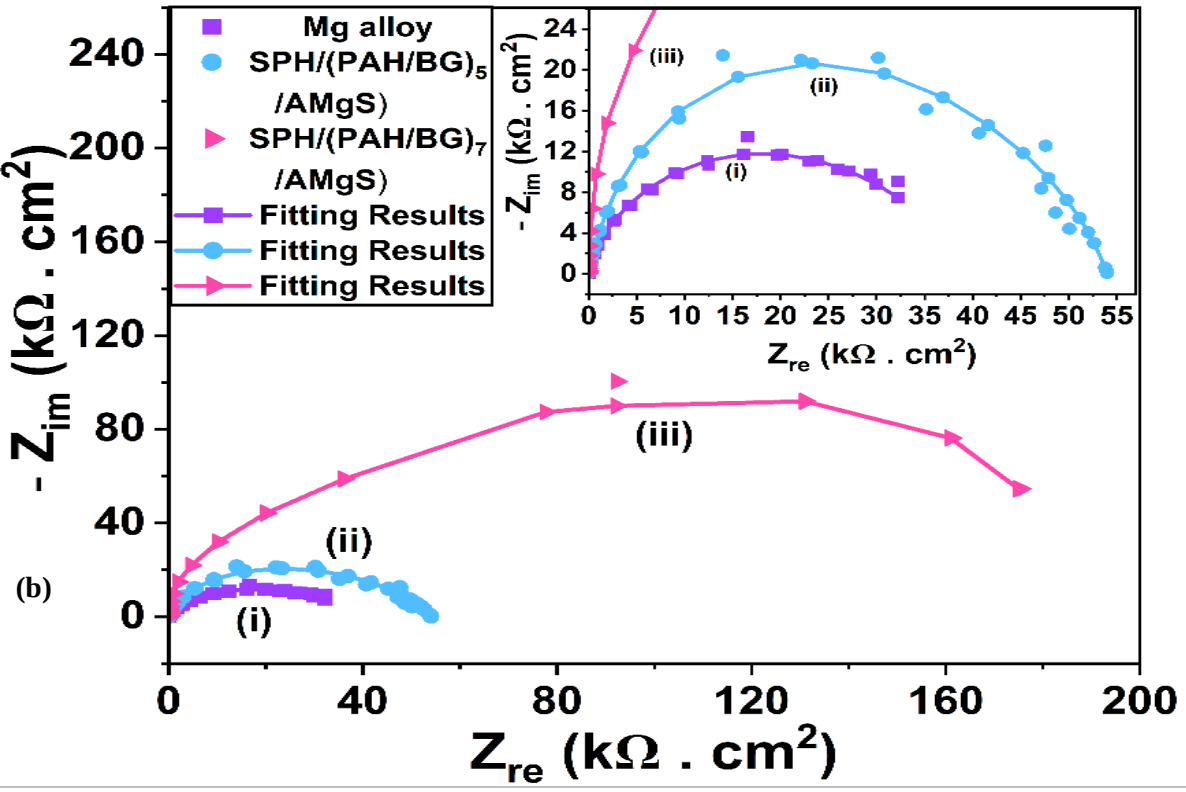
Mg alloy
SPH/(PAH/BG)5 /AMgS)
SPH/(PAH/BG)7 /AMgS)
Fitting Results
Fitting Results
Fitting Results
- Zim (kΩ . cm2)
Zre (kΩ . cm2)
(i)
(ii)
(iii)

(b)

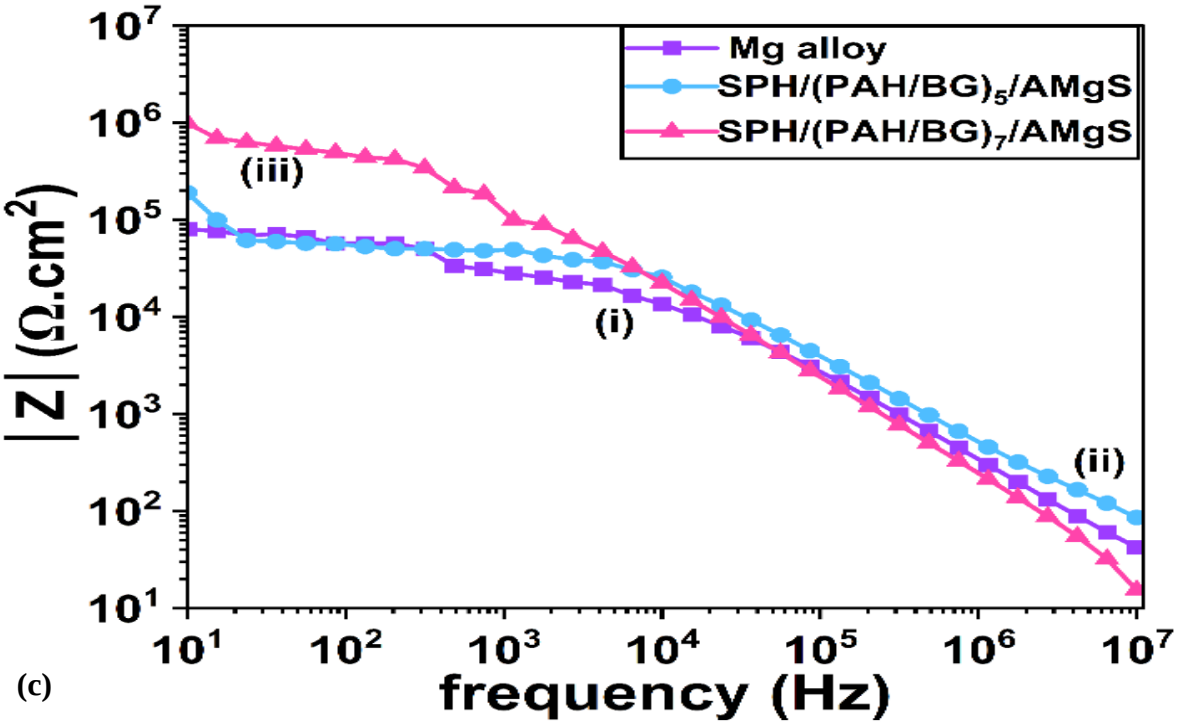

(c)

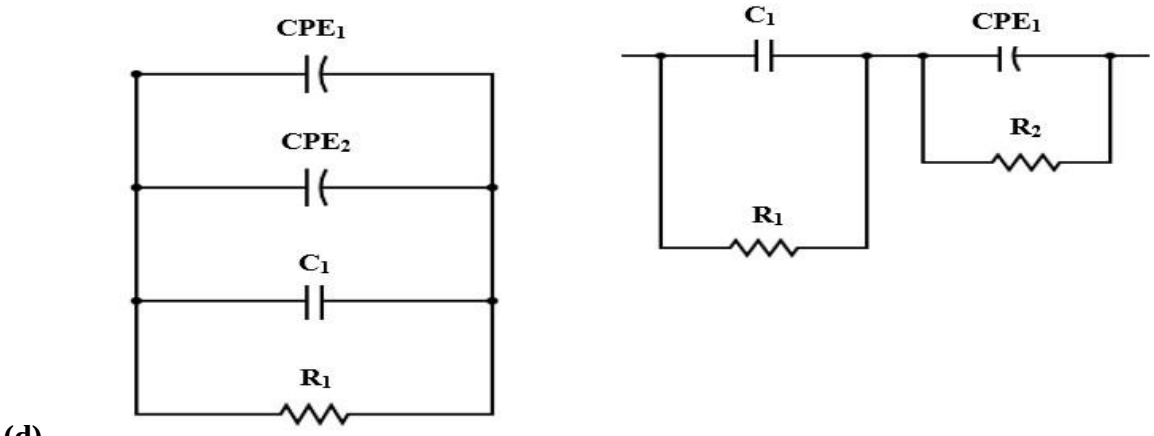

(d)

Fig. 3.7: (a) Potentiodynamic polarization curves and **(b)**Nyquist plots and fitting curves for the **(i)** Mg alloy substrate, **(ii)** SPH/(PAH/BG)$_5$/AMgS and **(iii)** SPH/(PAH/BG)$_7$/AMgS substrates immersed in HBSS for 10 d at 37 ℃ and **(c)** Bode plots of $|Z|$ vs. frequency and **(d)** Equivalent electrical circuits for the impedance data obtained from **(a1)** uncoated as well as **(b1)** coated samples.

3.3.4.2. Analysis of Degradation Behavior

Fig. 3.8 (a) shows the volume of hydrogen gas released as a function of time from uncoated and coated Mg alloy substrates immersed in HBSS. The lowest volume of hydrogen is released from the Mg alloy substrate immersed in HBSS, indicating the lowest corrosion rate of substrate [54]. As observed in **Fig. 3.8 (a),** the SPH/$(PAH/BG)_5$/AMgS and SPH/$(PAH/BG)_7$/AMgS coated substrates released the least amount of hydrogen gas, in contrast to the highest volume of hydrogen gas released by the uncoated Mg alloy. This is in good agreement with electrochemical measurements (Section 3.3.4.1).

The volume of released hydrogen gas from 24 h to 240 h of immersion in HBSS increases from 9.5 $mL.cm^{-2}$ to 73.4 $mL.cm^{-2}$ for the uncoated Mg alloy, ranging between 4.5 $mL.cm^{-2}$ to 46.4 $mL.cm^{-2}$ for SPH/$(PAH/BG)_5$/AMgS, and from 2.2 $mL.cm^{-2}$ to 35.4 $mL.cm^{-2}$ for SPH/$(PAH/BG)_7$/AMgS. After 120 h of immersion in HBSS, the hydrogen evolution was faster for all substrates. Among all substrates, SPH/$(PAH/BG)_7$/AMgS showed the lowest evolution of hydrogen due to the formation of a thicker protective oxide layer on its surface after longer exposure (>120 h) to HBSS [55].

The FTIR spectra of uncoated and SPH/$(PAH/BG)_n$/AMgS are shown in **Fig. 3.8 (b).** The FTIR spectrum of AMgS showed only peaks due to O – H stretching and bending (3671 cm^{-1} and 1396 cm^{-1}) and Mg – O (1244, 1065, and 878). After immersion in HBSS, AMgS displayed new peaks at 1044 cm^{-1} due to PO_4^{3-} . The FTIR spectrum corresponding to SPH/$(PAH/BG)_n$/AMgS for both n, 5 and 7, presents absorption peaks at 3671 cm^{-1}, 2989 cm^{-1} and 2913 cm^{-1} which were due to O – H, C – H, and CH_3 stretching. Peaks at 1400 cm^{-1} and 1044 cm^{-1} were due to N – O vibrations and Si—O⁻ stretching; respectively. Interestingly, Si – O – Si and Si – CH_3 vibrations were reported at 871 cm^{-1} , 713 cm^{-1} and 1245 cm^{-1} ; respectively. These findings support the presence of SPH/$(PAH/BG)_n$ coating on AMgS [56].

The FTIR spectrum of SPH/$(PAH/BG)_n$/AMgS are shown in **Fig. 3.8 (c),** after immersion in HBSS for 10 days showed peaks corresponding to O – H (3678 cm^{-1}), C – H (2885 $cm^{-1}$and 2983 cm^{-1}), ―C=O stretching and ―N―H (1651 cm^{-1}), N – O (1402 cm^{-1}) and Si – O – Si (871 cm^{-1}) vibrations. These observations are more or less similar to SPH/$(PAH/BG)_n$/AMgS before immersion in HBSS. Interestingly, a new peak appeared at 1037 cm^{-1} due to PO_4^{3-} ions indicating the formation of hydroxyapatite due to the bioactivity of BG. After immersion in HBSS, O – H and C – H peak positions were slightly shifted indicating the interaction of SPH/$(PAH/BG)_n$/AMgS with HBSS[57].

Fig. 3.8 (d) shows XRD diffraction patterns of the coated substrates SPH/$(PAH/BG)_5$/AMgS and SPH/$(PAH/BG)_7$/AMgS in contrast to the uncoated Mg alloy substrate. Observed reflections in the corresponding XRD pattern for Mg alloy (JCPDS file no. 00-001-1141) and for SPH/$(PAH/BG)_n$ refer to ($Ca_5(PO_4)_3(OH)$) as per (JCPDS file no. 00-024-0033). The existence of the Mg alloy peak in the SPH/$(PAH/BG)_7$/AMgS sample was less pronounced, which can be attributed to the difficulty of XRD penetration through the coatings to the Mg alloy substrate, due to the higher thickness of the coating. On the other hand the penetration of X–ray through the uncoated and SPH/$(PAH/BG)_5$ /AMgS was easier resulting in the appearance of Mg alloy peaks[8]. The generated coatings, in particular, were amorphous, as confirmed by XRD examination. **Fig. 3.8 (e)** demonstrates the XRD graph of samples after HBSS immersion for 10 days. For the uncoated Mg composite substrate, the presence of $Mg(OH)_2$ and hydroxyapatite in the films formed relating to the $Ca_3(PO_4)_2$ and HA ($Ca_{10}(PO_4)_6(OH)_2$) compounds was clearly visible. However, the Mg signal was also detected, which may be caused by scratching the covering film from the substrate [58,59]. However, it can be seen that the HA peak of the SPH/(PAH/BG)5/AMgS was stronger than the uncoated substrate, indicating that the selected polyelectrolyte improved the formation of HA [60]. On the other hand, peaks of $Ca_3(PO_4)_2$ and HA compounds on SPH/$(PAH/BG)_7$ /AMgS could not be visualized, indicating that the increased layer exhibited high corrosion resistance and can be termed a solution barrier.

Microscopic examination of uncoated and coated surfaces confirmed the surface deposition of corrosion products **(Fig. 3.8 (f)).** The lowest surface deposition was visualized for uncoated substrate immersed in HBSS, which increased with an increase in contact time with HBSS (3 d to 10 d) as illustrated in **Figs. 3.8 ((a1) – (c1))** .These substrates developed numerous micro-cracks throughout the surface. The SPH/$(PAH/BG)_7$/AMgS coated alloy surface was visualized with thicker surface deposition due to the bioactivity of BG along with the corrosion products of the Mg alloy substrate **Figs. 3.8 ((g1) – (i1))** compared to the SPH/$(PAH/BG)_5$/AMgS coating **Figs. 3.8 ((d1) – (f1)).** The *in-vitro* observation is indicative of decreased biodegradability and increased integrity of the SPH/$(PAH/BG)_7$/AMgS with the host [61].

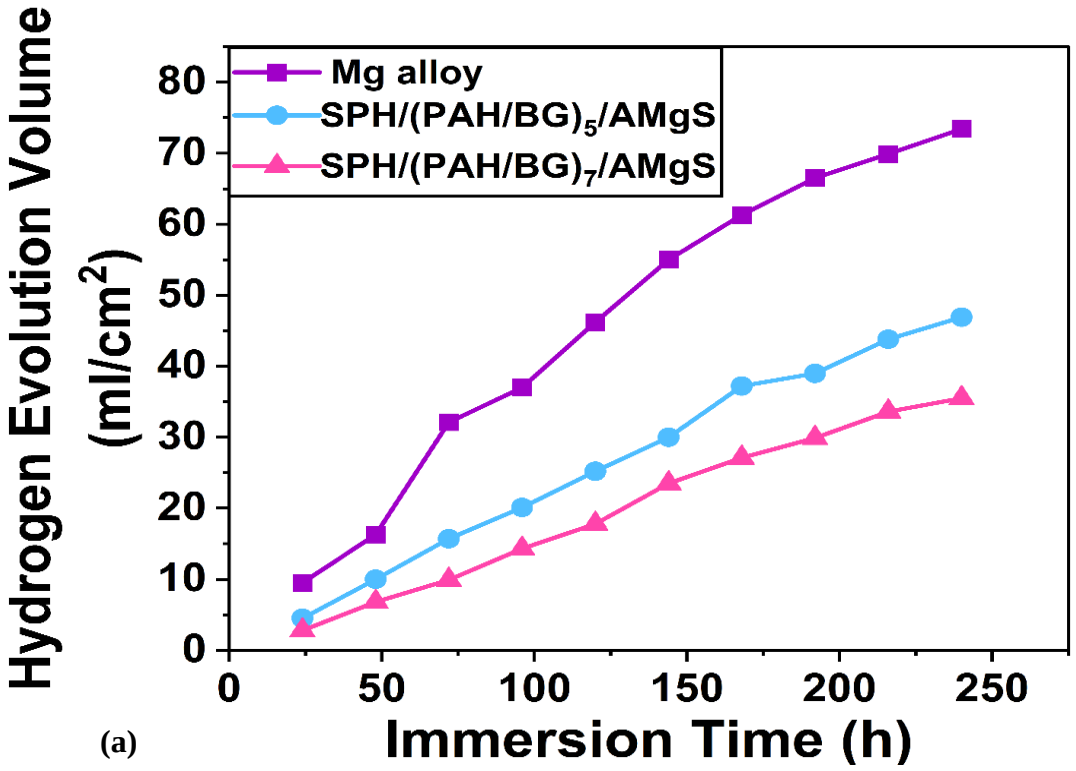

(a)

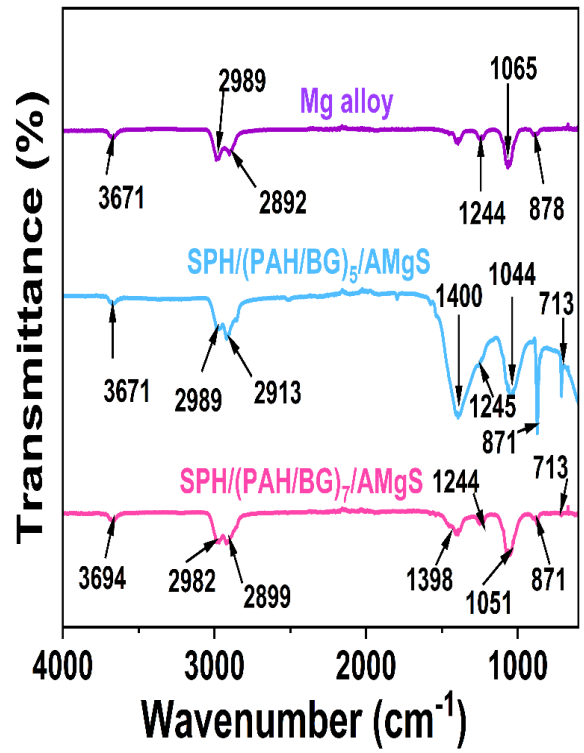
Transmittance (%)
Mg alloy
2989
1065
3671
2892
1244
878
SPH/(PAH/BG)5/AMgS
1400
1044
713
3671
2989
2913
1245
871
SPH/(PAH/BG)7/AMgS
1244
713
3694
2982
2899
1398
1051
871
4000
3000
2000
1000
Wavenumber (cm-1)

(b)

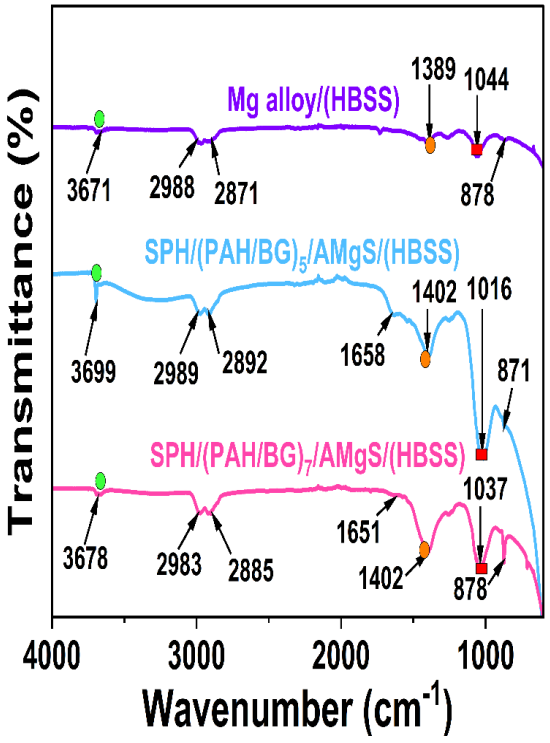
Transmittance (%)
Mg alloy/(HBSS)
1389
1044
3671
2988
2871
878
SPH/(PAH/BG)5/AMgS/(HBSS)
1402
1016
3699
2989
2892
1658
871
SPH/(PAH/BG)7/AMgS/(HBSS)
1037
1651
3678
2983
2885
1402
878
4000
3000
2000
1000
Wavenumber (cm-1)

(c)

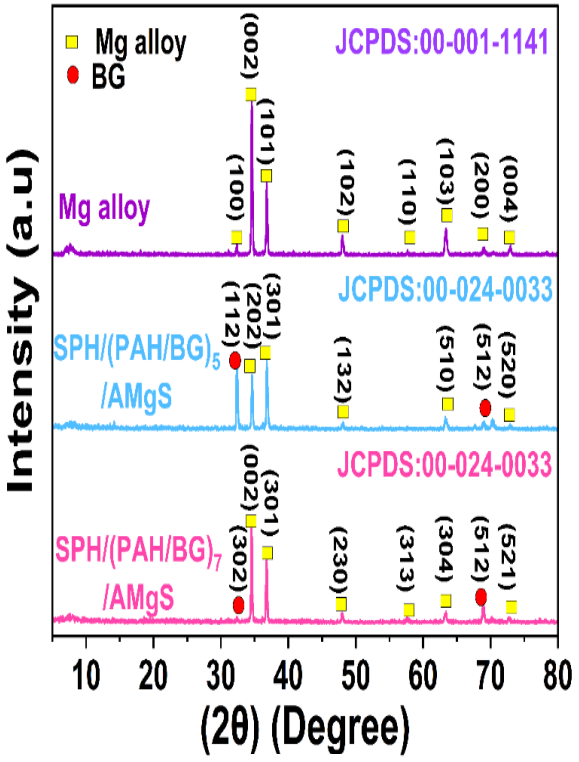
Mg alloy
BG
JCPDS:00-001-1141
(002)
(101)
(100)
(102)
(110)
(103)
(200)
(004)
Mg alloy
JCPDS:00-024-0033
(112)
(202)
(301)
(132)
(510)
(512)
(520)
SPH/(PAH/BG)5
/AMgS
JCPDS:00-024-0033
(002)
(301)
(302)
(230)
(313)
(304)
(512)
(521)
SPH/(PAH/BG)7
/AMgS
Intensity (a.u)
10
20
30
40
50
60
70
80
(2θ) (Degree)

(d)

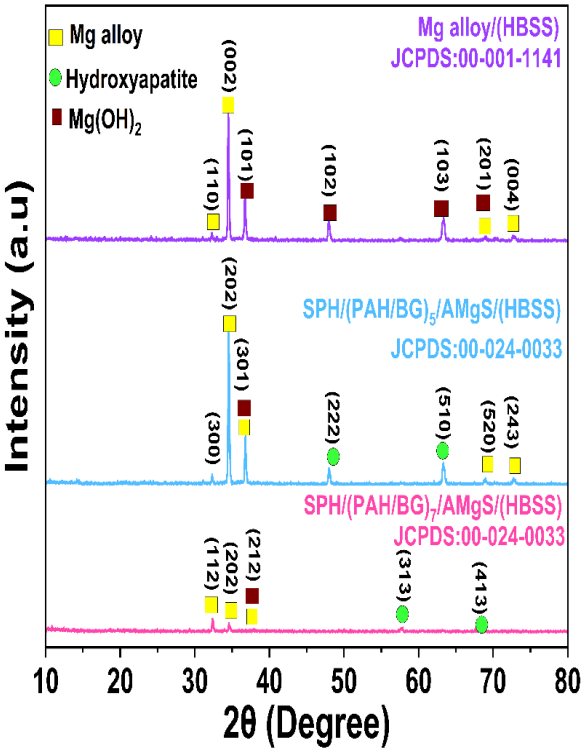
Mg alloy
Hydroxyapatite
Mg(OH)2
Mg alloy/(HBSS)
JCPDS:00-001-1141
(002)
(101)
(110)
(102)
(103)
(201)
(004)
SPH/(PAH/BG)5/AMgS/(HBSS)
JCPDS:00-024-0033
(202)
(301)
(300)
(222)
(510)
(520)
(243)
SPH/(PAH/BG)7/AMgS/(HBSS)
JCPDS:00-024-0033
(112)
(202)
(212)
(313)
(413)
Intensity (a.u)
10
20
30
40
50
60
70
80
2θ (Degree)

(e)

(f)

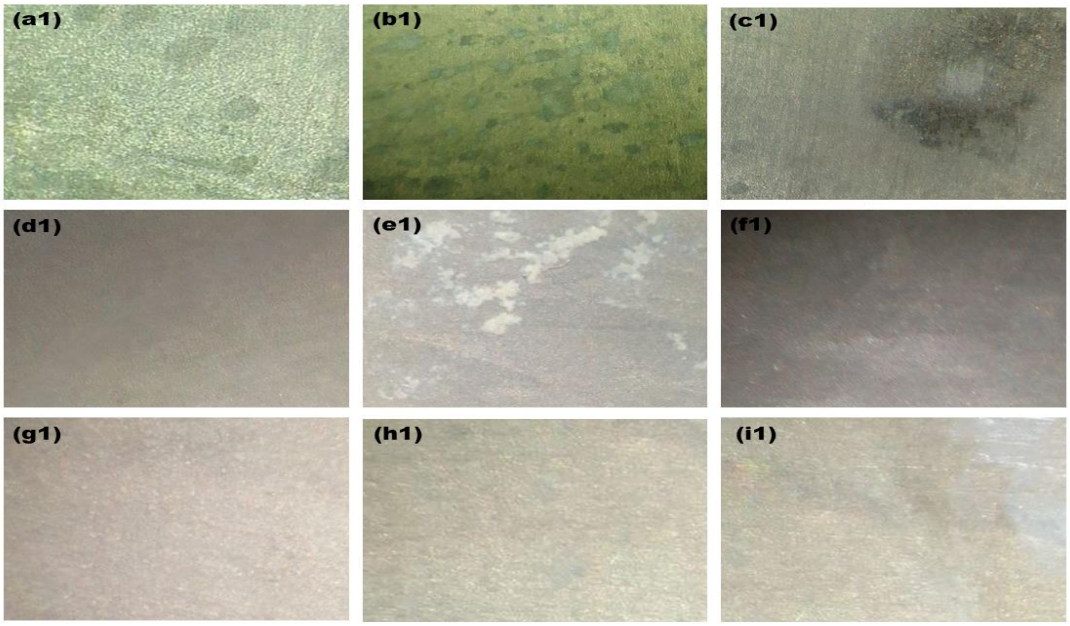

Fig. 3.8: (a) Hydrogen evolution of uncoated and coated substrates **(b), (c)** FTIR spectra **(d),(f)** XRD patterns for uncoated, SPH/$(PAH/BG)_5$/AMgS and SPH/$(PAH/BG)_7$/AMgS before and after immersion in HBSS for 10 d and **(f)** Microscopic images at 1000 X magnification of **(a1 – c1)** MgS **(d1 – f1)** SPH/$(PAH/BG)_5$/AMgS and **(g1 – i1)** SPH/$(PAH/BG)_7$/AMgS after 3, 7 and 10 d of immersion in HBSS; respectively.

Fig. 3.9(a) portrays XPS survey on the elemental composition and chemical state of SPH/$(PAH/BG)_7$/AMgS before and after immersion in HBSS for 10 d at 37 ℃. The XPS survey scan on SPH/$(PAH/BG)_7$/AMgS indicated the existence of Mg1s (1303.58 eV), O1s (531.44 eV), C1s (285.06 eV),Ca2p (350.08 eV), N1s (399.36 eV) and Si2p (103.11 eV) before immersion in HBSS. The observed N1s signal indicated the presence of PAH molecules on the surface of the alloy substrate[13]. **Fig. 3.9 (a)** also revealed the presence of Ca2p and Si2p peaks, demonstrating the successful coating of BG nanoparticles on the Mg substrate. The XPS peaks of the substrate after interaction with HBSS for 10 d were shifted to lower binding energy values for Mg1s (1303.04 eV), O1s (531.17 eV), C1s (284.91 eV), N1s (399.17 eV), and Si2p(102.3 eV) compared to the control. In comparison with the control, XPS peaks corresponding to Ca2p (350.27 eV) of the substrate after interaction with HBSS emerged at higher binding energy values.

These data suggest that following immersion in HBSS, corrosion products are deposited on the surface of Mg alloy substrate. In addition, the bioactivity of BG contents of SPH/$(PAH/BG)_7$/AMgS composite on the coated substrate during immersion in HBSS is also expected to cause the observed shifts in binding energies of the reported elements.

High-resolution XPS spectra of Mg1s, O1s, C1s, Ca2p, N1s, and Si2p are further gathered together to find the chemical status of the existing elements, as shown in **Figs.3.9(b)** and **9(c).** For precise analysis, the resulting high-resolution peaks were subjected to Gaussian model fit using XPS peak fitting 41 and Origin Lab 2023 software, and corresponding observations on Mg alloy surface substrates before and after immersion in HBSS are discussed below:

The coated Mg alloy surface showed XPS peaks corresponding to Mg^{2+} (1303.31 eV Mg1s), C=O (531.18 eV O1s), C– C (284.26 eV C1s), C=C (286.60 eV C1s), Ca^{2+} (346.54 eV Ca2p), CaO (350.56 eV Ca2p), NH_2 (399.01 eV N1s), and SiO_2 (102.82 eV Si2p) before immersion in HBSS [62]. These findings confirmed the existence of BG nanoparticles in SPH/$(PAH/BG)_7$ /AMgS composite coating. The XPS analyses of the Mg alloy surface after 10 d of interaction with HBSS report the following findings. The observed Mg1s peak at 1302.93eV corresponds to $MgHPO_4.H_2O$ [63]. The O1s peak showing a maximum at 530.94 eV indicates the existence of [$–OH^–$], [$PO_4^{3–}$], and [$CO_3^{2–}$] [64]. In most Mg alloys, the most dominant surface corrosion product is $Mg(OH)_2$ because of its lower solubility compared to magnesium phosphate and magnesium carbonate[65]. In the C1s spectra, peaks representing C1s at 284.32 eV and 285.74 eV evidenced the existence of $MgCO_3$ and $CaCO_3$; respectively, on the alloy surface as corrosion products[63]. The higher sub-peak centered at 350.56 eV in the Ca2p spectra corresponds to Ca2p1/2, indicating the presence of calcium salts. The peak centered at 346.54 eV is the Ca2p3/2 peak evidencing calcium-based corrosion products. The observation corresponds to the existence of Ca^{2+} ions in the form of $CaHPO_4.H_2O$ and $CaCO_3$, which are common corrosion products on the Mg alloy surface in HBSS [63].

In the N1s spectra, the peak at 398.87eV could be due to the C–N bond. The peak at 400.48 eV can be attributed to the $–NH_2$ bond[66]. Finally, the appearance of Si2p at 101.30 eV and 102.0 eV evidences the existence of silicon-containing species in the corrosion product layer, such as SiO_2 .

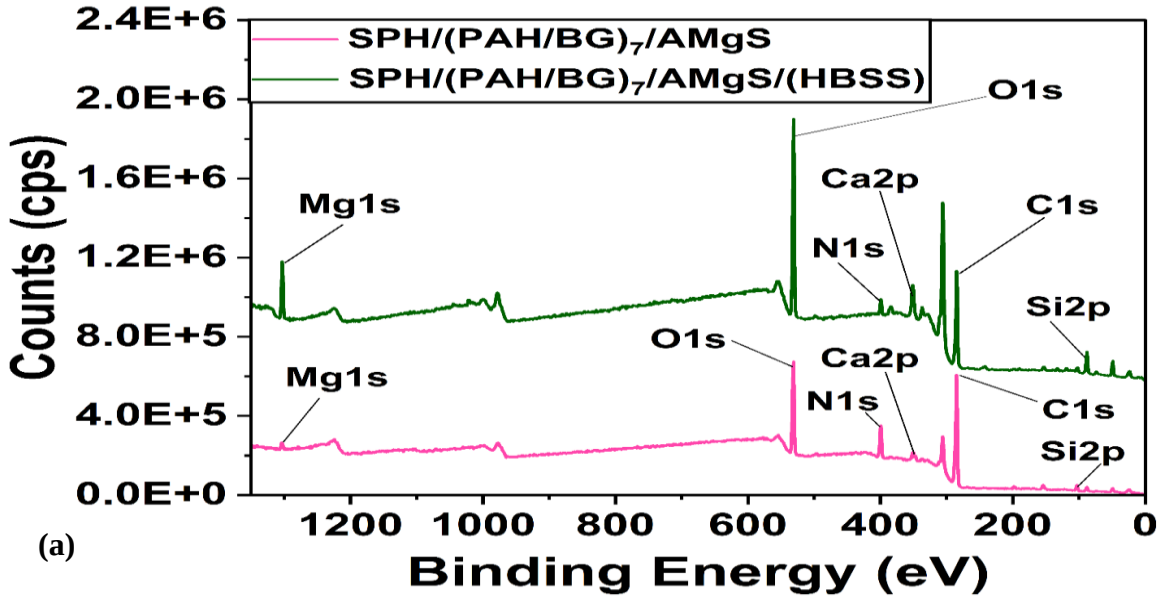

(a)

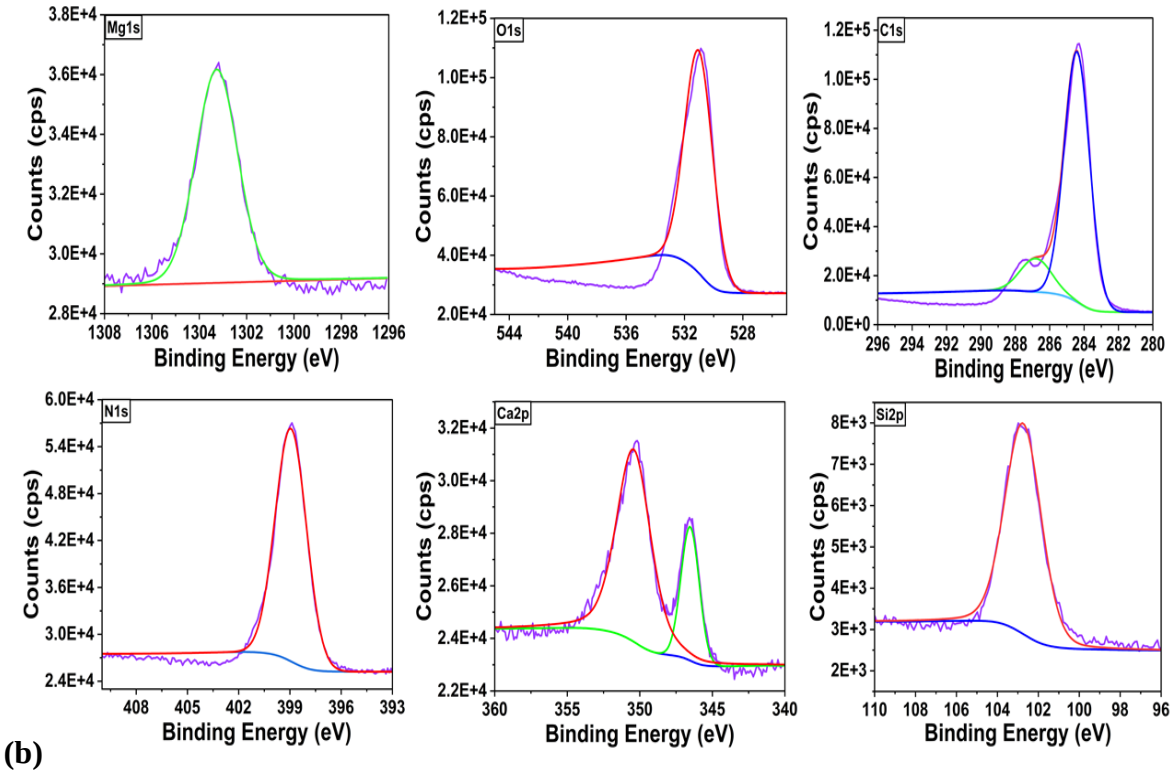

(b)

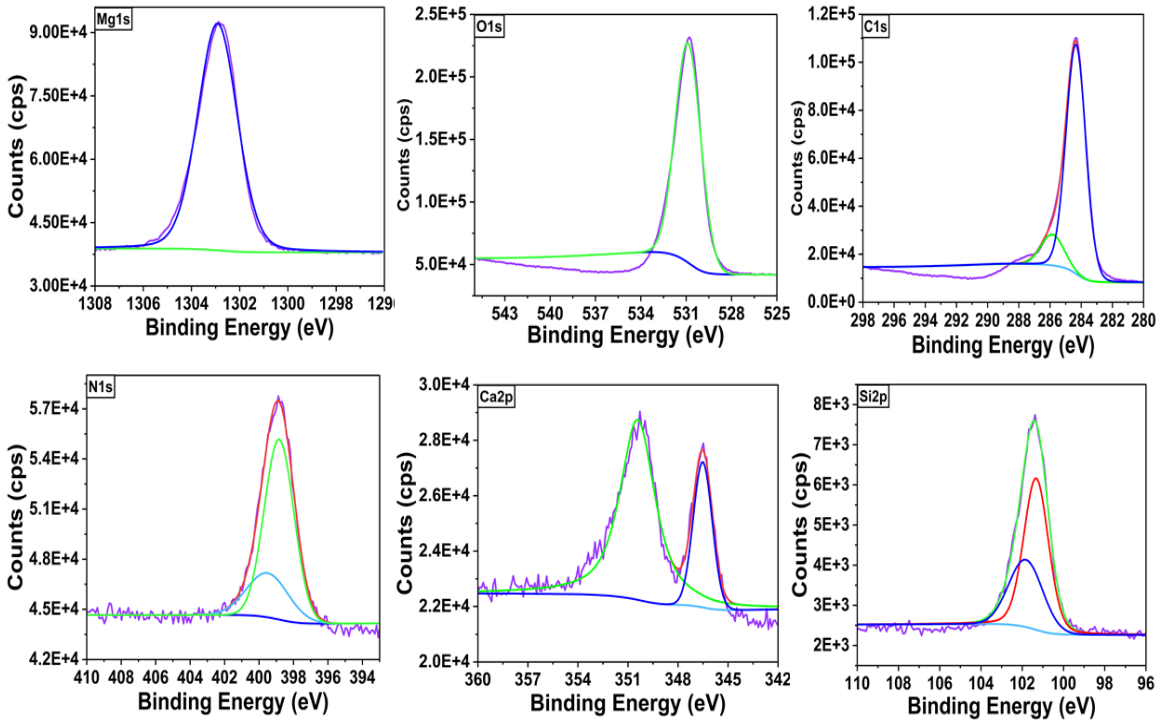

(c)

Fig. 3.9: (a) XPS analysis on SPH/(PAH/BG)$_7$/AMgS before and after immersion in HBSS at 37 ℃. for 10 d, **(b)** XPS with the high resolution scan region representing Mg1s, O1s, C1s, Ca2p, N1s and Si2p for SPH/(PAH/BG)$_7$/AMgS **(c)** XPS with the high resolution scan region representing Mg1s, O1s, C1s, Ca2p, N1s and Si2p for SPH/(PAH/BG)$_7$/AMgS after immersion in HBSS for 10 d.

3.3.5. Hemocompatibility

Evaluating the hemolysis rate of biomaterials is crucial analysis for assessing the biological safety of the same. It is imperative that the hemolysis rate remains below 5% when the biomaterials come into contact with blood [67]. Materials with a high hemolysis rate can potentially cause severe damage to red blood cells, increasing the risk of thrombosis and jeopardizing the success of implantation procedures. As shown in **Fig. 3.10,** the hemolysis rate of the unmodified magnesium alloy was 38.97 ± 0.09% and does not meet the requirements for clinical application. The untreated magnesium allow has inadequate corrosion resistance, leading to the generation of significant quantities of hydrogen peroxide and Mg^{2+} ions. These byproducts result in a rapid elevation of the blood's pH level, facilitating the bonding of red blood cells with Ca^{2+} ions in the solution [68]. This process

ultimately leads to rupture of red blood cells and triggers a severe hemolytic reaction.The hemolysis ratio (HR%) of (AMgS), SPH/$(PAH/BG)_5$/AMgS and SPH/$(PAH/BG)_7$/AMgS was approximately 23.62 ± 0.07 %, 3.93 ± 0.04 % and 2.75 ± 0.01 %; respectively. After alkali treatment and coating, the hemolysis rate decreased significantly. This is because the corrosion resistance of the Mg alloy was significantly improved, reducing the pH changes and Mg^{2+} release. As a result, less damage to red blood cells was observed when the coated substrate was in contact with blood. The lower hemolytic ratio of the coating suggests that it enhances the substrate's biocompatibility. This is consistent with previous studies that reported a hemolysis rate above 5% for untreated Mg alloy Preeti *et al*. demonstrated that Mg alloy coated with strontium-doped calcium phosphate (Ca-Sr-P) had a lower hemolysis rate compared to untreated Mg alloy [69]. Yee-Hsien *et al.* proved that embedding hydroxyapatite particles enhanced the blood compatibility of Mg alloys, with the enhancement being dependent on the HA content [70].

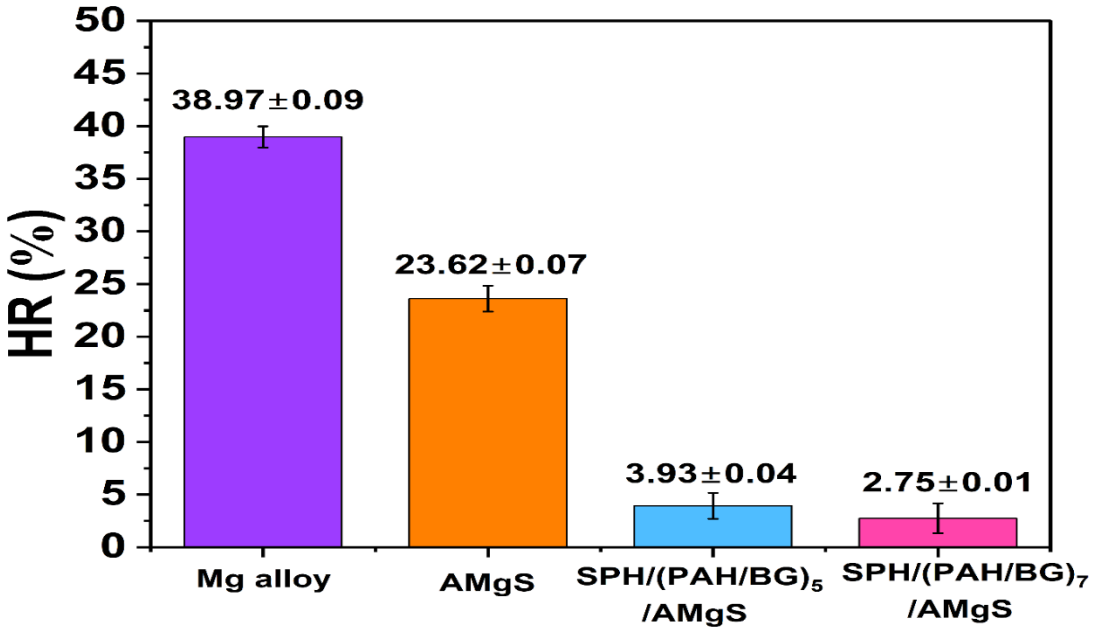

Fig. 3.10: The hemolysis rates (HR%) of uncoated (MgS), AMgS, SPH/$(PAH/BG)_5$/AMgS and SPH/$(PAH/BG)_7$/AMgS ; respectively.

Chapter 3: Multifunctional Poly(Allylamine Hydrochloride) / Bioactive Glass Layer by Layer surface coating on Magnesium Alloy for biomedical applications

LbL Coating Mechanism of SPH/(PAH/BG)$_n$ on AMgS and Salient features

The rising interest in multifunctional implant materials in biomedical applications increases the exploration of novel implant coating materials on Mg alloy substrates. Recent studies have explored various multilayer coating materials on AZ31 Mg alloy surfaces by the dip coating method [8,14,49,71,72]. These studies mostly used polymers in multilayers, but no one has examined the use of BG through the LBL coating mechanism on Mg alloy.

Composite SPH/(PAH/BG)$_7$ coatings (Scheme 1) were deposited on AMgS using a simple dip coating method. AMgS was evidenced with white patches due to surface hydroxylation containing Mg–O and O–H bonds. The net surface charge of AMgS at pH 7.10 was measured as 5 mV. Considering the net surface positive charge and patch-like coverage of hydroxyl groups on AMgS, the substrate was coated with SPH of zeta potential -15 mV at pH 7.10. As a result, a uniform and smooth SPH coating was obtained on AMgS because of the electrostatic force among the positive surface charge of AMgS and the negatively charged functional groups (mostly phosphate groups) of SPH. Overall, the SPH/AMgS net surface charge becomes negative and becomes suitable for the LbL coating of positively charged PAH containing an amine group and negatively charged FA templated BG through electrostatic interaction, hydrogen bonding and other weak physical forces. The resulting SPH/(PAH/BG)$_n$/AMgS indicated several beneficial features for Mg alloy implants. The FA templated BG content could improve the bioactivity of the implant by promoting bone growth and integration with surrounding tissue. Composite coating SPH/(PAH/BG)$_7$ was deposited on the Mg alloy substrate using the dip coating method. The BG nanoparticles for coating were synthesized by an ecofriendly bioinspired method using FA as a template. FESEM morphology of SPH/(PAH/BG)$_7$/AMgS showed a porous rough and compact microstructure. The coating adhered strongly to the surface of the substrate with a thickness of 31.06 ± 0.1 µm and was bioactive upon immersion in HBSS. SPH/(PAH/BG)$_7$/AMgS revealed a water contact angle of 61.85^{o} ± 6.21^{o}, which is appropriate for protein attachment and a roughness value (Ra = 2.95 ± 0.020) for subsequent cell growth. Interestingly, the excellent corrosion-resistant performance of the coating material was demonstrated by weight loss, Tafel polarization and impedance spectroscopy.

For example, SPH/$(PAH/BG)_7$/AMgS after 10 d immersion in HBSS reported excellent E_{corr} and CR values -1.13 (V/SEC) and 0.0080 ($mg/cm^2.d$) compared to the existing literature due to the outstanding bioactivity of nanosized BG.

These findings revealed the excellence of SPH/$(PAH/BG)_7$ multilayer coating with anti-cancerous, anti-oxidant and anti-inflammatory properties on AMgS to eliminate the dissolution of toxic metallic ions from the substrate in physiological environments and proven as a potential candidate for *in–vivo* studies.

3.4. Conclusions

A novel layer-by-layer coating containing SPH and $(PAH/BG)_n$, via the dip technique, is utilized to form a biomimetic $CaHPO_4.H_2O$ coating for enhancing the corrosion resistance of Mg alloy. Synthesized FA templated BG was nano-sized (12.53 ± 2.22) nm and proved to contain anti-cancerous FA molecules. Using BG particles, SPH/$(PAH/BG)_7$ composite coated was successfully deposited on AMgS via layer-by-layer assembly. SPH/$(PAH/BG)_7$/AMgS coating was dense and uniform, showing a thickness of 31.06 µm ± 0.1µm. The SPH/$(PAH/BG)_7$/AMgS demonstrated a suitable water contact angle of 61.85^{o} ± 6.21^{o}, which is appropriate for protein attachment. Also, composite coatings presented appropriate roughness values and good adhesive with the substrate that help in cell attachment and their proliferation. In HBSS, both hydrogen evolution and electrochemical corrosion tests confirmed BG caused $CaHPO_4.H_2O$ coating provided good corrosion protection for Mg metal. The cytocompatibility of SPH/$(PAH/BG)_7$/AMgS was confirmed through a hemolysis assay. Results imply that the SPH/$(PAH/BG)_7$/AMgS can be an ideal cytocompatibility material with multifunctional (anti-cancerous, anti-oxidant, and anti-inflammatory) properties for biomedical applications of Mg alloys.

References:

[1] P.J.U. Lokesh Choudhary , R.K. Singh Raman , Joelle Hofstetter, In-vitro characterization of stress corrosion cracking of aluminium-free magnesium alloys for temporary bio-implant applications, Mater. Sci. Eng. C. 42 (2014) 629–636. https://doi.org/10.1016/j.msec.2014.06.018.

[2] C. Lianxi Chen, Chuan-Ming Tseng, W.L. , Youmin Qiu, Junjie Yang , Chi-Lung Chang, XiaojianXiaojian Wang, A layer-by-layer assembled coating for improved stress corrosion cracking on biomedical magnesium alloy in cell culture medium, Surf. Coat. Technol. 403 (2020) 126427. https://doi.org/10.1016/j.surfcoat.2020.126427.

[3] S.V. Svenja Heisea, Tobias Wirtha, Michael Höhlingerb, Yadir Torres Hernándezc, Jose Antonio Rodriquez Ortizc, Victoria Wagenerb, Aldo R. Boccaccinia, Electrophoretic deposition of chitosan/bioactive glass/silica coatings on stainless steel and WE43 Mg alloy substrates, Surf. Coat. Technol. 344 (2018) 553–563.

[4] Y. Ding, Y. Li, J. Lin, C. Wen, Effects of zirconium and strontium on the biocorrosion of Mg-Zr-Sr alloys for biodegradable implant applications, J. Mater. Chem. B. 3 (2015) 3714–3729. https://doi.org/10.1039/c5tb00433k.

[5] S.A. Omar, Y. Castro, J. Ballarre, W.H. Schreiner, A. Durán, S.M. Ceré, Magnesium alloys implants coated with 58S sol-gel bioactive glass to retard first stage corrosion, Corrosion. 73 (2017) 1448–1460. https://doi.org/10.5006/2508.

[6] L.T. Mostafa Yazdimamaghania, Mehdi Razavib, Daryoosh Vashaee, Venkata Raveendra Pothineni, Jayakumar Rajadasd, Significant degradability enhancement in multilayer coating of polycaprolactone-bioactive glass/gelatin-bioactive glass on magnesium scaffold for tissue engineering applications Mostafa, Appl. Surf. Sci. 338 (2015) 137–145.

[7] L.W. and M.W.K. M. Fazley Elahi , Guoping Guan, Influence of Layer-by-Layer Polyelectrolyte Deposition and EDC/NHS Activated Heparin Immobilization onto Silk Fibroin Fabric, Materials (Basel). 7 (2014) 2956–2977.

[8] F.Z. Lan-Yue CUI, Rong-Chang ZENG , Xiao-Xiao ZHU, Ting-Ting PANG, Shuo-Qi LI, Corrosion resistance of biodegradable polymeric layer-by-layer coatings on magnesium alloy AZ31 Lan-Yue, Front. Mater. Sci. (2016) 1–13. https://doi.org/10.1007/s11706-016-0332-1.

[9] M. Keeney, X.Y. Jiang, M. Yamane, M. Lee, S. Goodman, F. Yang, Nanocoating for biomolecule delivery using layer-by-layer self-assembly, J. Mater. Chem. B. 3 (2015) 8757–8770. https://doi.org/10.1039/c5tb00450k.

[10] G.K. Mansi Uday Joshi , Shruti Prakash Kulkarni , Mounika Choppadandi , M. Keerthana, Current state of art smart coatings for orthopedic implants: A comprehensive review, Smart Mater. Med. 4 (2023) 661–679. https://doi.org/10.1016/j.smaim.2023.06.005.

[11] and J.S. Fan Fan, Chunyu Zhou, Xu Wang, Department, Layer-by-Layer Assembly of a Self-Healing Anticorrosion Coating on Magnesium Alloys, ACS Appl. Mater. Interfaces. 7 (2015) 27271–27278. https://doi.org/10.1021/acsami.5b08577.

[12] A. Abdal-hay, M.-H.L. , Anwarul Hasan , Yu-Kyoung, K.A.K. Abdel Salam Hamdy, Biocorrosion behavior of biodegradable nanocomposite fibers coated layer-by-layer on AM50 magnesium implant, Mater. Sci. Eng. C. 58 (2016) 1232–1241. http://dx.doi.org/10.1016/j.msec.2015.09.065 0928-4931/©.

[13] L.Y. Cui, R.C. Zeng, X.X. Zhu, T.T. Pang, S.Q. Li, F. Zhang, Corrosion resistance of biodegradable polymeric layer-by-layer coatings on magnesium alloy AZ31, Front. Mater. Sci. 10 (2016) 134–146. https://doi.org/10.1007/s11706-016-0332-1.

[14] L. yue CUI, J. XU, N. LU, R. chang ZENG, Y. hong ZOU, S. qi LI, F. ZHANG, In vitro corrosion resistance and antibacterial properties of layer-by-layer assembled chitosan/poly-L-glutamic acid coating on AZ31 magnesium alloys, Trans. Nonferrous Met. Soc. China (English Ed. 27 (2017) 1081–1086. https://doi.org/10.1016/S1003-6326(17)60126-2.

[15] L.Y. Cui, R.C. Zeng, S.Q. Li, F. Zhang, E.H. Han, Corrosion resistance of layer-by-layer assembled polyvinylpyrrolidone/polyacrylic acid and amorphous silica films on AZ31 magnesium alloys, RSC Adv. 6 (2016) 63107–63116. https://doi.org/10.1039/c6ra08613f.

[16] R.-C.Z. Lan-Yue Cui, Xiao-Hui Fang, Wei Cao, E.-H.H. , Shuo-Qi Li, Xiao-Bo Chen, Yu-Hong Zou, Shao-Kang Guan, In vitro corrosion resistance of a layer-by-layer assembled DNA coating on magnesium alloy, Appl. Surf. Sci. J. 457 (2018) 49–58.

[17] and J.L. Xingxing Yin, Peng Mu, Qingtao Wang, Superhydrophobic ZIF-8-Based Dual-Layer Coating for Enhanced Corrosion Protection of Mg Alloy, ACS Appl. Mater. Interfaces. 12 (2020) 35453–35463. https://dx.doi.org/10.1021/acsami.0c09497.

[18] L.Y. Cui, S.C. Cheng, L.X. Liang, J.C. Zhang, S.Q. Li, Z.L. Wang, R.C. Zeng, In vitro corrosion resistance of layer-by-layer assembled polyacrylic acid multilayers induced Ca–P coating on magnesium alloy AZ31, Bioact. Mater. 5 (2020) 153–163. https://doi.org/10.1016/j.bioactmat.2020.02.001.

[19] Z.W.P. Yanbin Zhao, Liqian Shi, Xiaojing Ji, Jichen Li, Zhuangzhuang Han, Shuoqi Li, Rongchang Zeng, Fen Zhang, Corrosion resistance and antibacterial properties of

polysiloxane modified layer- by-layer assembled self-healing coating on magnesium alloy, J. Colloid Interface Sci. (2018). https://doi.org/10.1016/j.jcis.2018.04.071.

[20] V.S. Yadav, M.R. Sankar, L.M. Pandey, Coating of bioactive glass on magnesium alloys to improve its degradation behavior : Interfacial aspects, J. Magnes. Alloy. 8 (2020) 999–1015.

[21] J.N. Oliver, D. Zhu, Y. Su, X. Lu, P. Kuo, J. Du, Bioactive Materials Bioactive glass coatings on metallic implants for biomedical applications, Bioact. Mater. 4 (2019) 261–270. https://doi.org/10.1016/j.bioactmat.2019.09.002.

[22] E. Vafa, L. Taybi, M. Abbasi, M. Javad, R. Bazargan, A better roadmap for designing novel bioactive glasses: effective approaches for the development of innovative revolutionary bioglasses for future biomedical applications, Environ. Sci. Pollut. Res. 30(55) (2022) 116960-116983. https://doi.org/10.1007/s11356-022-24176-1.

[23] M.E.B. Ehsan Vafa , Reza Bazargan-Lari, Electrophoretic deposition of polyvinyl alcohol/natural chitosan/bioactive glass composite coatings on 316L stainless steel for biomedical application, Prog. Org. Coatings. 151 (2021) 106059. https://doi.org/j.porgcoat.2020.106059.

[24] A.M.A. Ehsan Vafa, Reza Bazargan-Lari, Mohammad Ebrahim bahrololoom, Effect of polyvinyl alcohol concentration on biomedical application of chitosan/bioactive glass composite coated on AZ91D magnesium alloy, Mater. Chem. Phys. 291 (2022) 126650. https://doi.org/10.1016/j.matchemphys.2022.126650.

[25] R. Sergi, D. Bellucci, V. Cannillo, A Comprehensive Review of Bioactive Glass Coatings : State of the Art , Challenges and Future Perspectives, Coatings. 10 (2020) 1–30. https://doi.org/10.3390/coatings10080757.

[26] H. Goel, D. Santhiya, Effect of pH on bio-inspired synthesis of L-Lysine templated bioactive glass hybrid xerogels for tailored textural and rheological properties, Mater. Chem. Phys. 281 (2022) 125828. https://doi.org/10.1016/j.matchemphys.2022.125828.

[27] H. Goel, N. Gupta, D. Santhiya, N. Dey, H.B. Bohidar, A. Bhattacharya, Bioactivity reinforced surface patch bound collagen-pectin hydrogel, Int. J. Biol. Macromol. 174 (2021) 240–253. https://doi.org/10.1016/j.ijbiomac.2021.01.166.

[28] A.D. Smith, Y. Kim, H. Refsum, Is folic acid good for everyone ? 1 , 2, Am. J. Clin. Nutr. 87 (2008) 517–533. https://doi.org/10.1093/ajcn/87.3.517.

[29] Y.I. Kim, Folate and cancer prevention: A new medical application of folate beyond hyperhomocysteinemia and neural tube defects, Nutr. Rev. 57 (1999) 314–321.

https://doi.org/10.1111/j.1753-4887.1999.tb06905.x.

[30] T.J. Ashaolu, Health Applications of Soy Protein Hydrolysates, Int. J. Pept. Res. Ther. 26 (2020) 2333–2343. https://doi.org/10.1007/s10989-020-10018-6.

[31] J. Ciejka, M. Grzybala, A. Gut, M. Szuwarzynski, K. Pyrc, M. Nowakowska, K. Szczubialka, Tuning the Surface Properties of Poly (Allylamine Hydrochloride)-Based Multilayer Films Justyna, Materials (Basel). 14 (2021) 1–19.

[32] W.T. and S.R. Hongchi Zhao, Xiuting Wu, Synthesis and thermal property of poly(allylamine hydrochloride) Hongchi, Adv. Mater. Res. 150–151 (2011) 1480–1483.

[33] Z.S. Guan-Nan Li , Su-Ming Zhu , Jian-Feng Nie , Yufeng Zheng, Investigating the stress corrosion cracking of a biodegradable Zn-0.8 wt%Li alloy in simulated body fluid Guan-Nan, Bioact. Mater. J. 6 (2021) 1468–1478.

[34] I.M. Ghayad, M.A. Maamoun, W.A. Metwally, A.N. Abd El-Azim, Z.M. El-Baradie, Corrosion Control of Mg-Zn Implant Alloys in Simulated Body Fluid, Chem. Mater. Res. 7 (2015) 27–41.

[35] A.N. AlHazaa, E.S.M. Sherif, H.S. Abdo, Galvanic corrosion in 3.5 wt. % NaCl solutions of magnesium alloy AZ31 coupled with Ni after different bonding periods of time, Int. J. Electrochem. Sci. 10 (2015) 5420–5433.

[36] Yu-Hong ZOU, Rong- Chang ZENG, Qing-Zhao WANG, Li-Jun LIU, Qian-Qian XU, Chuang Wang, Blood compatibility of zinc–calcium phosphate conversion coating on Mg–1.33Li–0.6Ca alloy, Front. Mater. Sci. 2016,. 10 (2016) 281–289. https://doi.org/10.1007/s11706-016-0345-9.

[37] Y. Ouyang, Z. Zhang, W. Huang, W. Yang, C. Shen, Y. Chen, X. Yin, Y. Liu, Electrodeposition of F-doped hydroxyapatite-TiO2 coating on AZ31 magnesium alloy for enhancing corrosion protection and biocompatibility , J Mater Sci. 57 (2022) 17188–17202. https://doi.org/10.1007/s10853-022-07732-5.

[38] O.M. El-Borady, A.F. El-Sayed, Synthesis, morphological, spectral and thermal studies for folic acid conjugated ZnO nanoparticles: Potency for multi-functional bio-nanocomposite as antimicrobial, antioxidant and photocatalytic agent, J. Mater. Res. Technol. 9 (2020) 1905–1917. https://doi.org/10.1016/j.jmrt.2019.12.022.

[39] H. Goel, D. Santhiya, Role of Trigonella foenum-graecum leaf extract in tailoring the synthesis and properties of bioactive glass nanoparticles, Sustain. Mater. Technol. 33 (2022) e00485. https://doi.org/10.1016/j.susmat.2022.e00485.

[40] D. Santhiya, F. Anjum, glass-ceramic using CT-DNA as a template, J. Mater. Chem. B. 1 (2013) 6329–6338. https://doi.org/10.1039/c3tb21212b.

[41] N. Meyer, L.R. Rivera, T. Ellis, J. Qi, A.R. Boccaccini, Zein / Bioactive Glass Composites by Electrophoretic Deposition, Coatings. 8 (2018) 1–12. https://doi.org/10.3390/coatings8010027.

[42] A. Vora, A. Riga, D. Dollimore, K.S. Alexander, Thermal stability of folic acid, Thermochim. Acta. 392–393 (2002) 209–220. https://doi.org/10.1016/S0040-6031(02)00103-X.

[43] N. Gupta, A. Singh, N. Dey, S. Chattopadhyay, J.P. Joseph, D. Gupta, M. Ganguli, A. Pal, Pathway-Driven Peptide-Bioglass Nanocomposites as the Dynamic and Self-Healable Matrix, Chem. Mater. 33 (2021) 589–599. https://doi.org/10.1021/acs.chemmater.0c03757.

[44] Y. Ahmed, A. Nawaz, R. Singh Virk, A. Wadood, M.A. Ur Rehman, Fabrication and characterization of zein/bioactive glass deposited on pretreated magnesium via electrophoretic deposition, Int. J. Ceram. Eng. Sci. 2 (2020) 254–263. https://doi.org/10.1002/ces2.10066.

[45] J.R. Jones, Reprint of: Review of bioactive glass: From Hench to hybrids, Acta Biomater. 23 (2015) S53–S82. https://doi.org/10.1016/j.actbio.2015.07.019.

[46] Y. Ahmed, M. Atiq, U. Rehman, Improvement in the surface properties of stainless steel via zein / hydroxyapatite composite coatings for biomedical applications, Surfaces and Interfaces. 20 (2020) 100589. https://doi.org/10.1016/j.surfin.2020.100589.

[47] H.W. Yixuan Li, Sheng Zhao, Sirong Li, Yuxiang Ge, Rongliang Wang, Liming Zheng, Jiankun Xu, Minghui Sun, Qing Jiang, Yifeng Zhang, Surface Engineering of Biodegradable Magnesium Alloys for Enhanced Orthopedic Implants Yixuan, NANO.MICRO Small. 1904486 (2019) 1–10.

[48] A.N.S. Institute, Standard Test Methods for Rating Adhesion by Tape Test1, ASTM Int. (2017) 1–9. https://doi.org/10.1520/D3359-17.

[49] L. Liu, P. Li, Y. Zou, K. Luo, F. Zhang, R.C. Zeng, S. Li, In vitro corrosion and antibacterial performance of polysiloxane and poly(acrylic acid)/gentamicin sulfate composite coatings on AZ31 alloy, Surf. Coatings Technol. 291 (2016) 7–14. https://doi.org/10.1016/j.surfcoat.2016.02.016.

[50] J. Hum, A. Boccaccini, S. Naseri, Fabrication and characterization of zein – bioactive glass scaffolds, Bioinspired, Biomim. Nanobiomaterials. 4 (2014) 73–78.

[51]F.Z. Lan-yue CUI, Ji XU, Na LU, Rong-chang ZENG, Yu-hong ZOU, Shuo-qi LI, In vitro corrosion resistance and antibacterial properties of layer-by-layer assembled chitosan/poly-L-glutamic acid coating on AZ31 magnesium alloys, Trans. Nonferrous Met. Soc. China. 27 (2017) 1081−1086.

[52] J.E.G. González, J.C. Mirza-Rosca, Study of the corrosion behavior of titanium and some of its alloys for biomedical and dental implant applications, J. Electroanal. Chem. 471 (1999) 109–115. https://doi.org/10.1016/S0022-0728(99)00260-0.

[53] R. Chaharmahali, A. Fattah-Alhosseini, H. Esfahani, Increasing the in-vitro corrosion resistance of AZ31B-Mg alloy via coating with hydroxyapatite using plasma electrolytic oxidation, J. Asian Ceram. Soc. 8 (2020) 39–49. https://doi.org/10.1080/21870764.2019.1698143.

[54] D. Song, G. Guo, J. Jiang, L. Zhang, A. Ma, X. Ma, J. Chen, Z. Cheng, Hydrothermal synthesis and corrosion behavior of the protective coating on Mg-2Zn-Mn-Ca-Ce alloy, Prog. Nat. Sci. Mater. Int. 26 (2016) 590–599. https://doi.org/10.1016/j.pnsc.2016.11.002.

[55] Z. Li, Z. Peng, Y. Qiu, K. Qi, Z. Chen, X. Guo, Study on heat treatment to improve the microstructure and corrosion behavior of ZK60 magnesium alloy, J. Mater. Res. Technol. 9 (2020) 11201–11219. https://doi.org/10.1016/j.jmrt.2020.08.004.

[56] S. Kunst, L. Vanessa, R. Beltrami, H. Ribeiro, P. Cardoso, U.F. De Sergipe, Characterization of Siloxane-poly (methyl methacrylate) Hybrid Films Obtained on a Tinplate Substrate Modified by the Addition of Organic and Inorganic Acids, Mat. Res. 18(1) (2015). https://doi.org/10.1590/1516-1439.299514.

[57] P.P. Singh, K. Dixit, N. Sinha, A sol-gel based bioactive glass coating on laser textured 316L stainless steel substrate for enhanced biocompatability and anti-corrosion properties, Ceram. Int. 48 (2022) 18704–18715. https://doi.org/10.1016/j.ceramint.2022.03.144.

[58] D.B. Pokharel, W. Liping, J. Dong, X. Wei, I.I.N. Etim, D.B. Subedi, A.J. Umoh, W. Ke, Effect of D-fructose on the in-vitro corrosion behavior of AZ31 magnesium alloy in simulated body fluid, J. Mater. Sci. Technol. 66 (2021) 202–212. https://doi.org/10.1016/j.jmst.2020.03.080.

[59] L.Y. Cui, X.T. Li, R.C. Zeng, S.Q. Li, E.H. Han, L. Song, In vitro corrosion of Mg–Ca alloy — The influence of glucose content, Front. Mater. Sci. 11 (2017) 284–295. https://doi.org/10.1007/s11706-017-0391-y.

[60] Z.K. Zhenzhen Gui, Y. Li, Corrosion mechanism of the as-cast and as-extruded biodegradable Mg-3.0Gd-2.7Zn-0.4Zr-0.1Mn alloys, Mater. Sci. Eng. C. 96 (2019) 831–840.

[61] Y. Jin, C. Blawert, H. Yang, B. Wiese, F. Feyerabend, J. Bohlen, D. Mei, M. Deng, M. Silva, N. Scharnagl, K. Strecker, J. Bode, C. Vogt, R. Willumeit-römer, Microstructure-corrosion behaviour relationship of micro-alloyed Mg-0 . 5Zn alloy with the addition of Ca , Sr , Ag , In and Cu, Mater. Des. 195 (2020)108980. https://doi.org/10.1016/j.matdes.2020.108980.

[62] B.R. Barrioni, E. Norris, J.R. Jones, M.D.M. Pereira, The in fl uence of cobalt incorporation and cobalt precursor selection on the structure and bioactivity of sol – gel-derived bioactive glass, J. Sol-Gel Sci. Technol. (2018). https://doi.org/10.1007/s10971-018-4823-7.

[63] B. Di Tie, F. Feyerabend, N. Hort, R. Willumeit, D. Hoeche, XPS Studies of Magnesium Surfaces after Exposure to Dulbecco ' s Modified Eagle Medium , Hank ' s Buffered Salt Solution , and Simulated Body Fluid, (2010) 699–704. https://doi.org/10.1002/adem.201080070.

[64] G. Duan, L. Yang, S. Liao, C. Zhang, X. Lu, Y. Yang, Designing for the chemical conversion coating with high corrosion resistance and low electrical contact resistance on AZ91D magnesium alloy, Corros. Sci. 135 (2018) 197–206. https://doi.org/10.1016/j.corsci.2018.02.051.

[65] M. Kavyani, G.R. Ebrahimi, H.R. Ezatpour, M. Jahazi, Microstructure refinement, mechanical and biocorrosion properties of Mg–Zn–Ca–Mn alloy improved by a new severe plastic deformation process, J. Magnes. Alloy. 10 (2022) 1640–1662. https://doi.org/10.1016/j.jma.2020.11.013.

[66] L.Y. Li, Z.Z. Han, R.C. Zeng, W.C. Qi, X.F. Zhai, Y. Yang, Y.T. Lou, T. Gu, D. Xu, J.Z. Duan, Microbial ingress and in vitro degradation enhanced by glucose on bioabsorbable Mg–Li–Ca alloy, Bioact. Mater. 5 (2020) 902–916. https://doi.org/10.1016/j.bioactmat.2020.06.014.

[67] Chang-Jiang, L.-R.W. , Yu Hou , Ya-Nan Wang , Fei Gao , Tao Liu , Yan-Hua Hou , Yu-Fu Zhu a, Wei Ye, Effects of self-assembly of 3-phosphonopropionic acid, 3-aminopropyltrimethoxysilane and dopamine on the corrosion behaviors and biocompatibility of a magnesium alloy, Mater. Sci. Eng. C. 67 (2016) 132–143. https://doi.org/10.1016/j.msec.2016.05.038.

[68] Y.W. Fan Gao, Youdong Hu, Guicai Li, Sen Liu, Li Quan, Zhongmei Yanga, C. Pan, Layer-by-layer deposition of bioactive layers on magnesium alloy stent materials to improve

corrosion resistance and biocompatibility, Bioact. Mater. 5 (2020) 611–623. https://doi.org/10.1016/j.bioactmat.2020.04.016.

[69] B.L. Preeti Makkar, Hoe Jin Kang, Andrew R. Padalhin, Omar Faruq, In-vitro and in-vivo evaluation of strontium doped calcium phosphate coatings on biodegradable magnesium alloy for bone applications, Appl. Surf. Sci. 510 (2020) 145333. https://doi.org/10.1016/j.apsusc.2020.145333.

[70] T.-C.W. Yee-Hsien Ho, Kun Man, Sameehan S. Joshi, Mangesh V. Pantawane, N.B.D. Yong Yang, In-vitro biomineralization and biocompatibility of friction stir additively manufactured AZ31B magnesium alloy-hydroxyapatite composites, Bioact. Mater. 5 (2020) 891–901. https://doi.org/10.1016/j.bioactmat.2020.06.009.

[71] L. Cui, X. Fang, W. Cao, R. Zeng, S. Li, X. Chen, Applied Surface Science In vitro corrosion resistance of a layer-by-layer assembled DNA coating on magnesium alloy, Appl. Surf. Sci. J. 457 (2018) 49–58. https://doi.org/10.1016/j.apsusc.2018.06.240.

[72] L. Cui, R. Zeng, S. Li, E. Han, RSC Advances polyvinylpyrrolidone / polyacrylic acid and amorphous silica films on AZ31 magnesium alloys †, RSC Adv. 6 (2016) 63107–63116. https://doi.org/10.1039/C6RA08613F

CHAPTER 4

Conclusions &Recommendations

Chapter Four
Conclusion & Recommendation

4.1. Conclusions

Based on the experimental observations from the synthesis bioactive glass and use as a coating with other biocompatible materials and performed corrosion and mechanical testing, the following conclusions can be drawn:

In the first project, a bio-inspired approach was used to synthesize nano-sized bioactive glass (BG) using CTAB as a template. This BG nano powder was then used to create a zein_BG composite coating on an AZ31B Mg alloy substrate through dip coating. The composite coating exhibited physical and chemical bonding between zein and BG, showed a compact and rough microstructure, and demonstrated strong adhesion to the substrate. The coating also exhibited excellent corrosion resistance, making it a promising candidate for biomedical applications, as it could prevent the release of toxic metallic ions in physiological environments.

In the second project, a novel layer-by-layer coating containing SPH and $(PAH/BG)_n$, via the dip technique, is utilized to form a biomimetic $CaHPO_4.H_2O$ coating for enhancing the corrosion resistance of Mg alloy. Synthesized FA templated BG was nano-sized (12.53 ± 2.22) nm and proved to contain anti-cancerous FA molecules. Using BG particles, $SPH/(PAH/BG)_7$ composite coated was successfully deposited on AMgS via layer-by-layer assembly. $SPH/(PAH/BG)_7$/AMgS coating was dense and uniform, showing a thickness of 31.06 µm ± 0.1µm. The $SPH/(PAH/BG)_7$/AMgS demonstrated a suitable water contact angle of $61.85^{o} \pm 6.21^{o}$, which is appropriate for protein attachment. Also, composite coatings presented appropriate roughness values and good adhesion with the substrate that help in cell attachment and their proliferation. In HBSS, both hydrogen evolution and electrochemical corrosion tests confirmed BG caused $CaHPO_4.H_2O$ coating provided good corrosion protection for Mg metal. The cytocompatibility of $SPH/(PAH/BG)_7$/AMgS was confirmed through a hemolysis assay. Results imply that the $SPH/(PAH/BG)_7$/AMgS can be an ideal cytocompatibility material with multifunctional (anti-cancerous, anti-oxidant, and anti-inflammatory) properties for biomedical applications of Mg alloys.

Overall, this thesis presents evidence that surface modification offers a viable approach for effectively regulating the biodegradation rate and enhancing the biocompatibility of magnesium and its alloys. As a result, these materials show great potential as favorable choices for orthopedic applications.

4.2. Recommendation for Future Work

This work has provided a platform for the development of a novel layer by layer coating for the improvement of magnesium alloy for use as a biodegradable biomaterial. However, there is more work required. The following are avenues for future research required in order to achieve this:

1) It is of interest to further study, the microstructure and degradation behavior of AZ31 Mg alloy by using alloying and layer by layer coating to optimize the degradation rate and mechanical performance of the alloy system.

2) The effect of wettability and surface roughness of Mg alloys on the degradation rate and cell behavior should be widely studied under in - vivo conditions. Beside this, the effect of surface morphology and porosity on the corrosion behaviors of Mg alloy in vivo has not been fully investigated.

3) Biocompatibility and cytocompatibility testing in - vivo experimentation.